MICROFABRICATED FUEL CELLS TO POWER INTEGRATED CIRCUITS

A Thesis
Presented to
The Academic Faculty

by

Christopher W. Moore

In Partial Fulfillment of the
Requirements for the Degree
Doctor of Philosophy in
Chemical & Biomolecular Engineering

Georgia Institute of Technology
May 2005

MICROFABRICATED FUEL CELLS TO POWER INTEGRATED CIRCUITS

Approved:

Dr. Paul Kohl, Chairman
School of Chemical & Biomolecular Engineering
Georgia Institute of Technology

Dr. Dennis Hess
School of Chemical & Biomolecular Engineering
Georgia Institute of Technology

Dr. Peter Hesketh
School of Mechanical Engineering
Georgia Institute of Technology

Dr. Meilin Liu
School of Materials Science & Engineering
Georgia Institute of Technology

Dr. Carson Meredith
School of Chemical & Biomolecular Engineering
Georgia Institute of Technology

Date Approved: May 5, 2005

ACKNOWLEDGMENTS

This project could not have been completed without the help and support of many people. Dr. Kohl came up with the microfabricated fuel cell idea and provided guidance throughout the project. Jun Li performed many of the electrochemical tests, co-authored technical papers and presentations, and was an overall great help. Other group members who contributed to this project included Dhananjay Bhusari, Paul Joseph, and Justin Tullis. Hollie (Reed) Kelleher provided me with tremendous help in learning how to use cleanroom equipment to make microchannels and was a good friend.

Robert Bondi also helped show me the ropes in the cleanroom and with the electrical engineering side of microfabrication. He also was a good friend and classmate, and we worked together on some interesting class projects. My two best friends that I met at Georgia Tech are Christopher Timmons and Cody Berger. The three of us regularly ate lunch together where a wide variety of topics were discussed, usually sports. This was typically the highlight of the workday. Cody and I became fathers at about the same time, so we got to experience our wives' pregnancies and early parenthood together. Timmons and I spent many hours watching and talking about football and I was honored to be in his wedding.

Off campus, I made many friends at Powers Ferry Rd. Church of Christ. Tops among them are Jimmy and Joyce Marquis. They practically adopted Somaly and me as soon as we met. Their family, including Jimmy and Janet, Tammy, and Larry and Robin Hawk, along with the grandchildren, are very special to us and will not only be what we miss most about Atlanta, but also what will bring us back for future visits.

Giving me support throughout my life have been my parents. The ideals I learned growing up have helped me to make it through graduate school. They have always been there to give me anything I have needed and then some. My brother, Marcus, has become my best friend and even though we live far apart, we have stayed close, probably closer than when we under the same roof. He followed me to Ol' Mizzou, but not down here, so he has had keep me up to date with anything or anyone back home in Lee's Summit or Columbia.

The person who deserves the most credit for all her love and support is my wife, Somaly. She came down here in love with me while I was confused and didn't know much about anything. We have started our life together and been blessed with our first daughter, Marissa, another child on the way, and hopefully more in the future. Through it all, she has worked to help take care of us so I could concentrate on school. Now, I can only hope to give her all she deserves so that she can concentrate on more important things in life, such as being a great mother and wife as we set out on the next part of our lives.

TABLE OF CONTENTS

LIST OF TABLES

LIST OF FIGURES

SUMMARY

Microfabricated fuel cells have been designed and constructed on silicon integrated circuit wafers using many processes common in integrated circuit fabrication, including sputtering, polymer spin coating, reactive ion etching, and photolithography. Fuel delivery microchannels were made through the use of sacrificial polymers. The characteristics of different sacrificial polymers were studied to find the most suitable for this work. A polypropylene carbonate solution containing a photo-acid generator could be directly patterned with ultraviolet exposure and thermal decomposition. The material that would serve as the fuel cell's proton exchange membrane (PEM) encapsulated the microchannels. Silicon dioxide deposited by plasma enhanced chemical vapor deposition (PECVD) at relatively low temperatures exhibited material properties that made it suitable as a thin-film PEM in these devices. By adding phosphorous to the silicon dioxide recipe during deposition, a phosphosilicate glass was formed that had an increased ionic conductivity. Various polymers were tested for use as the PEM or in combination with oxide to form a composite PEM. While it did not work well alone, using Nafion on top of the glass layer to form a dual-layer PEM greatly enhanced the fuel cell performance, including yield and long-term reliability. Platinum and platinum/ruthenium catalyst layers were sputter deposited. Experiments were performed to find a range of thicknesses that resulted in porous layers allowing contact between reactants, catalyst, and the PEM. When using the deposited glasses, multiple layers of catalyst could be deposited between thin layers of the electrolyte, resulting in higher catalyst loading while maintaining porosity. The current and power output were greatly improved with these additional catalyst layers.

CHAPTER 1

INTRODUCTION

1.1 Micro Power Generation

Portable electronic devices, including those for mobile communications, microsensors, micro-electromechanical systems (MEMS), and microfluidic devices will benefit from advances in energy storage. The availability of power sources with higher energy density and lower cost will enable a wider range of usage and functionality. One possible higher energy density source is the fuel cell.

For electronic devices with small power requirements, microfabricated power sources, including fuel cells, are being investigated (1-6). The possibility of co-fabricating a power source on the same substrate as the electric circuit offers many advantages, including a reduction in size and weight, improved signal integrity because of fewer interconnects, increased processing efficiency, and lower cost. Integrated microfabricated fuel cells are potentially the smallest form-factor chemical energy source with the lowest cost since they use materials and processes already present in the electronic device.

This project brings together two areas of study: fuel cells and MEMS fabrication. Along with a dramatic decrease in size, the microfabricated fuel cell materials and processing must be different from conventional fuel cell construction. Below, typical fuel cell materials are discussed, followed by a description of the material properties and processes that will be used for the microfabricated devices.

1.2 Dissertation Overview

Microfabricated fuel cells have been designed and constructed on silicon integrated circuit wafers using many processes common in integrated circuit fabrication, including sputtering, polymer spin coating, reactive ion etching, and photolithography. Proton exchange membranes (PEM) have been made by low-temperature, plasma-enhanced chemical vapor deposition (PECVD) of silicon dioxide, phosphorous-doped silicon dioxide, and polymer films. Fuel delivery channels were made through the use of a patterned sacrificial polymer below the PEM and anode catalyst. Platinum and platinum-ruthenium catalysts were deposited by DC sputtering. The resistivity of the oxide films was higher than traditional polymer electrolyte membranes, e.g. Nafion, but they were also much thinner. Results showed that the amount of catalyst in the thin-film electrodes chiefly limited the performance.

The next chapter gives more background information on fuel cells and thin-film processing. Chapter 3 details the equipment and processes used in fabrication and testing of micro fuel cells. Chapter 4 discusses the design of the devices, including sizing considerations. Chapter 5 explains the process sequence to fabricate the fuel cells with emphasis on the sacrificial polymers used to form the microchannels. Chapter 6 discusses the sputtered catalyst electrodes. Results are shown for different catalyst loadings, including multiple layers, and factors affecting the activity of the catalyst are discussed. In Chapter 7, the use of acidic methanol is investigated as a fuel for direct methanol fuel cells, specifically microchannel-based devices, in order to increase the area for catalyst usage. Chapter 8 discusses silicon dioxide deposited through PECVD at low temperatures and its use as a thin-film PEM. In Chapter 9, the results are given for micro

fuel cells that feature composite PEMs with polymer on SiO_2. Chapter 10 discusses phosphorous-doping of PECVD SiO_2 films and the effects on ionic conductivity and overall cell performance. The fabrication of microchannel fuel cells with larger active areas and other design improvements is discussed in Chapter 11. The final chapter gives some conclusions and recommendations based on the work presented here.

CHAPTER 2

LITERATURE REVIEW

2.1 Introduction

Portable electronic devices, including those for mobile communications, microsensors, micro-electromechanical systems (MEMS), and microfluidic devices will benefit from advances in energy storage. The availability of power sources with higher energy density and lower cost will enable a wider range of usage and functionality. One possible higher energy density source is the fuel cell.

For electronic devices with small power requirements, microfabricated power sources, including fuel cells, are being investigated (1-6). The possibility of co-fabricating a power source on the same substrate as the electric circuit offers many advantages, including a reduction in size and weight, improved signal integrity because of fewer interconnects, increased processing efficiency, and lower cost. Integrated microfabricated fuel cells are potentially the smallest form-factor chemical energy source with the lowest cost since they use materials and processes already present in the electronic device.

This project brings together two areas of study: fuel cells and MEMS fabrication. Along with a dramatic decrease in size, the microfabricated fuel cell materials and processing must be different from conventional fuel cell construction. Below, typical fuel cell materials are discussed, followed by a description of the material properties and processes that will be used for the microfabricated devices.

2.2 Fuel Cells

Fuel cells are galvanic cells that chemically convert a fuel into electrical energy. Chemical reactions take place at an anode and a cathode. At the anode, the fuel is catalytically oxidized to produce protons and electrons. The electrons move through the electrical circuit. Meanwhile, the protons pass through a proton exchange membrane (PEM) to the cathode. At the cathode, the protons and electrons catalytically reduce oxygen (usually from air) to produce water vapor. Possible fuels include hydrogen and methanol. Hydrogen fuel cells produce only water, while direct methanol fuel cells (DMFCs) also give off carbon dioxide. Overviews of fuel cells (7) and DMFCs (8) can be found in the literature.

PEM fuel cells typically operate at temperatures from ambient to 120°C. Figure 2.1 shows a schematic of a PEM fuel cell with hydrogen as the fuel. Hydrogen can be stored as a pressured gas or in a metal hydride form. It requires humidification for high membrane conductivity.

2.3 Direct Methanol Fuel Cells

Direct methanol fuel cells (DMFCs) are a class of PEM fuel cell that use methanol and water as the fuel instead of hydrogen. Figure 2.2 shows a schematic of a PEM fuel cell with hydrogen as the fuel. The methanol-water mixture can be fed to the anode in either liquid or vapor form. Methanol is an attractive fuel option because it is stored as a liquid, is inexpensive, and has a high specific energy. Possible applications for DMFCs exist in the transportation, space, and military sectors. The following sections discuss the main issues and research for DMFCs.

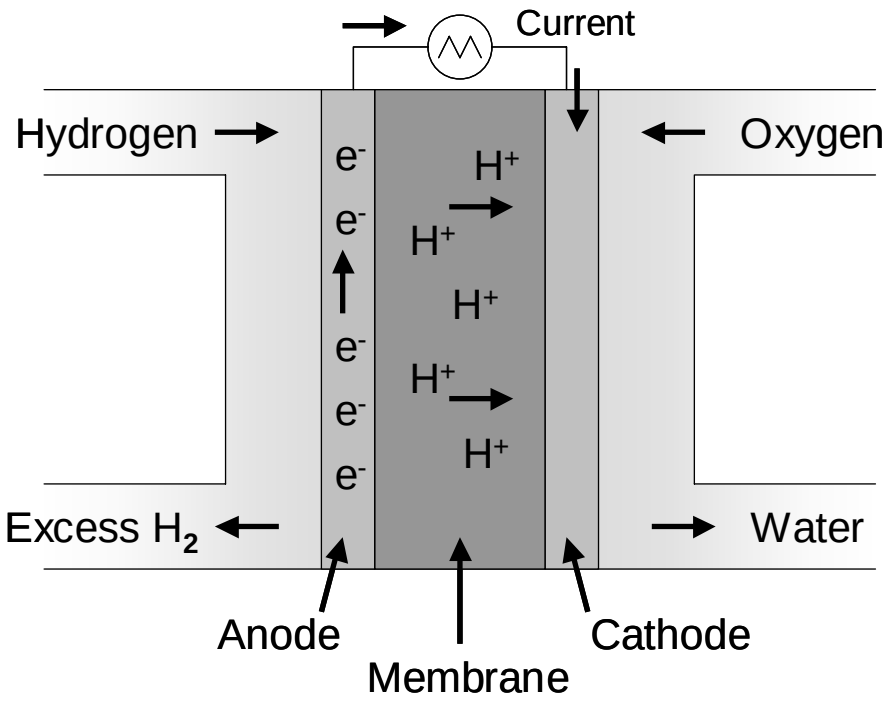

Figure 2.1: Schematic of a PEM fuel cell with hydrogen fuel

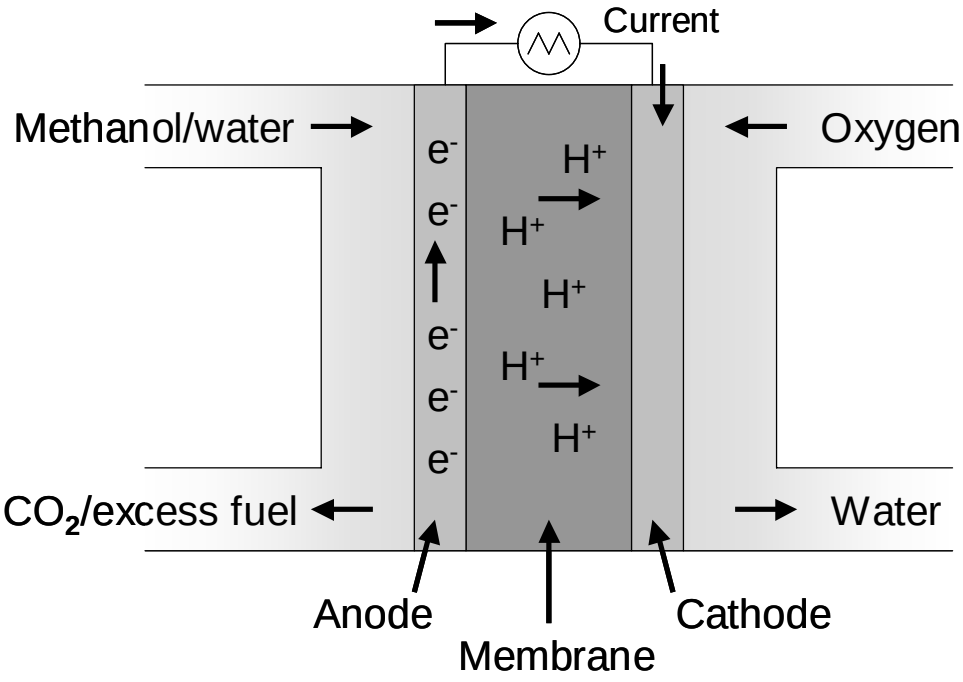

Figure 2.2: Schematic diagram of a direct methanol fuel cell

2.3.1 Methanol Oxidation

Many studies on the oxidation of methanol have been performed (9-14). Platinum and platinum based alloys display a high activity and stability for use as electrode materials. In a DMFC methanol and water react in the following way:

$$CH_3OH + H_2O \rightarrow CO_2 + 6H^+ + 6e^- \qquad \Delta G = -3.827 \text{ kJ/mol}, \Delta U_o = 0.0066 \text{ V} \quad (1)$$

where DG is the Gibbs free energy change of the reaction, which is related to the cell voltage by equation 2.

$$\Delta G = -nF\Delta U_o \quad (2)$$

where n is the number of electrons in the reaction, F is the Faraday constant, and ΔUo is the voltage for thermodynamic equilibrium in the absence of current flow.

It is assumed that the oxidation of methanol begins with the adsorption of methanol on Pt, followed by deprotonation to CO as shown in Figure 2.3 (15).

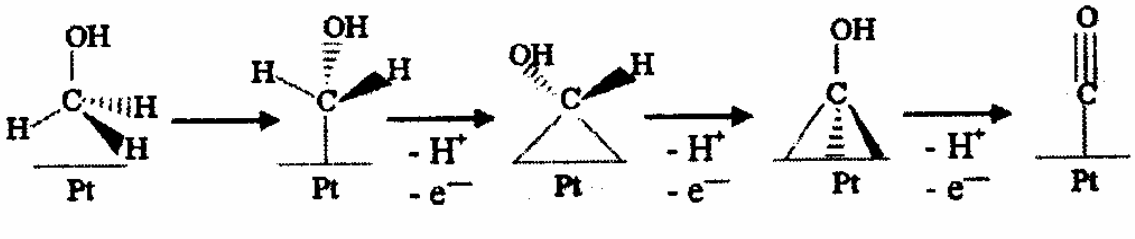

Figure 2.3: Scheme of methanol oxidation on Pt catalyst

The water in the fuel oxidizes the CO adsorbed at the surface to CO_2. Before being oxidized, the CO molecules can block the Pt surface and hinder the catalysis of further reactions. For this reason, a number of other metals have been examined as co-metals to the Pt catalyst to facilitate the CO oxidation and removal (16,17). The most investigated co-metal is ruthenium. A bimetallic alloy of Pt and Ru supported on carbon is commonly used as an anode in these studies.

2.3.2 Oxygen Reduction

The hydrogen ions transferred from the anode to the cathode through the PEM react with oxygen to generate water vapor. The oxygen reduction reaction is:

$$\tfrac{1}{2}\, O_2 + 2H^+ + 2e^- \rightarrow H_2O \qquad \Delta G = -228.572 \text{ kJ/mol}, \Delta U_o = 1.184 \text{ V} \qquad (3)$$

Platinum can also be used as a catalyst to reduce oxygen at the cathode. The adsorption of the oxygen species on the surface of the catalyst particles is necessary for electron transfer. The reduction reaction can occur by two methods in aqueous electrolytes, a direct 4-electron pathway and an indirect 2-electron pathway (18,19). The overall resistance of oxygen reduction can be divided into three contributions: the diffusion of oxygen into an external water film on the catalyst, internal diffusion in the porous Pt catalyst, and the intrinsic reaction rate on the Pt surface (20).

2.3.3 PEM and Methanol Crossover

Polymer electrolyte membranes (PEM) can be used in low-temperature fuel cells that operate with either hydrogen or methanol (21). The solid membrane is usually a

perfluorinated polymer with sidechains terminating in sulfonic acid moieties, such as Nafion by Dupont. Membranes in PEM fuel cells generally contain water to keep the conductivity high. The water content of the membrane dictates the upper temperature limit. A dried-out membrane has a lower conductivity to protons, because proton transport in the PEM is similar to in an aqueous solution. For every proton, a shell of H_20 is also transported through the membrane. Therefore, a high electro-osmotic drag on the water can reduce the proton conductivity, and thus the performance of the fuel cell.

Methanol crossover occurs in direct methanol PEM fuel cells and is one of the biggest obstacles to increased performance and fuel efficiency. The proton transport across the membrane is facilitated by water, keeping the water content of the membrane high. Because methanol has similar properties as water, it is also transported across the membrane to the cathode, where it has been shown to have a poisoning effect on the oxygen reduction reaction (22). The methanol takes up adsorption sites on the catalyst, decreasing the number of sites for oxygen reduction. Also, the methanol oxidation causes a mixed potential with the oxygen reduction reaction. This, along with the conversion losses in terms of wasted fuel, decreases the performance of the fuel cell.

The factors that contribute to methanol crossover include membrane permeability and thickness, methanol concentration of the fuel, fuel flow rate, operating temperature, cathode air pressure, and anode performance (23-25). Reducing the thickness of the PEM gives lower resistance to both proton and methanol transport. Increasing the temperature or the concentration of methanol increases diffusion through the membrane. Also, improving the anode activity will oxidize more methanol, which decreases the amount of methanol available for crossover.

Choi et. al. (26) studied the effect on methanol crossover of modifying the PEM using two techniques common in microelectronics process. The PEM was plasma etched with argon and/or sputtered with palladium. The plasma etching was shown to increase the roughness of the surface and decrease the methanol permeation. A thin layer of palladium sputtered on an etched or non-etched membrane was shown to further decrease the methanol crossover without decreasing the proton transfer rate.

2.3.4 Performance

Figures 2.4 and 2.5 show graphs for the performance of direct methanol fuel cells (27). Figure 2.4 shows the power density curves for a thin-film catalyzed Nafion 112 DMFC assembly operating with oxygen at the cathode at 130ºC and with air at the cathode at 110ºC. The conditions were controlled to ensure saturated vapor conditions of the 1 M methanol fuel solution. Figure 2.5 shows the effect of operating temperature on the current density. The data is for a cell potential of 0.5 V, oxygen cathode at 130ºC and 1 M methanol at saturated vapor conditions.

2.4 Micro-electromechanical Systems

Micro-electromechanical systems (MEMS) incorporate various mechanical elements, sensors, actuators, or fluidics built onto a silicon substrate through microfabrication technology. MEMS is an enabling technology that allows for the miniaturization of a number of different products. This research focuses on using these miniaturization techniques to fabricate fuel cells. Discussed below are the microelectronic or MEMS fabrication processes that are utilized and the possible advantages to an integrated power source and electronic device.

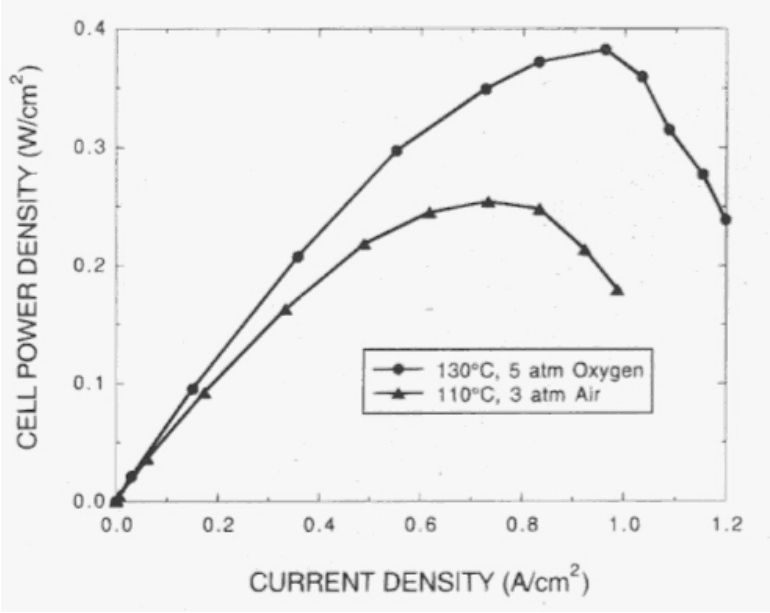

Figure 2.4: Power density curves for a DMFC

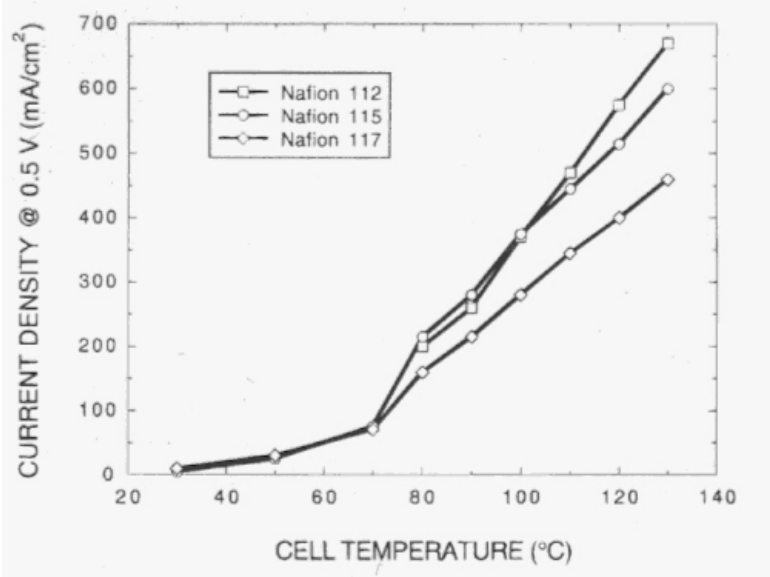

Figure 2.5: Effect of cell temperature on current density of DMFC

2.5 Microchannel Development

The micro fuel cell channels will be fabricated using novel microfabrication techniques and materials previously developed (28,29). A pictorial view of the process is shown in Figure 2.6. Several sacrificial materials have been found which decompose at temperatures ranging from 220°C to 400°C. The sacrificial polymer (e.g. functionalized polynorbornene (PNB)) is patterned followed by full encapsulation by the PEM. The figure shows the current procedure, which features the application and patterning of a hard mask before the reactive ion etching (RIE) of the PNB. Development of a photo-definable form of sacrificial polymer (SP) would greatly reduce the number of steps this process. After depositing the overcoat material, the composite is heated to its decomposition temperature where the polymer undergoes decomposition and its products diffuse out of the channel through the permanent dielectric. Further, the polymer decomposition products must permeate through the superstructure. Figure 2.7 shows the cross section of an air-channel with a width of 140 μm and a polyimide overcoat (Amoco Ultradel 7501). Figure 2.8 shows an air-channel fabricated between copper lines, which would become the anode current collector.

2.6 Thin-film Proton Exchange Membranes

Compared to conventional fuel cells, a PEM in a microfabricated fuel cell should be thin to match the thickness of the other materials, such as insulators on electronic devices. The use of an alternate membrane material with a higher resistance to methanol crossover and less dependence on water concentration is desired for thin-film membranes. The ionic conductivity, however, can be lower because the film is thinner.

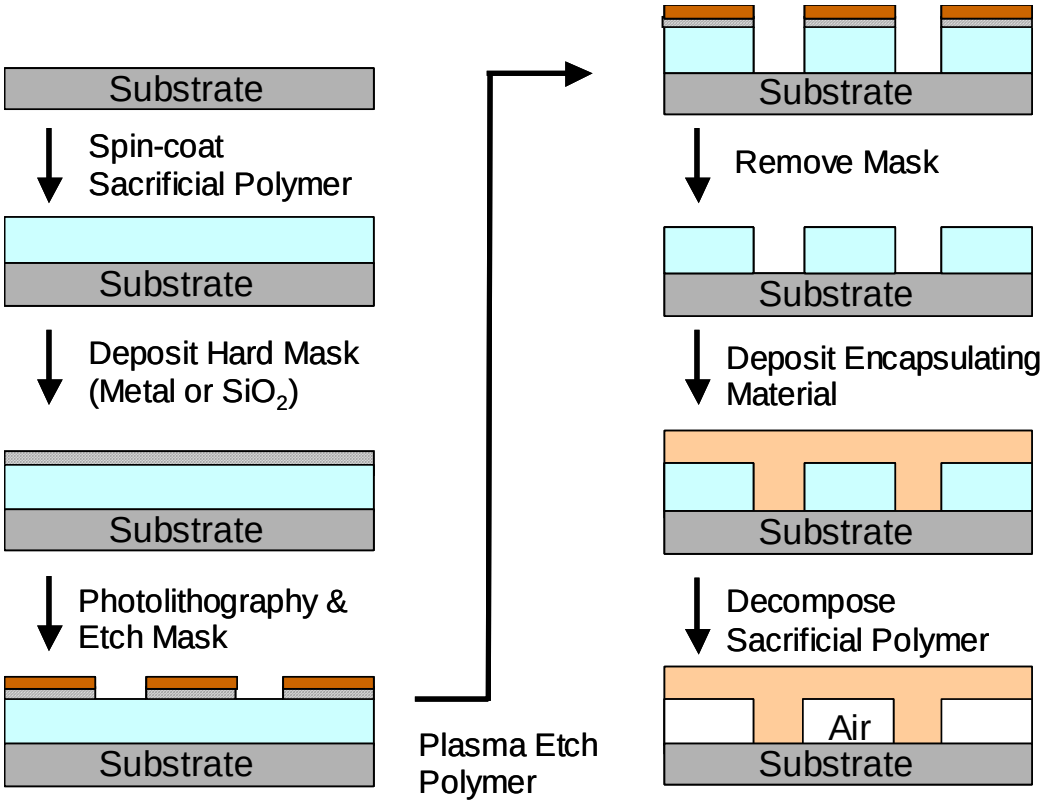

Figure 2.6: Microchannel formation process

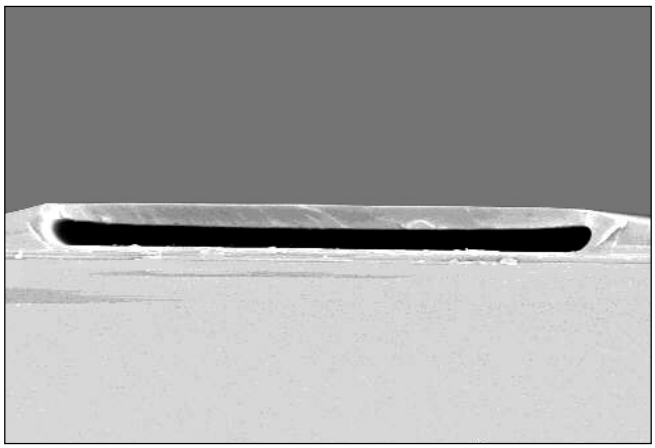

Figure 2.7: Air-channel encapsulated in Amoco Ultradel 7501

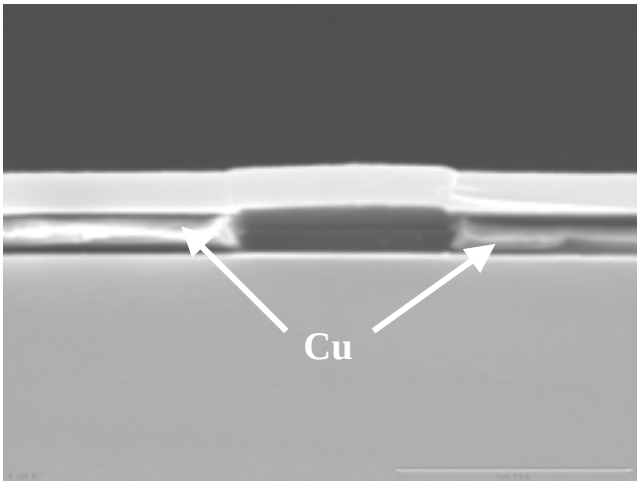

Figure 2.8: Air-channel fabricated between copper lines

Polymers that have been studied for use as a PEM in microfabricated fuels cells include Nafion, polybenzimidazole (PBI), and poly phenylene sulfonic acid (4, 30-31).

The deposition temperature of PECVD silicon dioxide has been shown to have a large effect on silanol and water concentrations in the film, leading to increased polarity and therefore higher ionic conductivity (32). The resistance to methanol permeation through inorganic glasses should be very high. In addition, the mechanical properties make it suitable for use in the thin-film design being used, making it an attractive alternative to be studied.

The main factor for proton conduction in glass appears to be the strength of O – H bonding. In silica glasses, the O – H bonding is typically strong, leading to a low mobility of H+, but in phospho-silicate glass (PSG), the O – H bonding is weak due to strong hydrogen bonding (33). In addition, the proton conductivity in phosphate glasses has been shown to be proportional to the square of the proton concentration (34). Studies of proton conduction has been made in a number of melt glasses of the form $MO \cdot P_2O_5$ (M = Be, Mg, Ca, Sr, Ba, etc.), in which small amounts of water in the form of – OH groups exist instead of alkali metal ions (35-36).

2.7 Sputtered Catalyst

Another important topic to investigate in microfabricated fuel cells is decreased catalyst loading. Pt-Ru alloy catalysts are the most efficient anode catalysts for methanol electro-oxidation (37-39). The addition of Ru to the Pt catalyst enhances the rate of methanol electro-oxidation because the Ru provides a site for water oxidation and OH adsorption needed in oxidation of methanol to CO_2. The availability of adsorbed OH on

the Ru lowers the number of CO intermediates on the Pt (40-43). In a typical DMFC, the anode catalysts are generally present in the form of nanoparticles supported on high surface area carbon in contact with the membrane (40, 44-46). Sputtering the metal catalyst allows for very low catalyst loading because of the size of the deposited particles in the island growth stage of film deposition. Dobierzewska-Mozrzymas et. al. studied the conduction mechanisms in discontinuous Pt films with different coverage coefficients (47). The films made by evaporation had a very high resistance when the coverage coefficient was less 0.5. Above 0.5, the resistances indicated that the films were porous, but there were metallic paths across the films. The advantages to sputtering the catalyst include the lower Pt loading (48) because of the higher surface area to weight ratio and a reduction in methanol crossover due to better coverage (26). Depositing a single layer of catalyst onto the membrane limits the amount of catalyst that can be deposited, because the film must remain porous to allow reactants to contact the membrane. The anode reaction must occur at the interface between the catalyst and electrolyte membrane for the protons to be transported to the cathode, where they subsequently are consumed in the cathode reaction where the membrane and catalyst are in contact. A fabrication technique that can increase the amount of sputtered catalyst while maintaining porosity for reactant access to the membrane can be an important factor in improving cell performance.

2.8 Integrated Power Supply

Today, hybrid devices are used. Each component is separately made and packaged, and then interconnected. An integrated power supply is one that would be

fabricated and packed with the electronic device. The advantages of this technology to the traditional hybrid approach would include:

- The common packaging would reduce the large sizes and excess weight of separately packaged devices.
- A reduction of interconnection problems due to the need for external connectors and loss of signal integrity due to long path lengths for critical signals, especially those between sensors and amplifiers.
- Increased processing efficiency by co-fabricating components that are common to different devices, such as metals and dielectrics.
- An efficient heat management scheme among different devices, because some devices generate waste heat and others require heat.
- Matching of power output and usage can be realized. In mismatched devices, the capabilities of one are not optimally matched to the others, resulting in further increases in weight and size vs. performance because some components will be oversized.

Figure 2.9 shows a schematic diagram of an IC with an integrated micro fuel cell. This design shows the fuel being vaporized by waste heat, which will also serve to cool the integrated circuit. The other processing and packaging advantages listed above may also be realized with this type of device.

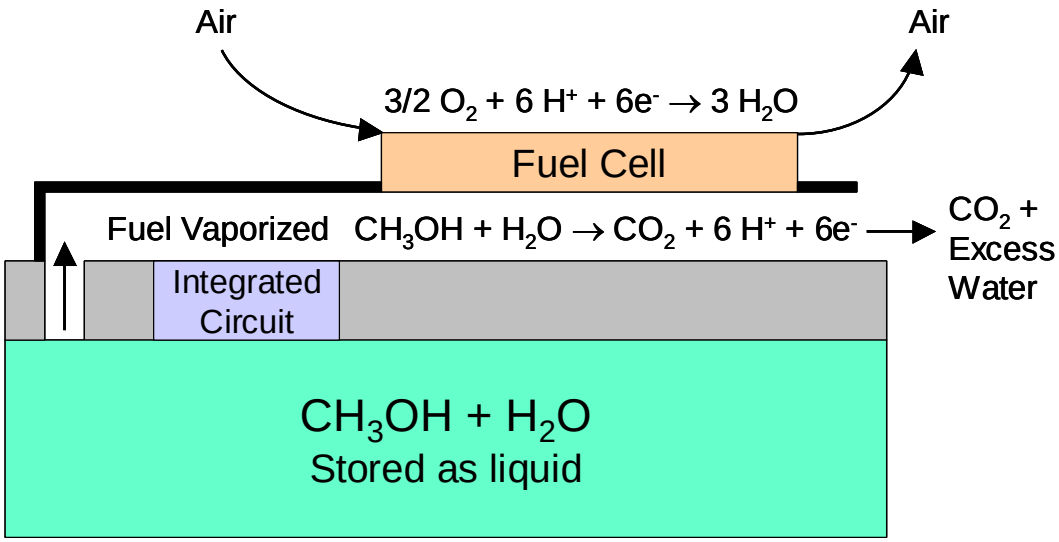

Figure 2.9: Schematic diagram of integrated micro fuel cell

CHAPTER 3

EXPERIMENTAL METHOD

3.1 Microchannels

The design and fabrication of the micro fuel cells is based on a technique of using a sacrificial polymer to form the fuel delivery channels for the anode (28, 29). The membrane and electrodes coat the patterned features in a sequential buildup process. One of the last steps in the fabrication sequence is the thermal decomposition of the patterned Unity features, leaving encapsulated microchannels. Figure 3.1 shows the process sequence for fabricating the enclosed air gaps, or microchannels, in an encapsulating material. This sacrificial polymer, Unity 2000P (Promerus LLC, Brecksville, OH), was patterned by ultraviolet exposure and thermal decomposition of the exposed areas. Unity decomposition took place in a Lindberg tube furnace with a steady nitrogen flow. The final decomposition temperature and time was 170°C for 1.5 hours. The micro fuel cell fabrication included deposition of catalytic electrodes and current collectors before and after the encapsulating material, which served as the PEM, was deposited. A schematic cross section of the device built on an array of parallel microchannels is shown in Figure 3.2.

3.2 Sputtered Metals

All metals, including the catalyst layers, were sputter deposited using a CVC DC sputterer (CVC Products, Inc., Rochester, NY). Pure metal targets that were used included platinum, gold, titanium, and aluminum. A 50:50 atomic ratio platinum/ruthenium target (Williams Thin-Film Products, Brewster, NY) was also used

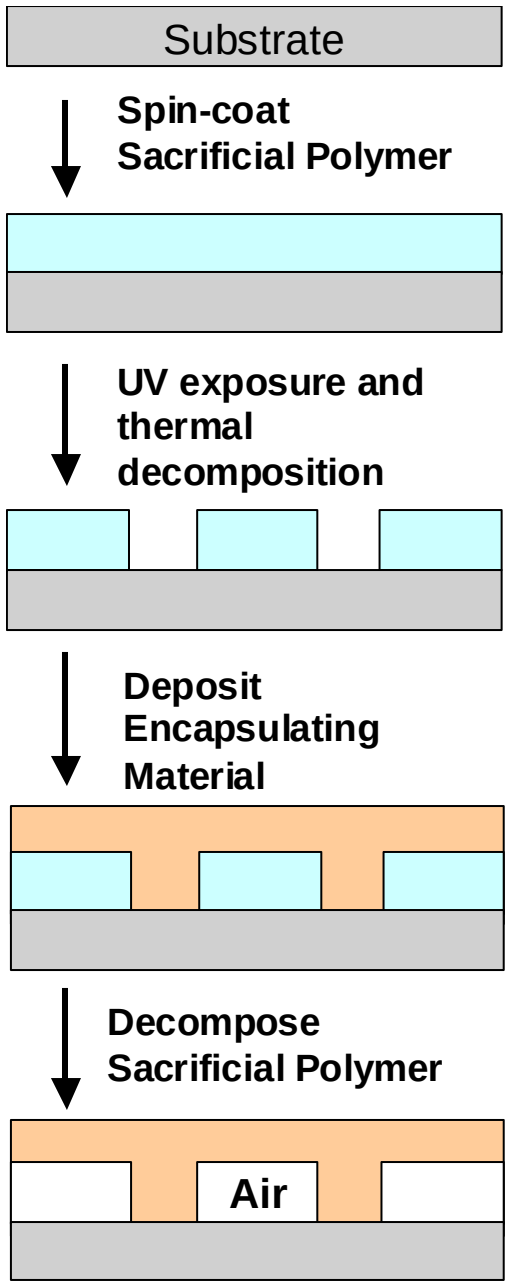

Figure 3.1: Microchannel formation process with a photo-definable sacrificial polymer

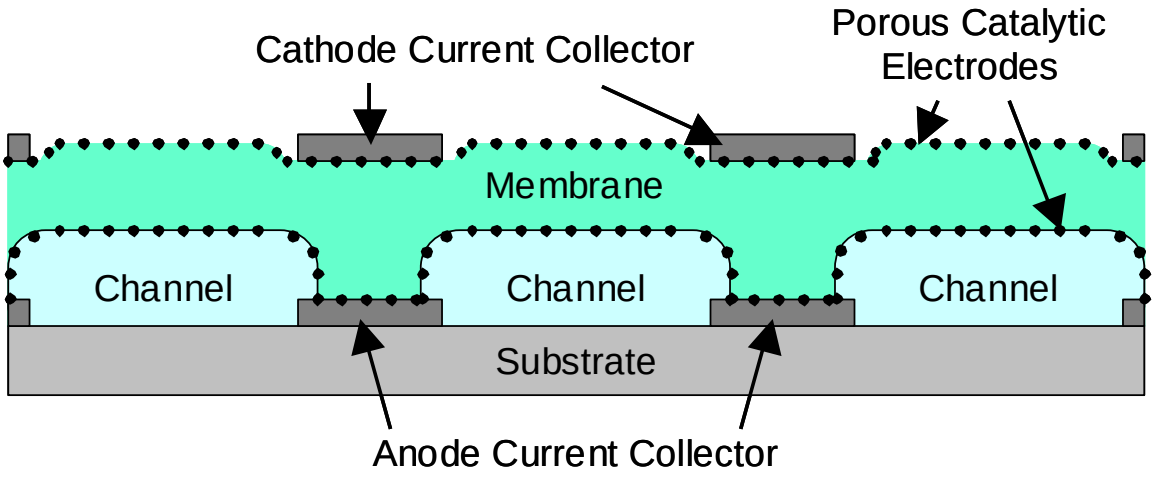

Figure 3.2: Cross-section of a thin-film fuel cell with parallel microchannels

as a catalyst source target. Porous films of either Pt or Pt/Ru with average thicknesses of 50-200 Å were deposited on the sacrificial polymer, and then coated with the membrane, to serve as anode catalysts. In addition, a 600 Å thick layer of Pt/Ru was deposited on the bottom of the anode microchannels opposite the membrane to serve as both additional catalyst and for current collection. This additional catalyst improved the performance of the microchannel fuel cells, particularly when using acidic methanol.

3.3 Silicon Dioxide Membranes

Silicon dioxide was used as the encapsulating material and PEM. The deposition of SiO_2 took place in a Plasma-Therm PECVD system (Plasma-Therm, St. Petersburg, FL) at temperatures of 60-200°C. The reactant gases were silane and nitrous oxide with a N_2O:SiH_4 ratio of 2.25 and operating pressure of 600 mTorr. Deposition times of 60-75 minutes produced film thicknesses, measured with an Alpha-Step surface profilometer (KLA-Tencor, San Jose, CA), between 2.4 and 3.4 μm.

Deposition of phosphosilicate glass (PSG) films took place in an Unaxis PECVD system (Unaxis, St. Petersburg, FL) at temperatures of 100-250°C. The reactant gases were nitrous oxide and a silane/phosphine mixture. The amount of phosphine in the mixture was 6% of the silane. Other parameters, such as N_2O:SiH_4/PH_3 ratio and RF power were varied and resulted in different deposition rates. PSG films between 1 and 2 μm were used for ionic conductivity tests with impedance spectroscopy. Thicker films, usually between 3 and 10 μm, were used as PEMs in the microfabricated fuel cells.

3.4 Membrane conductivity tests

Two approaches taken to test the conductivity of thin-film membranes were through the use of impedance spectroscopy and direct ionic conductivity. Impedance spectroscopy was performed on samples of the membrane materials that were deposited onto a layer of metal. Meanwhile, the ionic conductivity measurements required that both sides of the membrane were exposed.

Impedance spectroscopy is a method to measure the conduction of ions in a film by comparing the real impedance to imaginary impedance over a range of frequencies. The films were deposited onto a metal layer, and then placed on a mercury probe such that the mercury came in contact with the deposited film to measure the conduction from mercury to the metal layer through the film. The potentiostat was connected to the mercury probe and swept through frequencies from 2 GHz to 100 Hz, with an AC signal amplitude of 10 mV.

Because impedance spectroscopy measured the conductivity of ions in the film and not specific ions through the film, a different method was additionally used for the collection of data that will more accurately simulate the membranes' use in a fuel cell and validate the use of impedance spectroscopy. A difficult aspect of this process was to find a way to properly support such delicate films while exposing both sides in an electrochemical cell. Two different support structures were used: porous glass frits and metal disks with drilled holes. Figure 3.3 shows the process for preparing a supported membrane on the structures through the use of a filler material, deposition of the membrane, and removal of the filler.

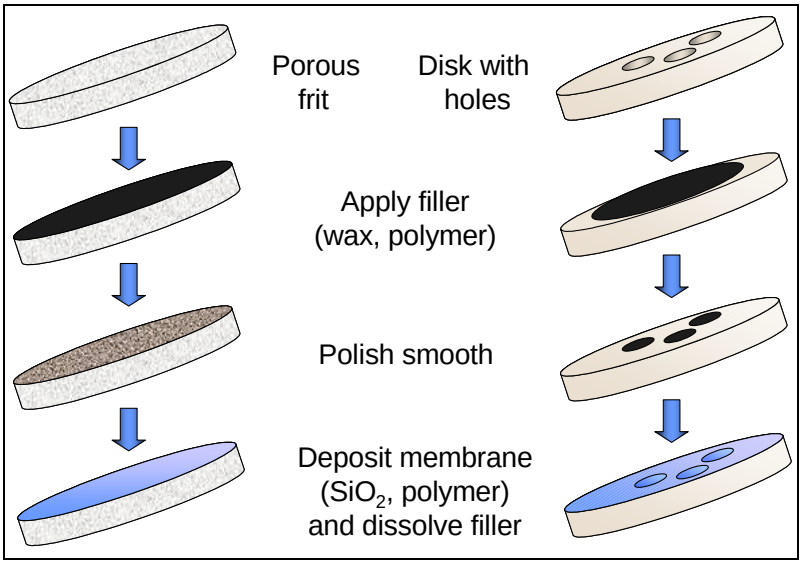

Figure 3.3: Membrane support structures

Supported membranes were placed between two vials containing 2.0 M KCl solution as shown in Figure 3.4. A potential was applied across the platinum wires resulting in a flux of protons through the membrane. The resistance of the membrane was calculated by subtracting the solution's resistance from the total resistance.

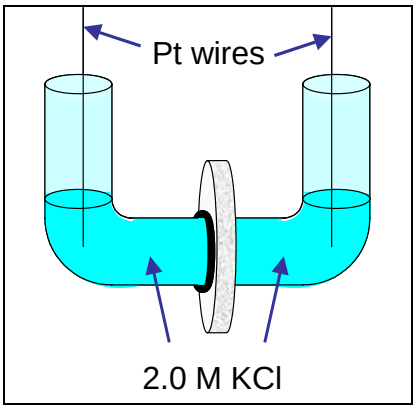

Figure 3.4: Electrochemical cell to measure membrane resistance

3.5 Membrane-Electrode Assemblies

In order to test the performance of the silicon dioxide membranes and sputtered catalyst, membrane-electrode assembly (MEA) test structures were made as shown in Figure 3.5(a). Aluminum disks with 1-mm^2 holes were used as a rigid support for the gas diffusion layer (GDL), which was a flexible, cloth-like material. Additionally, GDLs were epoxied to silicon wafers with etched channels and through holes for backside fuel delivery. The GDL was coated with Nafion, and polished smooth to make a flat surface for catalyst and membrane deposition. Pt or Pt/Ru catalyst was sputtered, followed by silicon dioxide depositions by PECVD at relatively low temperatures (80-150°C). The half-cell measurements were taken with the setup shown in Figure 5.18(b) and a potentiostat.

Methanol, hydrogen, or air was passed by the catalyzed GDL, while a solution of 2 M H_2SO_4 with the counter and reference electrodes was on the other side of the membrane. The potentiostat measured the current vs. potential. Voltages were measured vs. a standard calomel electrode (SCE).

3.6 Thick-film Catalyst Ink Cathodes

Porous catalytic cathodes were also fabricated by sputtering of Pt or Pt/Ru on the top, or outside, of the PEM. However, the cathodes on some samples were made by painting a prepared catalyst ink containing carbon-supported Pt in Nafion on the PEM, followed by coating with a porous gold current collector. This thick-film approach increased the catalyst loading and performance on the cathode side of the PEM. This was especially useful in studying the anode performance by eliminating the oxygen reduction at the cathode from being the rate-limiting step.

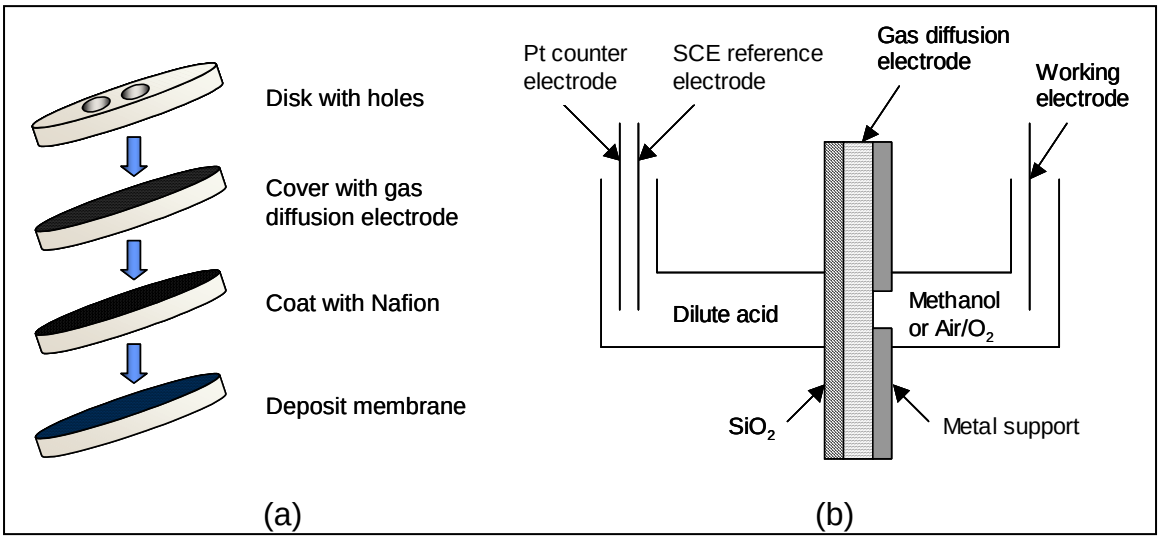

Figure 3.5: Test structure fabrication (a) and electrochemical testing setup (b)

3.7 Tube attachment and fuel delivery:

After device fabrication, wafers were split into individual chips to be tested. PEEK micro tubing was attached to the opened inlet holes using a microscope and alignment marks in the overcoat material made during the last photolithography step. The anode and cathode contact pads were wire-bonded to a packaging substrate as shown in Figure 3.6. Flow of both liquid and gas through the microchannels was demonstrated with each of the sacrificial polymers and various encapsulating materials, including polymers and silicon dioxide.

After being connected to the microchannels, the tubing was then attached to either a pressurized gas cylinder or a syringe pump to flow gas or water through the channels. A pressure sensor was placed in line between the pump and microchannel substrate to measure pressures.

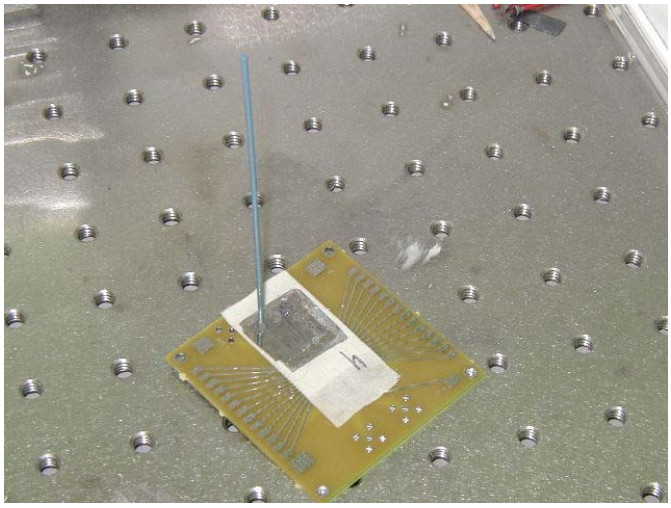

Figure 3.6: Micro fuel cell prototype with attached fuel delivery tube and wire-bonded to testing substrate

3.8 Electrochemical Testing

All electrochemical measurements, including impedance spectroscopy (IS) and linear voltamagrams, were performed with a PerkinEkner PARSTAT 2263 (EG&G, Princeton, NJ) electrochemical system. The scan rate for linear sweep voltametry was 1 mV/s. Ionic conductivity was measured with impedance spectroscopy through SiO_2 films deposited onto aluminum-coated substrates and contacted with a mercury probe, as well as with actual cells. Half-cell devices were fabricated with the fuel delivery channels and sputtered catalyst under the SiO_2 PEM. Instead of a cathode, epoxy was used to form a well on top of the devices and filled with a 1 M sulfuric acid solution. Measurements were made with a saturated calomel electrode (SCE) and a Pt wire as the reference and counter electrodes, respectively, placed in the sulfuric acid solution.

Figure 3.7 shows a picture of the key components of the device testing setup that was used to test the fuel cells with methanol. A PHD 2000 Programmable Syringe Pump (Harvard Apparatus, Holliston, MA) delivered liquid fuels and controlled the flow rates. Hydrogen was supplied with a pressurized tank of ultra high purity grade gas that passed through a bubbler to humidify the feed. The tubing was polyetheretherketone (PEEK) with an outside diameter of 1/16" and an inner diameter of 150 μm. A pressure transducer was placed in the line to measure the pressure as close to the microchannel inlet as possible. The devices were placed in the oven during testing to control the temperature. Figure 3.8 shows a schematic diagram of the setup with both the syringe pump and hydrogen cylinder connected. With this configuration, the tubing could be filled with hydrogen, then pushed into the micro fuel cells by the syringe pump.

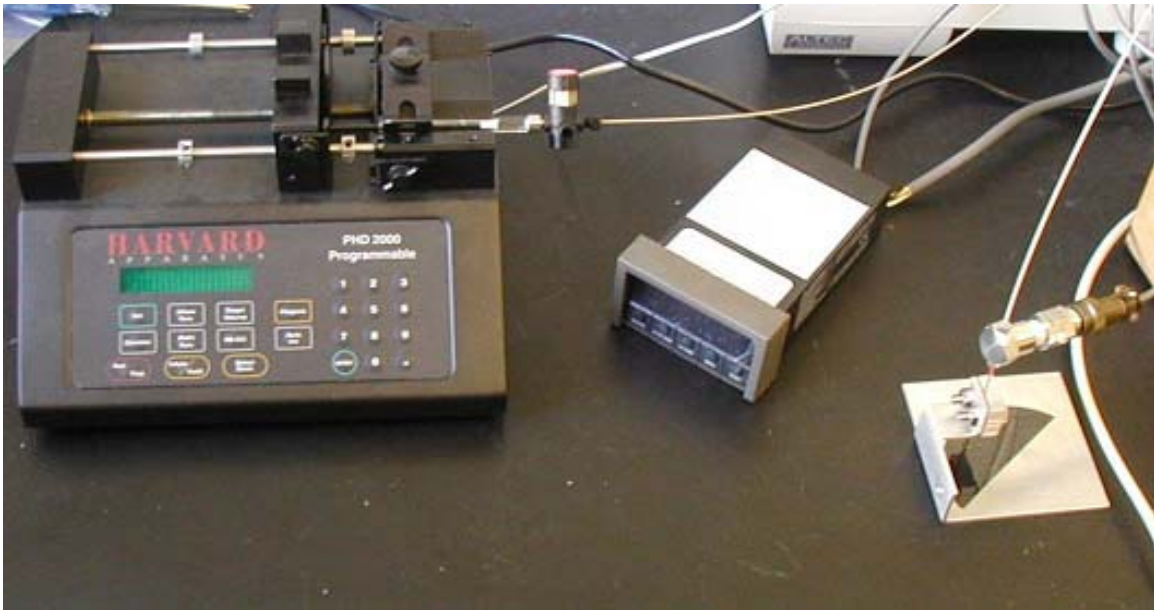

Figure 3.7: Experimental setup to test micro fuel cells

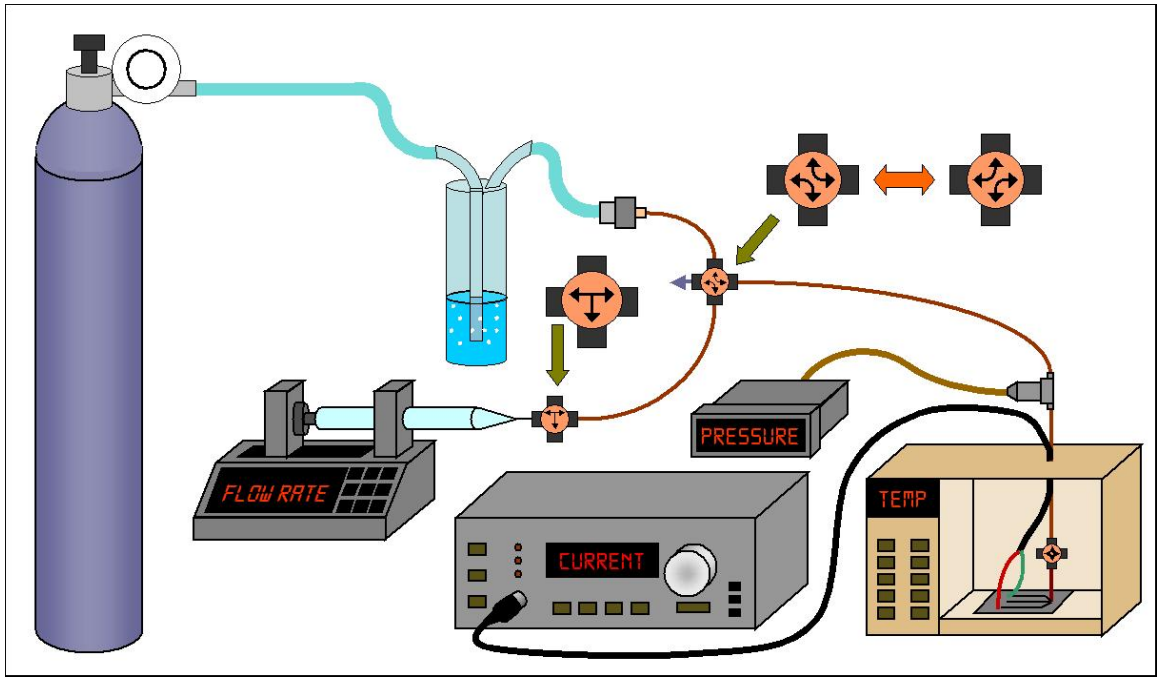

Figure 3.8: Experimental setup to test micro fuel cells

3.9 Deep Silicon Etching

Deep silicon etching to make holes or channels in the silicon wafers was performed using a Plasma-Therm inductively coupled plasma (ICP) RIE system (Plasma-Therm, St. Petersburg, FL) using the Bosch process. AZ P4620 photoresist (AZ and city) was used as an etch mask. Typically, the etch rate in silicon was approximately 50 μm per hour.

3.10 Gold electroplating

Gold electroplating took place in a bath containing $KAu(CN)_2$, K_2HPO_4, and H_3PO_4 in de-ionized (DI) water at 45-50°C. The counter electrode was Pt. The current density was approximately 4 mA/cm2, which resulted in a deposition rate of about 15 μm/hr. AZ P4620 (AZ Electronic Materials, Somerville, NJ) was patterned over a sputtered gold seed layer in order to plate only in the exposed areas.

CHAPTER 4

DESIGN

4.1 Introduction

In this chapter, the basic design elements developed early in the project lifetime are presented. These include calculations for fuel flow through microchannels based on the physical state of the fuel and size of channels; ideas on the way the cells were to be built up on the substrate and incorporated into an integrated self-powered device; the effect of current density, flowrate, and fuel concentration on waste heat production and cell temperature, and finally some early experimental results comparing pressure drop and flow rates through microchannels to the calculations.

4.2 Fuel flow scenarios

The design of micro fuel cell devices uses the experimental results for current and power densities to maximize fuel utilization through the sizing of microchannels. Because of the different types of fuel that can be used, as well as different operating temperatures, which can affect the nature of the fuel (liquid or vapor), three different basic design scenarios are considered. These are:

1. Plug flow with no fuel outlet
2. Single-pass flow in channels
3. Re-circulating flow in channels

4.2.1 Scenario 1: Plug flow with no fuel outlet

The plug flow without a fuel outlet design would be suitable for the use of pure hydrogen because the oxidation of hydrogen does not produce bi-products. The microchannels could be constructed in such a way that a relatively constant pressure of hydrogen is present at all parts of the membrane/catalyst surface. In addition, the pressure can be held fairly high compared to a device with an exit stream in order to take advantage of improved kinetics and minor pressure drop down the length of the channels. Sizing of the channels requires simply dividing the desired power by the power density from experimental results.

One concern with this scenario is the humidification of the hydrogen fuel. Humidified hydrogen helps keep the conductivity high in polymer membranes. The increased resistance of dried-out membranes result in poor cell performance. A small amount of water may need to be stored and used to humidify the hydrogen feed before or as it enters the micro fuel cell.

4.2.2 Scenario 2: Single-pass flow in channels

The single-pass flow of fuel through the microchannels is also a simple design, but allows for the exit of by-products and unreacted fuel. This is necessary when using methanol because its oxidation produces carbon dioxide. Also, methanol fuel usually has excess water, which must also be released. In order to achieve high fuel utilization, the concentration of methanol must decrease along the length of the microchannels as it approaches the end. Also, because carbon dioxide is gaseous, a vaporized fuel is preferred. Otherwise, gas bubbles in the microchannels will increase the pressure as

methanol is oxidized and also cover catalyst sites. The design of these channels for liquid fuel will incorporate experimental data to determine the correct sizing.

4.2.3 Scenario 3: Re-circulating flow in channels

The re-circulating flow of fuel would be a more complicated system to build, especially on the micro-scale, but will be considered from a theoretical standpoint for design purposes. The advantages to a recirculating design, which is most commonly used for direct methanol fuel cells, includes the ability to use a relatively dilute, liquid methanol fuel in the fuel cell to decrease methanol crossover, while re-using the water so that only stochiometric amounts of methanol and water are added to the stream. The carbon dioxide produced can be removed as part of the recirculation system.

4.2.4: Fuel and design choice

Methanol, stored in liquid form, was determined to be more efficient and convenient than the storage of hydrogen, as pressurized gas or in metal hydride form, for small form factors. While the micro fuel cell prototypes would be tested with both hydrogen and methanol, the design and fabrication would follow the single-pass flow scenario. One of the key features of the design and experimental work with methanol was the concentration of the fuel. While the concentration affects the amount of energy that can be stored in a given volume, it also may affect the state of the fuel, as discussed further below. One goal, through high fuel concentration and utilization, was to generate and maintain enough heat to vaporize the fuel as it passed through the microchannels.

4.3 Flow Calculations

The shapes of the fuel delivery microchannels are rectangular in cross-section because of the nature of microelectronic processing. Because of the sizes being considered, flow calculations will be based on laminar flow in tubes (49). Laminar flow is defined as being the regime where the Reynold's number is less than 2100, where the Reynold's number (Re) is given by:

$$\mathrm{Re} = \frac{D\nu\rho}{\mu} \qquad [4.1]$$

where D is the diameter, ν is the average velocity of the fluid, ρ is the fluid density, and μ is the fluid viscosity. The friction factor (f) for laminar flow in tubes is given by:

$$f = \frac{16}{\mathrm{Re}} \qquad [4.2]$$

For a given length of tube, L, the pressure drop, ΔP is given by:

$$\Delta P = \frac{2L}{D}\rho v^2 f \qquad [4.3]$$

Because the microchannels have a rectangular cross-section, the hydraulic diameter, D_H, is substituted for D. D_H is defined as:

$$D_H = \frac{4A}{P_w} \qquad [4.4]$$

where A is the cross-sectional area and P_w is the wetted perimeter. For a rectangular tube, the D_H is related to the width, w, and height, h, by:

$$D_H = \frac{2wh}{(w+h)} \qquad [4.5]$$

Therefore, the pressure drop for laminar flow through a microchannel with a rectangular cross-section is given by:

$$\Delta P = \frac{L(w+h)}{wh} \rho v^2 f \qquad [4.6]$$

4.4 Experimental Confirmation of Pressure Drop Calculations

Microchannels were fabricated on silicon wafers using sacrificial polymers and other microelectronic processing techniques. There were connected to a syringe pump and pressure transducer with polymer tubing. The pump supplied a given flow rate of water while the pressure transducer reported the pressure in psig of the water in the tubing before it entered the microchannels on the wafers. The opposite ends of the microchannels were opened for exiting water. Therefore, the pressure reading in psig was taken as the pressure drop in the channels. The dimensions of the microchannels were 100 μm wide by 10 μm tall with a length of 1.5 cm. Table 1 and Figure 1 show the

results from three samples tested along with the calculated values based on the equations above. The data supports the theoretical laminar flow calculations, so therefore the above equations will be used for design and sizing of channels.

Table 4.1: Pressure drop in microchannels

Flow rate (μL/min)	Velocity (m/s)	Reynold's Number	Friction Factor	Pressure Drop			
				Calculated	Sample 1	Sample 2	Sample 3
0.21	0.0035	0.124	128.6	0.39	0.6	0.7	0.6
0.43	0.0071	0.249	64.3	0.77	1.1	1.0	1.2
0.64	0.0106	0.373	42.9	1.16	1.4	1.5	1.7
1.06	0.0177	0.622	25.7	1.93	1.9	1.8	2.0
1.70	0.0283	0.996	16.1	3.09	3.6	3.7	3.9
2.13	0.0354	1.24	12.9	3.86	4.4	4.4	4.6
2.76	0.0461	1.62	9.89	5.02	5.7	5.5	5.8
3.40	0.0567	1.99	8.03	6.18	6.1	5.9	6.3
4.25	0.0708	2.49	6.43	7.72	6.6	6.7	6.9
5.31	0.0886	3.11	5.14	9.65	7.8	7.6	7.9

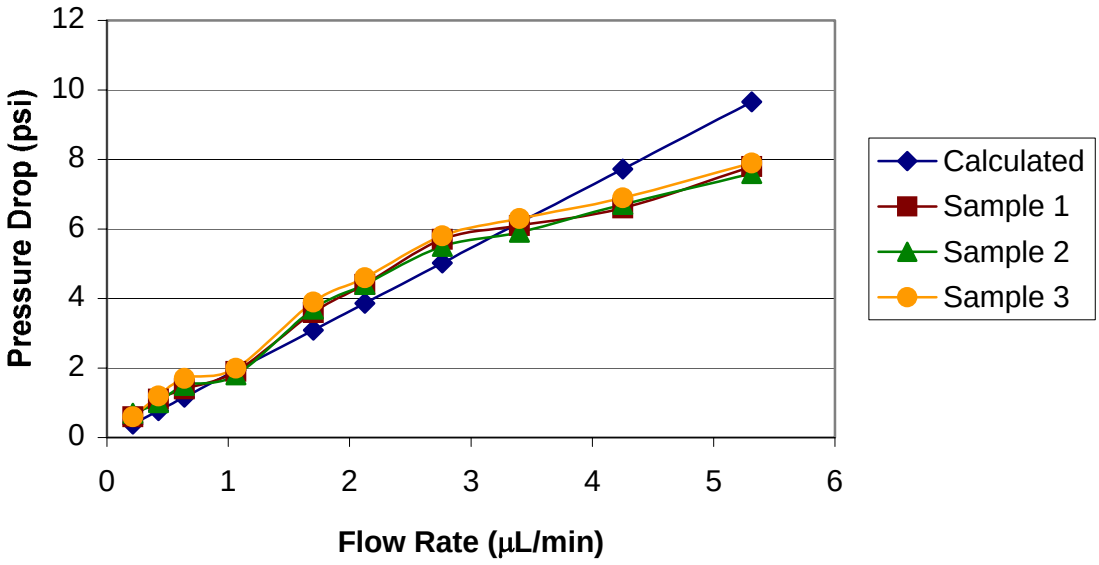

Figure 4.1: Pressure drop in microchannels

4.5 Current Density and Flowrate

Current density from measured micro fuel cells is used to calculate the necessary flowrate for fuels through the microchannels. Faraday's constant, *F*, relates the amount of charge passed in Coulombs, *C*, to the number of moles of reacted species and the number of equivalents, *eq*, per mole by the following equation:

$$C = mol_{reacted} \times \frac{eq}{mol} \times F \qquad [4.7]$$

where F = 96,485 *C/eq*. Because current is charge passed per unit time, reported in Amperes, *A*, that equals one Coulomb per second, *C/s*, the Flowrate in moles per second is a direct comparison. For methanol in water fuel, the number of moles is determined by the volumetric flowrate and the concentration of the fuel in moles/Liter, or molar, M.

Table 4.2 shows calculated values for the flow rates and velocities of liquid and gas methanol and water mixtures in microchannels with different widths and heights. The lengths of the channels are 1.0 cm and the pressure drop is 1 atm, or 14.7 psi. The values listed for current are for a 1.0 M solution with all of the methanol reacting. Table 4.3 shows values for the same calculations, except that the pressure drop is 1.0 psi.

For fuel cell operation with hydrogen, it was determined that the feed would be humidified. Table 4.4 gives the percent water concentration for a fully humidified feed entering the cell at 1 psig, or 15.7 psia. With increasing temperature, the percent of water increases sharply reducing the amount of hydrogen enters the microchannel. The flow rate and expected current for full conversion are based on channels 100 μm wide, 10 μm tall, and 1.0 cm long.

Table 4.2: Calculated flow rates and maximum currents for 1.0 M methanol in 1.0 cm long microchannels with a pressure drop of 1.0 atm

Channel		Liquid			Vapor		
Width (um)	Height (um)	Flow rate (ug/min)	Velocity (m/s)	Current (mA)	Flow rate (ug/min)	Velocity (m/s)	Current (mA)
1	1	0.0452	0.000754	0.00044	0.000871	0.0244	0.00001
10	1	1.43	0.00238	0.0138	0.0275	0.0770	0.0003
10	10	452	0.0754	4.37	8.71	2.44	0.084
100	10	14304	0.238	138.0	275	7.70	2.66
100	100	4523442	7.54	43,651	87100	244	840.5

Table 4.3: Calculated flow rates and maximum currents for 1.0 M methanol in 1.0 cm long microchannels with a pressure drop of 1.0 psi

Channel		Liquid			Vapor		
Width (um)	Height (um)	Flow rate (ug/min)	Velocity (m/s)	Current (mA)	Flow rate (ug/min)	Velocity (m/s)	Current (mA)
1	1	0.0031	0.000051	0.00003	0.00006	0.00166	0.000001
10	1	0.097	0.00016	0.0009	0.00187	0.00524	0.00002
10	10	30.8	0.0051	0.297	0.593	0.166	0.0057
100	10	973.4	0.0162	9.39	18.74	0.524	0.181
100	100	307801	0.513	2,970	592.7	1.657	5.72

Table 4.4: Calculated flow rates and maximum currents for fully humidified hydrogen in 1.0 cm long microchannels with a pressure drop of 1.0 psi

Temp (^{o}C)	Water (mol %)	Flow rate (μg/min)	Current (mA)
na	0.0%	2.84	4.52
20	2.2%	3.19	4.25
40	6.8%	4.36	4.21
60	18.4%	6.96	3.69
80	43.8%	12.66	2.54
100	93.6%	23.83	0.29

4.6 Overall Efficiency and Heat Evolution

The efficiency of a fuel cell is the amount of electrical energy produced compared to the total theoretical amount of energy available from the fuel being supplied. There are two components that are multiplied to get this number: the percentage of fuel used and the ratio of the operating voltage to the theoretical potential of the cell. While fuel utilization simply is a measure of the amount of fuel used, with the unreacted portion contributing nothing to the cell, not all of the energy produced by the reacting species is captured as electrical energy. A portion of it generates "waste heat." This comes from the difference in theoretical potential and the operating voltage. In a fuel cell with a theoretical, or open-circuit, potential of 1.2 V, the operating voltage may be closer to 0.4 V, meaning approximately twice as much waste heat energy is produced by the cell as electrical energy.

This heat can be used advantageously as the reaction kinetics are typically improved with an increase in temperature. For a direct methanol fuel cell with concentrated methanol fuel and a high efficiency, there could be enough heat to vaporize the fuel in the anode. Figure 4.2 shows the percentage of heat that must be retained in the device to vaporize a fuel stream as a function of the water:methanol molar ratio. The operating volage is set at 0.4 V. Calculations are shown for 100% fuel utilization (33% overall efficiency) and 50% fuel utilization (17% overall efficiency). Total heat, which includes the fuel cell waste heat and the heat generated by circuits using the electrical energy produced on an on-chip power device, is considered in addition to capturing only waste heat. In addition to retaining as much heat as possible in the device, the fuel must be highly concentrated and the utilization high in order to vaporize the feed.

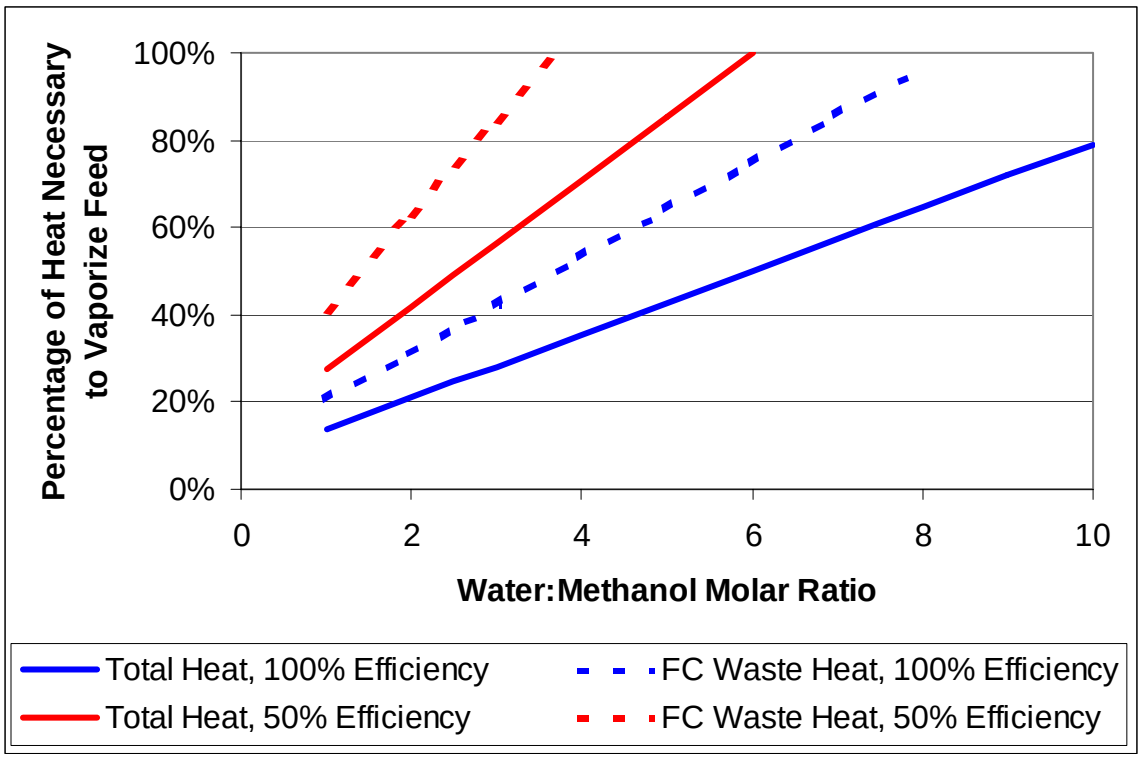

Figure 4.2: Heat retention necessary for fuel vaporization

4.7 Integrated fuel cells

The type of device in which microfabricated fuel cells usage was envisioned was one that integrated the micro power source with the electronic device that it would power. The advantages to this type of design include increased processing efficiency by co-fabricating components that are common to different devices, such as metals and dielectrics, as well as an efficient heat management scheme among different devices, because some devices generate waste heat and others require heat.

Figure 4.3 shows a schematic diagram of an integrated micro fuel cell/silicon CMOS/sensor technology. The fuel is stored in a collapsible unit that is under pressure from a piston. The piston, driven by a constant force spring, forces the fuel into the microchannels at a desired pressure. The fuel cell, fabricated over the microchannels, is located on the silicon substrate with the sensor device, a micro battery, and the controlling integrated circuit. A protective cover, or chimney, surrounds the top of the device to protect it, but features small, open windows in the side and top to allow air flow for the oxygen breathing cathode and the gas sensor. The overall size for such a device could be from less than 5 cm^3 to about 100 cm^3 with a stored fuel volume from 1 to 80 mL.

4.8 Conclusions

The initial design for the microfabricated fuels had to take into account the limitations of microchannel sizes for the materials used at that time along with assumptions and expectations of the power generation. During the course of the project, changes were made to the materials used, particularly the sacrificial polymer and

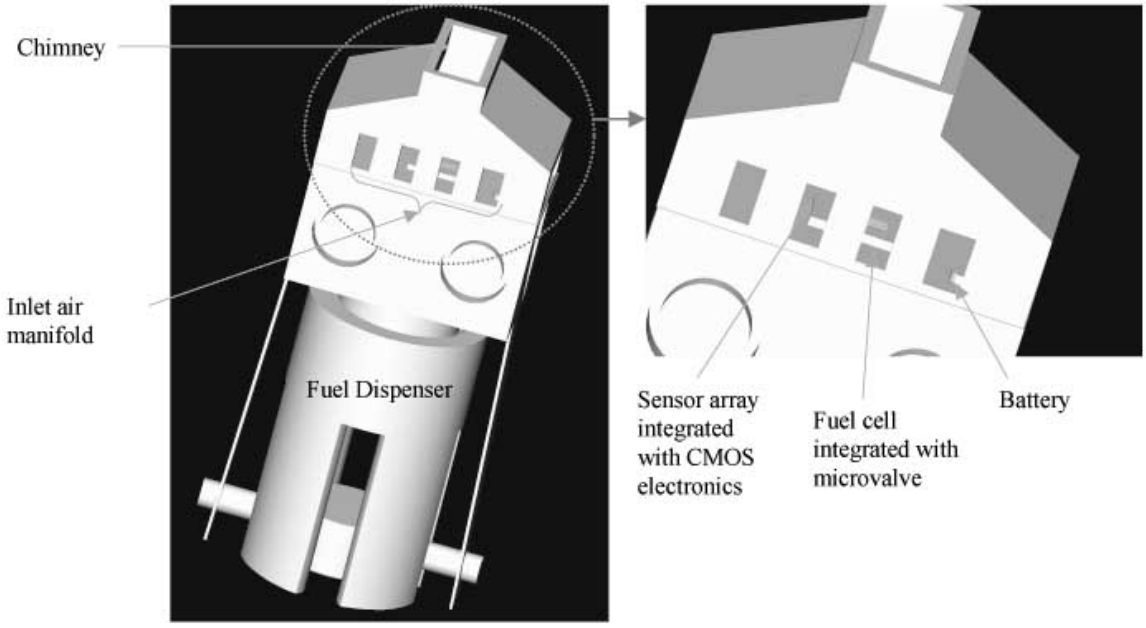

Figure 4.3: Integrated micro fuel cell/silicon CMOS/sensor technology

overcoat materials that increased the size, both width and height, of the fuel delivery channels. Testing results for power generation were obtained for a number of different parameters. Based on these results, additional changes had to be made to the design, particularly sizing and pressure drop values, to deliver the necessary fuel to be used. The following chapters give details on these issues and discuss the actual power generation and fuel efficiency obtained.

CHAPTER 5

FABRICATION

This chapter details many of the steps taken to develop the different parts of the microfabricated fuel cells. A main focus of the project was the investigation of sacrificial polymers to form microchannel for fuel delivery, including their patterning, decomposition, and compatibility with overcoat materials that would serve as the proton exchange membrane (PEM). Electrode and PEM materials are mentioned here, but also given more emphasis in later chapters.

5.1 Fabrication Process Sequence

The processing of complete devices using photo-definable polypropylene carbonate (PPC) as the sacrificial polymer, silicon dioxide as the overcoat/membrane, and sputtered Pt as the catalyst has successfully been performed. The complete process is given below:

Step #1: Anode current collector/contact

The metal in this step provides a low resistance path for electrons to be collected along the length of the fuel channel. It provides one level of metallization and is directly connected to the working electronic device (sensor/integrated circuit). Aluminum is sputtered on the silicon wafer containing the electronic circuits. The first fuel cell mask is patterned through photolithography and etching of the Al.

Step #2: Microchannel patterning

PPC is spin-coated and soft-baked on a hotplate. The thickness is about 20 micrometers. The PPC is exposed at 248-nm radiation through the second mask, generating acid to promote decomposition at a lower temperature. The PPC also serves as the insulator in the electronic circuit. The sample is heated on a 110°C hotplate for 5 minutes, which causes decomposition of the polymer in the exposed regions. Isopropyl alcohol is used to remove decomposition products from the surface, followed by an oxygen plasma de-scum in a reactive ion etcher.

Step #3: Anode catalyst

Platinum is deposited with a DC sputterer. Because of adhesion problems between Pt and the substrate, as well as between Pt and the overcoat material, a very small amount of titanium is sputtered as an adhesion layer below and above the platinum. The total metal layer is so thin, that is actually porous above the plasma-roughened polymer.

Step #4: Overcoat/membrane

Silicon dioxide is deposited through plasma-enhanced chemical vapor deposition (PECVD) at 100°C. The membrane thicknesses currently being deposited and tested are between 0.5 and 3.5 μm. This oxide will also serve as a dielectric for one metallization layer in the integrated circuit.

Step #5: Cathode current collector/contact

The metal in this step provides a low resistance path for electrons to be distributed along the length of the fuel channel. It also serves as another layer of metallization in the IC.

Aluminum is sputtered on the silicon dioxide and is patterned through photolithography and etching.

Step #6: Cathode catalyst

Platinum is again sputtered over the substrate with a titanium adhesion layer between the SiO_2 and Pt. A shadow mask covers the wafer with openings above the microchannels. The catalytic Pt layers will be deposited strictly for the fuel cell and will not be part of the circuit fabrication.

Step #7: Microchannel formation

The channels are formed by decomposing the sacrificial polymer with its degradation products diffusing through the overcoat, leaving encapsulated air gaps. For PCC, the samples are slowly heated in a furnace to 170°C for 1.5 hours. This heat cycle will also serve to cure dielectric material in the circuit if necessary.

Step #8: Inlet/outlet holes

Either reactive ion etching or a laser ablation tool can be used to pierce holes in the SiO_2 at each end of the microchannels for tube attachment to allow fuel to be pushed through the devices.

5.2 Fabrication of Porous Catalytic Layer

A successful way to fabricate the porous catalytic layer was a key to this project. The catalyst is platinum or platinum/ruthenium at the anode and platinum at the cathode. The three key properties that must be obtained in the fabrication of the electrodes are porosity (access of the fuel to the membrane), conductivity, and catalytic activity. The

layer must contain enough Pt to be sufficiently catalytic as well as conductive to the electrons involved in the half reactions at both electrodes. However, there cannot be so much Pt that it loses its porosity and the reactants cannot come in contact with the membrane.

An initial attempt in making these catalytic layers was by spin coating fine particles of the catalyst. The diameters of particles contained in the fine metallic powders were approximately 1 μm. Metallic powder was mixed with polyimide to make a slurry and then spun onto wafers. Various ratios of powder to polymer, as well as diluting the polymer with its solvent, were tried. The results were not very good. Most of the coatings had streaks and had high electrical resistance. The micro particles had a tendency to clump together and were not distributed evenly on a micro scale basis.

A more successful approach was sputtering Pt or Pt/Ru. The amount of Pt sputtered is less than the minimum amount to form a contiguous blanket layer. This was necessary to keep the layer porous and conductive. An even thinner layer of titanium was co-sputtered with Pt or Pt/Ru layers to promote adhesion. Further details on sputtered catalyst films are given in more detail in chapter 6.

5.3 Microchannels with Polynorbornene

Polynorbornene (PNB) was used as the sacrificial polymer to make a number of microchannels on Si substrates. The fabrication of these microchannels, which included Al hard masks and reactive ion etching (RIE), is shown in Figure 5.1. Different polymers were tested as the overcoat materials. PI 2611, a polyimide from HD Microsystems, gave the best results. Figure 5.2 shows photographs taken through a microscope of the top view of air channels. A clean section of channels is shown in 2a, while an area of

blockage is shown in 5.2b. This blockage could either be PNB that did not fully decompose, or is from a collapse in the overcoat material. Figure 5.3 shows some pictures of an array of channels. The channels have a common inlet then branch out to have a greater fuel cell area.

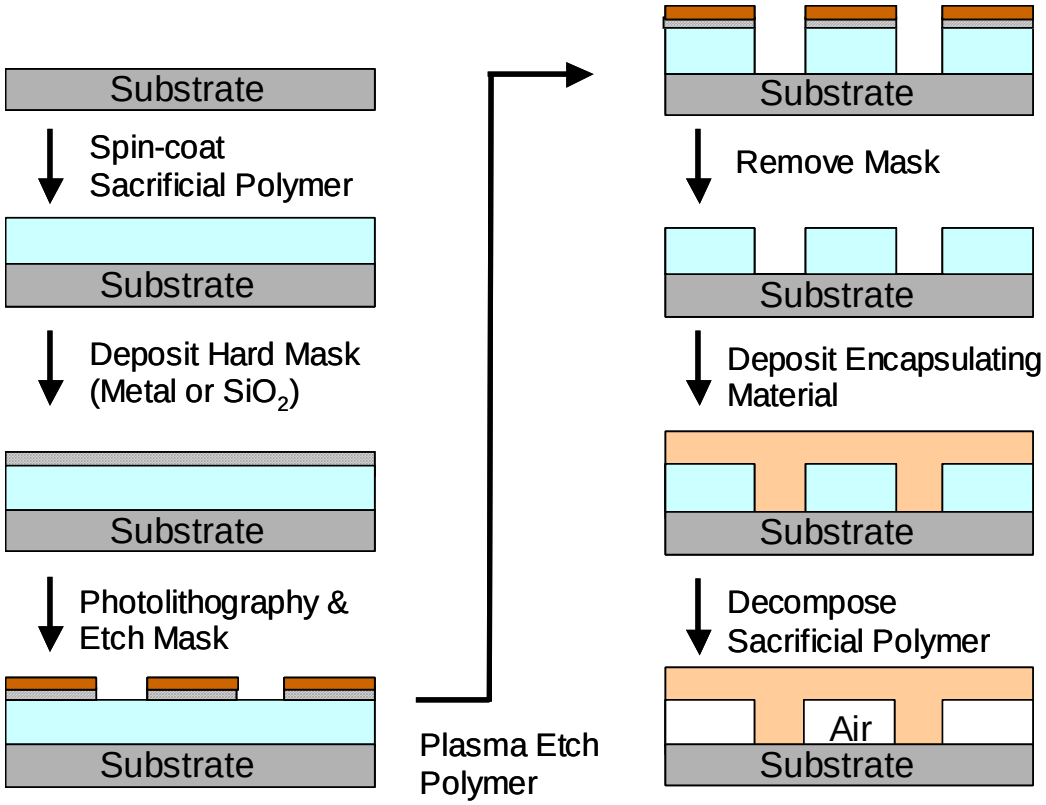

Figure 5.1: Microchannel formation process

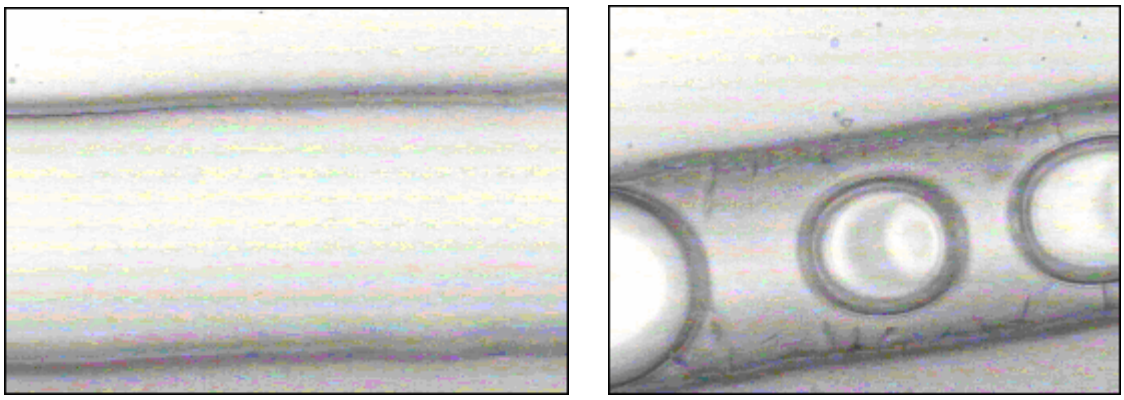

(a) (b)

Figure 5.2: Top-view pictures of microchannels

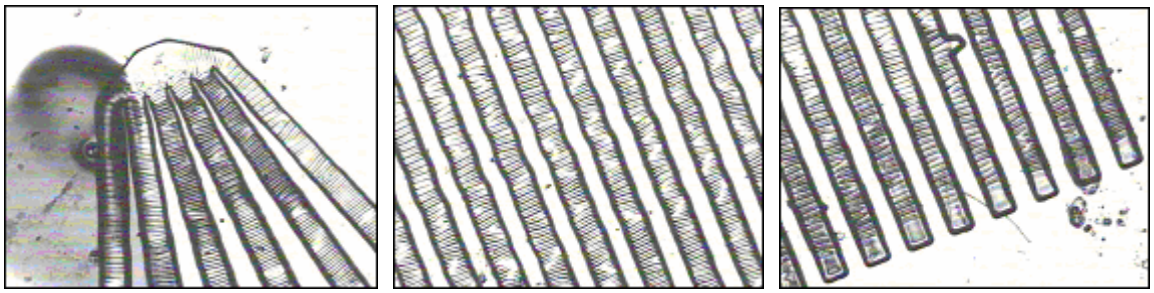

(a) (b) (c)

Figure 5.3: Top-view pictures of an array of parallel microchannels

5.4 Microchannels with Polycarbonates

One of the tasks in this project was the search for new sacrificial polymers with improved characteristics over PNB. The desired characteristics of the new sacrificial polymers included a lower decomposition temperature and photo-definability. PNB decomposes at 425°C. This was a higher temperature than many of the materials being studied as possible PEMs, which also serve as the microchannel overcoat, could withstand without a degradation of material properties. Therefore, a sacrificial polymer with a decomposition temperature of 200°C or less was desired. Along with a reduced decomposition temperature, the ability to pattern the sacrificial polymer through exposure to UV radiation, like a photoresist, would reduce the number of processing steps and possibly increase yield. A class of sacrificial polymers that were studied as a replacement to PNB was poly carbonate.

Two types of poly carbonate were examined, poly propylene carbonate (PPC) and poly cylcohexene carbonate (PCC). Both of these polymers have decomposition temperatures that are lower than PNB. A photo acid generator (PAG) was mixed with each of these materials to provide the possibility of direct patterning with UV exposure through a mask. Photo-patterning of the polymers was performed as well as the more traditional means of using a hard mask and reactive ion etching (RIE) of the polymer. Another challenge in processing that was studied was the compatibility of these sacrificial polymers and the overcoat materials, which would also serve as the PEM.

The steps taken to photo-pattern the polycarbonate, as shown in Figure 5.4, included spinning the polymer, UV exposure through a mask, and preliminary decomposition on a hot plate. The UV radiation caused the PAG to generate acid in the

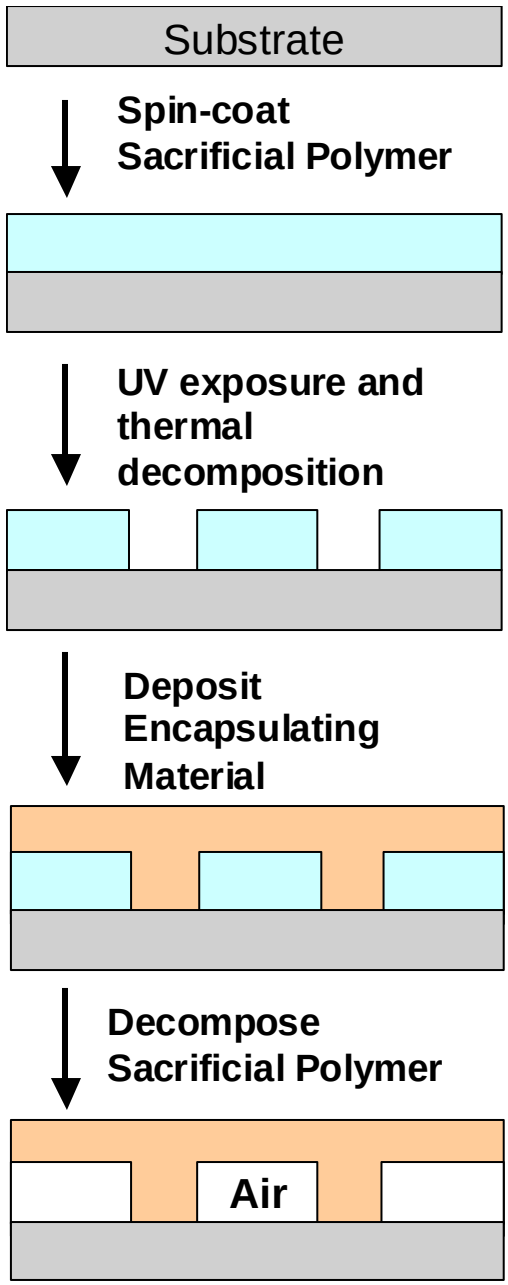

Figure 5.4: Microchannel formation process with a photo-definable sacrificial polymer

exposed areas. The acid reduces the temperature of the decomposition reaction. Therefore when substrate is heated to this lower decomposition temperature, the exposed polycarbonate decomposes into gaseous products. The unexposed polycarbonate remains. A short (30-60 seconds) descum in oxygen plasma was shown to remove any residue. Figure 5.5 shows a profilometer measurement of 100-μm lines and spaces photo-patterned in PCC. The final height of the features was about 6 μm.

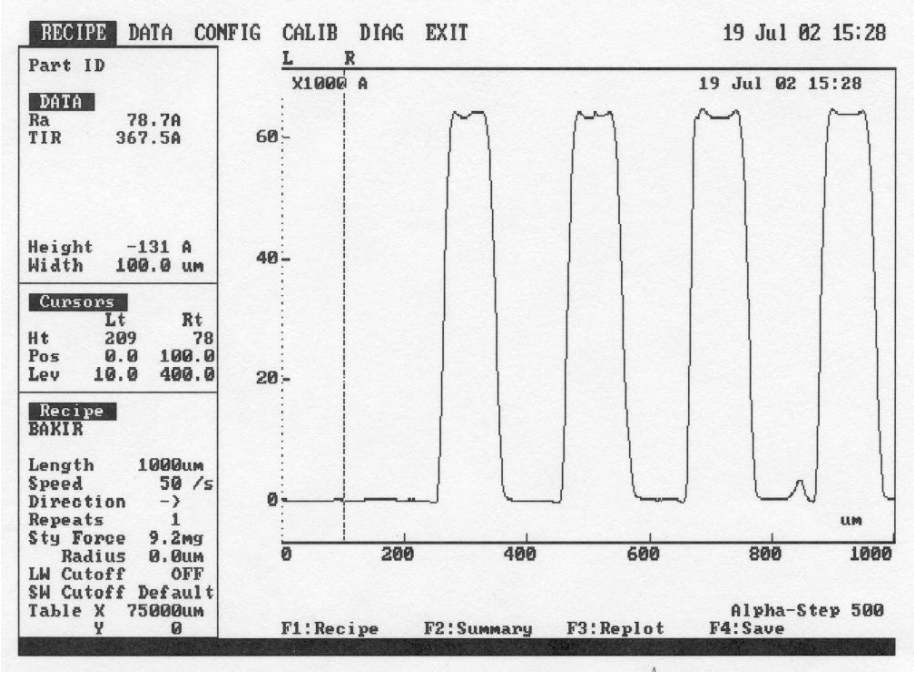

Figure 5.5: Profilometer measurement of photo-patterned PCC features

A number of materials were shown to work as an overcoat for PNB channels. Of these, the search was for one that would work with the poly carbonate and serve as a suitable PEM. Polyimide works well as an overcoat for PNB and was tried with both types of poly carbonate. The solvent that polyimide is cast in, NMP, quickly dissolved both PCC and PPC features during the spin-on process. Other polymers that were tried included polynorbornene-based polymers and PBO. Solvent compatibility problems were also encountered with these polymers. To overcome this obstacle, a thin layer of SiO_2 was deposited over the patterned PCC to serve as a barrier between the features and the overcoat's solvent. The SiO_2 also helps the mechanical stability of the overcoat during the PCC decomposition process decreasing the number of collapsed channels.

Because a number of the overcoat materials that are used for the higher temperature sacrificial material (polynorbornene) have solvent compatibility problems with PCC and PPC, a thin layer of SiO_2 was deposited over the patterned sacrificial material to serve as a barrier between the features and the overcoat's solvent. The SiO_2 also helps the mechanical stability of the overcoat during the PCC decomposition process decreasing the number of collapsed channels. To help serve as a baseline for PEM comparisons, it was decided to make the first prototypes with only SiO_2 as the overcoat. Figures 5.6 and 5.7 show microscope images of both ends of a completed device after the PCC was decomposed to form the microchannels.

Figure 5.8 shows a profilometer measurement of a patterned PPC feature. PPC can be spin-coated up to 25 μm thick. Therefore, it was used to create larger microchannels. It can also be seen that the slope of the sidewalls of the photo-patterned

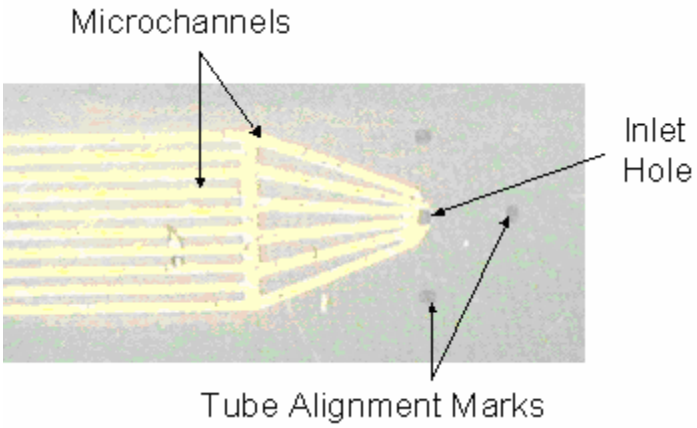

Figure 5.6: Fuel inlet area of micro fuel cell

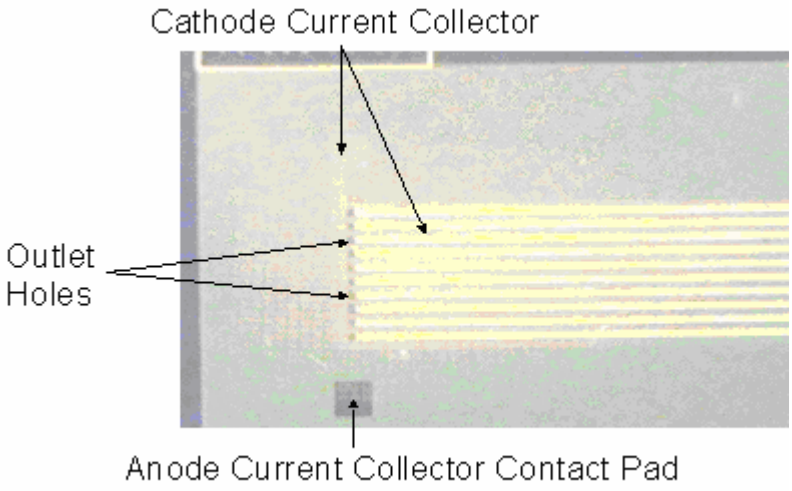

Figure 5.7: Fuel outlet area of micro fuel cell

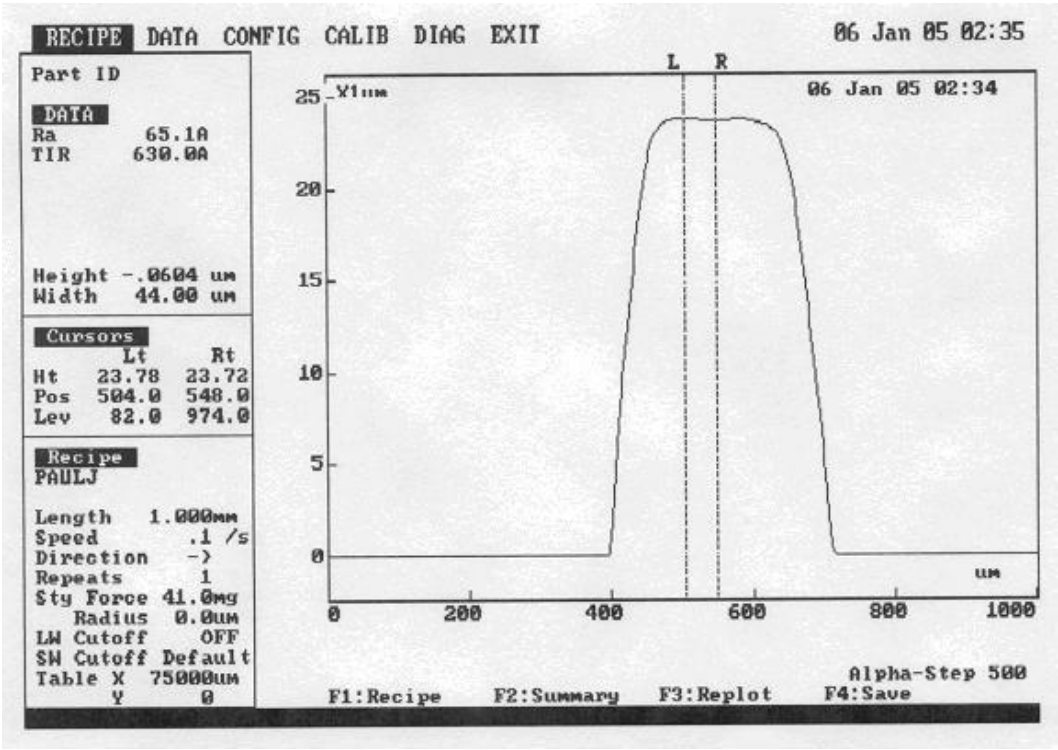

Figure 5.8: Profilometer of a PPC feature made through photo-patterning

PPC had a lower angle than for PCC or the RIE-patterned PNB. This was determined to be advantageous for the fuel cell design due to it allowing better coverage of the sputtered catalyst on the sidewalls. It was also noticed that the height of the patterned PPC features were dependent on their width, that is to say, the wider the feature, the taller the final height. For this reason, simpler masks were used rather than the branching network of channels shown in Figures 5.6 and 5.7 in favor of a single, 300-μm wide, 1.5-cm long fuel channel. After thermal patterning of the features, isopropyl alcohol was used to rinse off residue from the PPC decomposition. This was followed by a short exposure to an oxygen-based plasma in a Plasma-Therm reactive ion etching (RIE) system to further clean the surface. The oxygen plasma also served to roughen the surface of the PPC features. The final height of the PPC channels in this work was typically between 18 and 20 μm.

5.5 Conclusions

The use of sacrificial polymers to form microchannel structures was successfully accomplished. Photo-definable PPC with a relatively high viscosity was used in the fabrication of the micro fuel cell devices due to its low decomposition temperature, reduced processing time, and ability to form relatively large microchannels. Channels were typically 300 μm in width, 20-25 μm in height, and 1.5 cm in length. The fabrication of the cells followed the processing scheme described, including the deposition of catalyst, current collectors, and membranes. The requirements for a suitable overcoat material were numerous due to the fact that it would also serve as the proton exchange membrane for the fuel cell. Low-temperature deposited PECVD silicon

dioxide was often used as the PEM or with different polymers in dual-layer PEMs. Phosphorous doping of the SiO_2 films was also examined. The study of the electrodes and PEMs, particularly in use with the microchannels, is the focus of following chapters.

CHAPTER 6

SPUTTERED CATALYST ELECTRODES

6.1 Introduction

An important topic to investigate in microfabricated fuel cells is decreased catalyst loading. Hydrogen-based proton exchange membrane (PEM) fuel cells typically use platinum as the catalyst for the oxidation of hydrogen and the reduction of oxygen at the cathode. For direct methanol fuel cells (DMFC) Pt-Ru alloy catalysts are the most efficient anode catalysts for methanol electro-oxidation (37-39). The addition of Ru to the Pt catalyst enhances the rate of methanol electro-oxidation because the Ru provides a site for water oxidation and OH adsorption needed in oxidation of methanol to CO_2. The availability of adsorbed OH on the Ru lowers the number of CO intermediates on the Pt (40-43). In a typical DMFC, the anode catalysts are generally present in the form of nanoparticles supported on high surface area carbon in contact with the membrane (40, 44-46). Sputtering the metal catalyst allows for very low catalyst loading because of the size of the deposited particles in the island growth stage of film deposition. The advantages to sputtering the catalyst include the lower Pt loading (48) because of the higher surface area to weight ratio and a reduction in methanol crossover due to better coverage (26). Depositing a single layer of catalyst onto the membrane limits the amount of catalyst that can be deposited, because the film must remain porous to allow reactants to contact the membrane. The anode reaction must occur at the interface between the catalyst and electrolyte membrane for the protons to be transported to the cathode, where they subsequently are consumed in the cathode reaction where the membrane and catalyst are in contact. A fabrication technique that can increase the amount of sputtered catalyst

while maintaining porosity for reactant access to the membrane can be an important factor in improving cell performance.

Figure 6.1 shows a schematic diagram of the cross section of the microfabricated fuel cells using a sacrificial polymer to form fuel delivery microchannels. The processing requires a layer-by-layer sequential build-up. Therefore, the anode catalyst is deposited on the sacrificial polymer, and then coated with the PEM material. The cathode catalyst must then be deposited directly onto the membrane.

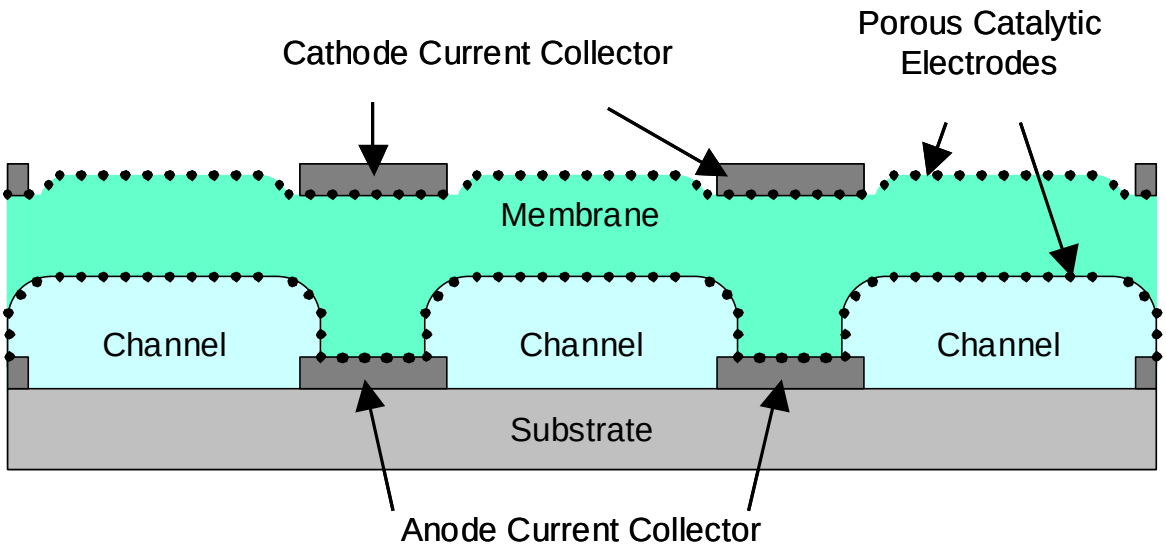

Figure 6.1: Schematic cross-section of microchannel fuel cell

6.2 Experimental Method

Catalyst layers were sputter deposited using a CVC DC sputterer (CVC Products, Inc., Rochester, NY). A platinum target and a 50:50 atomic ratio platinum/ruthenium target (Williams Thin-Film Products, Brewster, NY) were used as the source targets. Figure 6.2 shows an X-ray photoelectron spectroscopy (XPS) scan confirming that the sputtered Pt/Ru films have equal amounts of the two metals. Porous films with average thicknesses of 50-200 Å were deposited on the sacrificial polymer, and then coated with the membrane, to serve as anode catalysts.

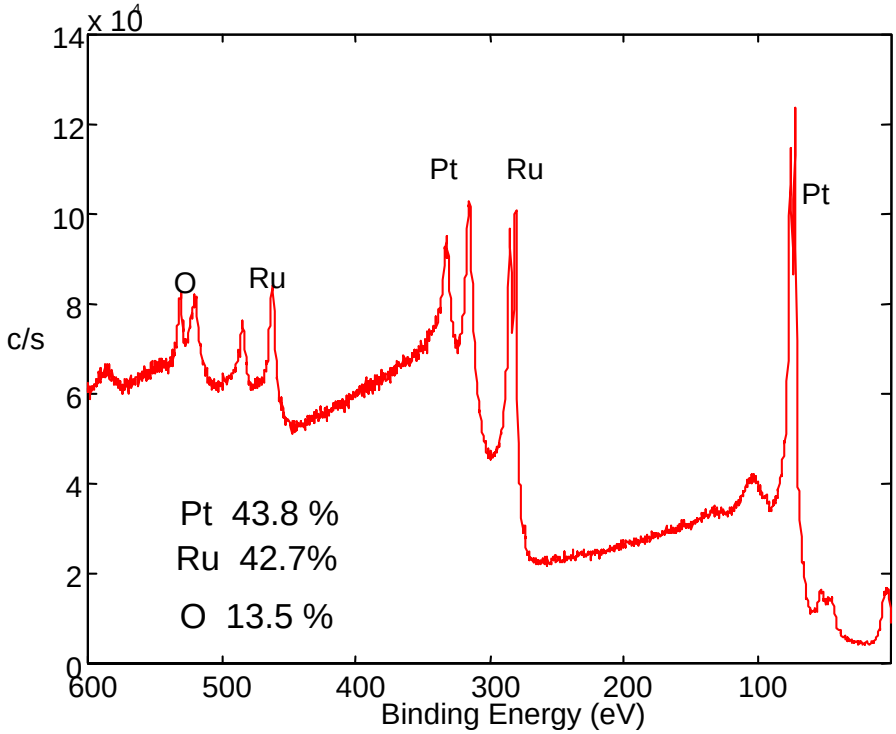

Figure 6.2: XPS scan of sputtered Pt/Ru

Porous catalytic cathodes were also fabricated by sputtering Pt or Pt/Ru on the top, or outside, of the PEM. However, the cathodes on the samples discussed here were made by painting a prepared catalyst ink containing carbon-supported Pt in Nafion on the PEM, followed by coating with a porous gold current collector. This thick-film approach increased the catalyst loading and performance on the cathode side of the PEM. This was especially useful in studying the anode performance by eliminating the oxygen reduction at the cathode from being the rate-limiting step.

In addition to catalytic activity, the key properties that were desired for the sputtered catalyst layers were porosity and electrical conductivity. The catalyst layer that contacts the membrane must be porous so that the protons generated during oxidation can come in contact with the PEM and pass to the cathode. The electrons generated at the anode catalyst need a path to the metal current collectors. To determine a range of catalyst loading that would provide these requirements, different amounts of Pt were sputtered onto substrates containing two solid electrodes patterned on opposite sides of an insulator. The sheet resistance of the Pt layers across the space between the electrodes was measured. Three sets of samples were made with different layers for the Pt to be sputtered on: a smooth oxide, a layer of the polypropylene carbonate (PPC) sacrificial polymer, and a layer of PPC that was exposed to 3 minutes of oxygen plasma in a Plasma-Therm reactive ion etcher (RIE) system (Plasma-Therm, St. Petersburg, FL). This oxygen plasma step is a necessary step following the photo-patterning of the PPC for microchannels. It also serves to roughen the polymer, which should lead to an increase in the amount of metal needed to form a complete layer free of any holes.

Pt/Ru was also found to cause problems with adhesion in the processing of the fuel cells. When it was sputtered and then overcoated with SiO_2, the oxide layer delaminated from the surface, usually upon contact with water or solvent, in the areas with catalyst. For this reason an adhesion layer of titanium was always used in conjunction with the Pt/Ru depositions, except for embedded catalyst layers. The layer of Pt/Ru deposited prior to the PPC was sputtered onto a sputtered Ti layer. After the PPC had been spin-coated and photo-patterned, the sputtering of the porous catalyst layer included the Pt/Ru followed by 45 Å of Ti. As with the catalyst depositions, the 45 Å of Ti was an average thickness for a discontinuous film deposition, but did prove to be enough to promote SiO_2 adhesion to the surface. The only material that Pt/Ru was in direct contact with was the PPC prior to decomposition, leaving it exposed for fuel contact in the microchannels. In the areas where PPC was removed, the top catalyst was sputtered on the first Pt/Ru layer, so Ti was both above and below the Pt/Ru, improving the SiO_2 adhesion to the surface.

6.3 Results and Discussion

Figure 6.3 shows the measured resistance (Ω/square) of sputtered Pt films on the three types of samples as a function of thickness for layers with average thicknesses between 30 and 600 Å. Figure 6.4 shows a closer view of the data for average thicknesses between 45 and 150 Å. Also plotted are calculated values of sheet resistance for smooth, continuous films of the indicated thickness. Above 150 Å, the measured values correspond to the expected values, indicating that the films were contiguous. Below 150 Å the resistance increased more dramatically with decreasing thickness. For

the samples with 60, 75, 90, and 105 Å, the resistance is higher than the calculated values, up to twice as much, indicating some discontinuity or porosity in the film, but that electrical pathways are still present. For the samples with less than 60 Å, the resistance is dramatically more than the calculated values, indicating that the sputtered Pt islands have are too small or too few in number to provide enough electrical conductance between the electrodes.

The desired electrodes were fabricated to be in the middle region of porous, yet somewhat continuous catalyst films. These results did not show that roughening of the Unity sacrificial polymer's surface through RIE dramatically increased in the amount of metal that could be sputtered before making a metal layer with electrical conductivity. In this work, Pt and Pt/Ru layers with average thicknesses of 50-200 Å were used as porous, conducting layers on photo-patterned Unity features that were roughened through the oxygen plasma de-scum.

Half-cell devices were fabricated and tested to evaluate the anode performance with different fuels and provide a comparison for the full cell tests. A solid layer of Pt/Ru was deposited before the sacrificial polymer was patterned, as well as a porous layer on top of the patterned features to be in contact with the membrane. The catalyst weight at the membrane surface was 17 $\mu g/cm^2$. Hydrogen was supplied with a pressurized tank of ultra high purity grade gas that passed through a bubbler to humidify the feed. Figure 6.5 shows the results for inlet pressures of 1-4 psig (15.7-18.7 psia). The current densities of the half-cells scale with the partial pressure of the humidified hydrogen. This indicates that the performance is chiefly limited by the catalytic reaction

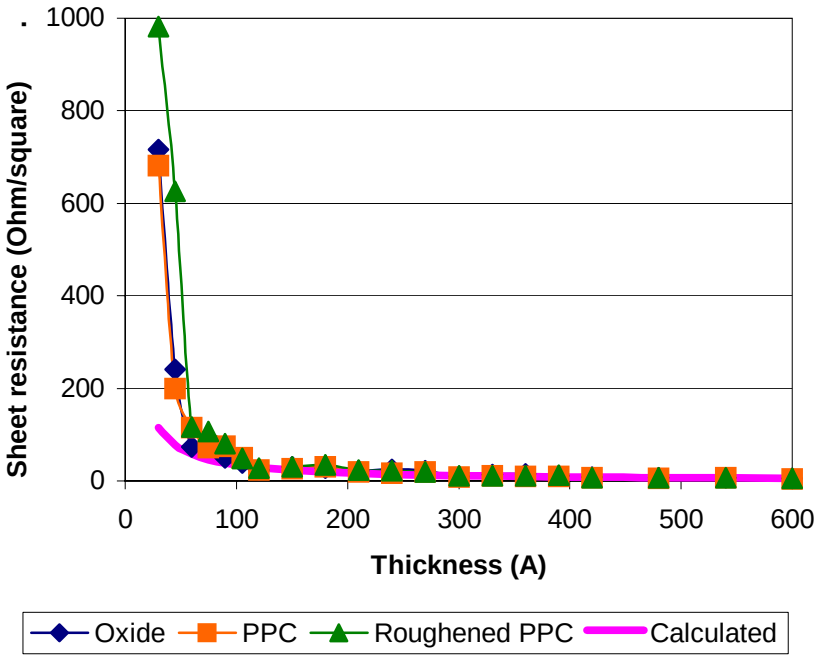

Figure 6.3: Measured and calculated resistances for sputtered platinum films

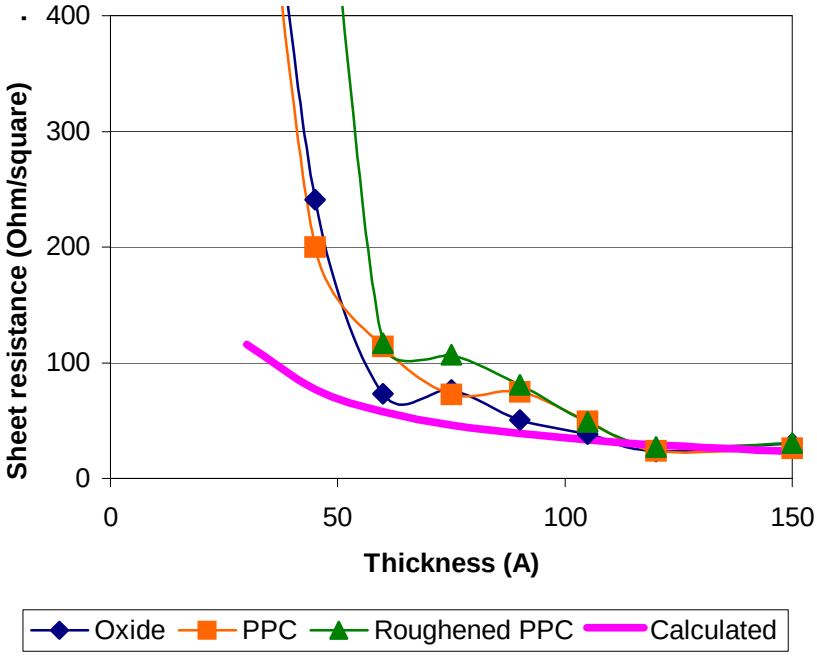

Figure 6.4: Measured and calculated resistances for sputtered platinum films

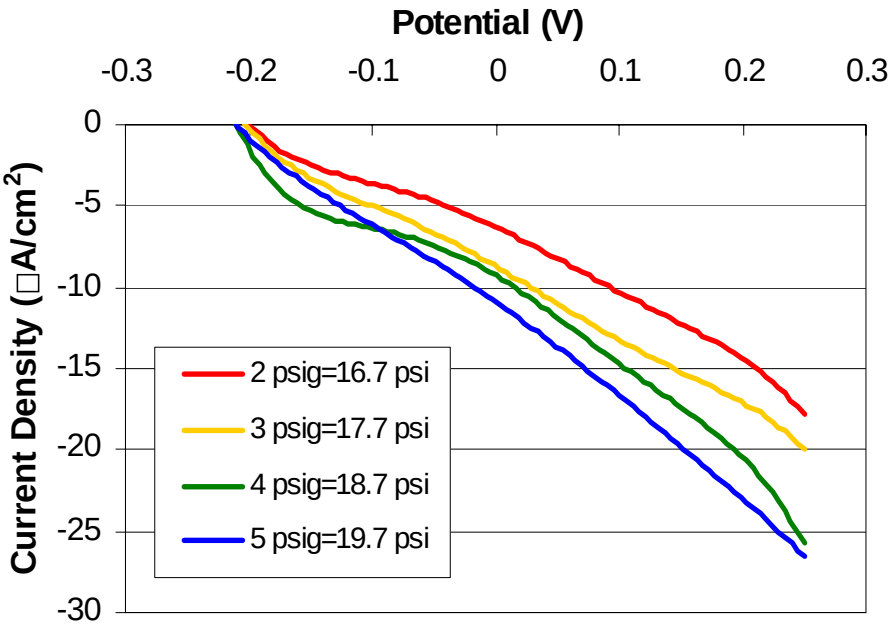

Figure 6.5: Half-cell performance of microchannels with humidified hydrogen

kinetics at the anode, that is, proportional to hydrogen partial pressure. Further improvements in current density are possible with improved activity of the anode catalyst.

Microfabricated full-cells were fabricated and tested with linear voltammetry at a scan rate of 1 mV/sec from the open-circuit potential. Table 6.1 compares the differences in process between five sets of cells that are presented here to demonstrate the key parameters (anode and cathode construction) that affect cell performance for these power devices.

Table 6.1: Processing characteristics of micro fuel cell samples

Sample	Anode catalyst weight* ($\mu g/cm^2$)	SiO_2 membrane thickness (μm)	Cathode catalyst
A	31	3.2	sputtered
B	17	3.2	thick-film
C	34	3.2	thick-film
D	43**	3.2	thick-film
E	17	2.4	thick-film

* Weight at membrane surface (100 $\mu g/cm^2$ at bottom of microchannels)
** Total weight of two Pt/Ru layers with 400 Å SiO_2 deposited between

Figure 6.6 shows polarization (top) and power (bottom) curves for one cell, sample A, that had sputtered catalyst with a loading of 31 $\mu g/cm^2$ at both the anode and cathode. Humidified hydrogen with an inlet pressure of 1 psig served as the fuel and oxygen from the air was reduced at the cathode. The performance at 60°C was approximately four times greater than at ambient conditions with a measured peak power density of 4 $\mu W/cm^2$. The lower current densities of these devices with sputtered catalyst on the cathodes compared to the results from the anode half-cells run with hydrogen shown in Figure 6.5 demonstrate that their performance is limited by the catalytic activity of the air cathode. This agrees with the expectation that ambient oxygen reduction at the cathode would be performance limiting when pressurized hydrogen was used at the anode.

A thick-film ink catalyst was coated onto the air-breathing cathode to improve its area and catalyst activity. When using the painted catalyst ink on top of the membrane, the full cell performance increased dramatically due to the increase in cathode catalyst loading. Because of the significant improvement to the oxygen reduction at the cathode, it was no longer the limiting electrode. The performance of cells with the thick-film cathode was a function of the anode composition. Figure 6.7 shows the polarization (top) and power (bottom) curves at ambient temperature, 40°C, and 60°C for sample B. This sample had an anode and membrane similar to sample A, but used the catalyst ink and porous gold current collector for the cathode. Hydrogen with an inlet pressure of 1 psig was the fuel and the cathode was air-breathing. The room-temperature polarization curve shows current densities very similar to the hydrogen half-cell results from Figure 6.5.

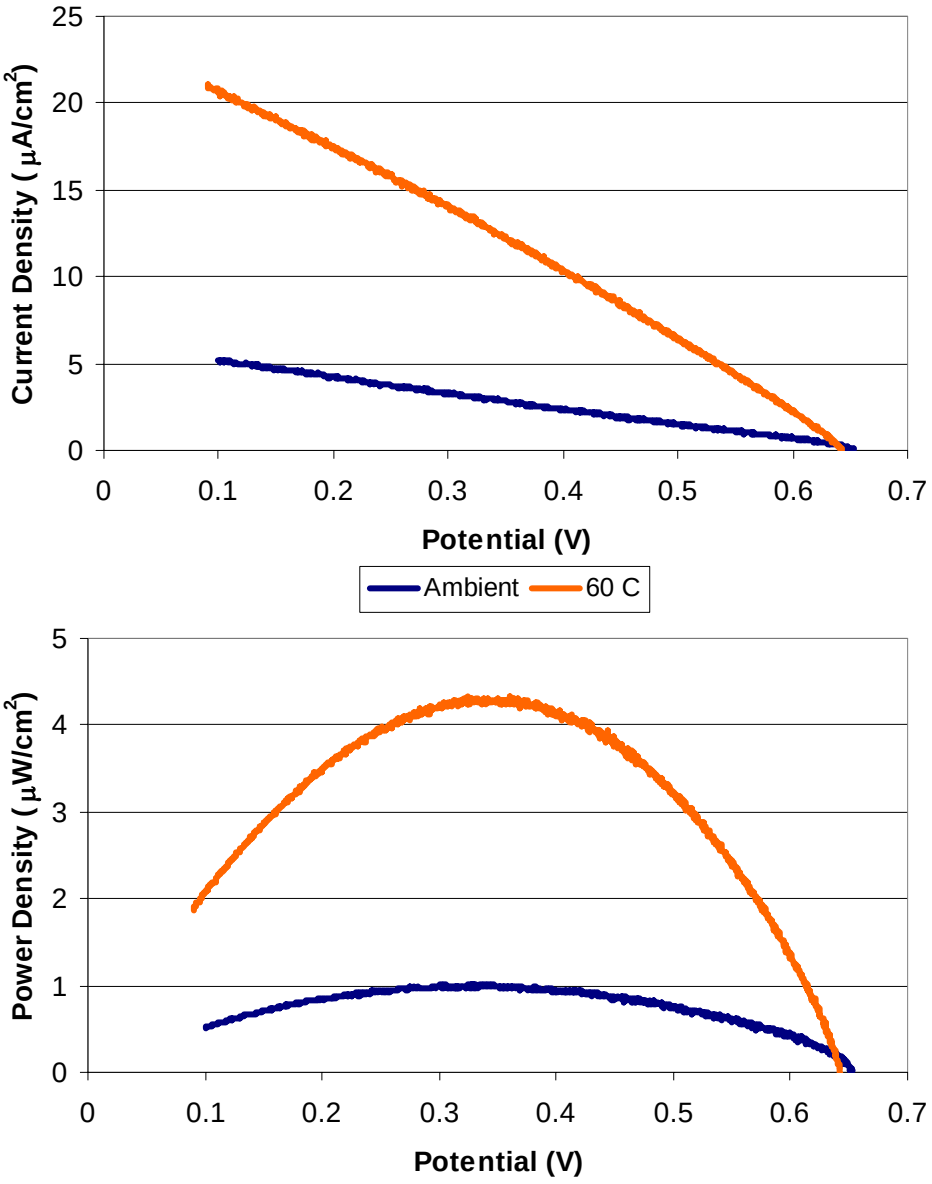

Figure 6.6: Micro fuel cell performance with sputtered anode and cathode

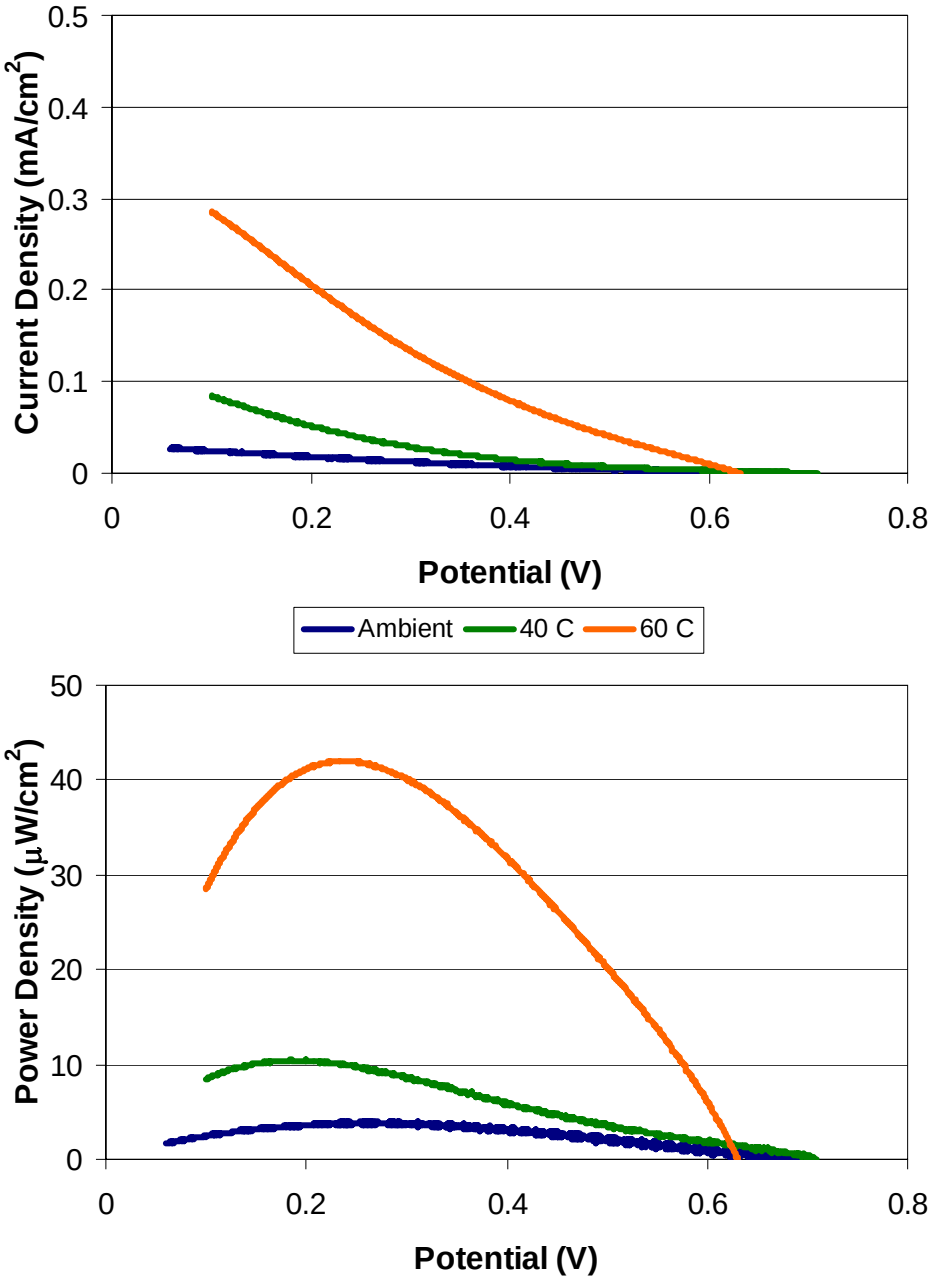

Figure 6.7: Micro fuel cell performance with sputtered anode and thick-film cathode as a function of operating temperature

The performance was approximately one order of magnitude greater than sample A with a peak power density of 42 $\mu W/cm^2$ at 0.23 V and 60°C. These two results indicate that the anode limits the sample's performance when using the painted catalyst instead of the sputtered catalyst at the cathode.

The temperature dependence was such that greater power output could be achieved at elevated temperatures. Waste heat is produced in fuel cells, however, the size of these devices and the amount of power generated suggest that they would not be able to retain enough heat for operation at an elevated temperature. Integrated fuel cells could also use some heat released from the circuit (or other electronic devices) that they are built on.

Improvements in the activity and surface area of the anode can lead to higher currents and power densities. The anode performance was improved with a higher catalyst loading. Figure 6.8 shows the room temperature polarization (top) and power (bottom) curves of three samples with different amounts of sputtered catalyst at the anode. Humidified hydrogen with an inlet pressure of 1 psig was the fuel and the thick-film cathodes were air-breathing. A solid layer of approximately 100 $\mu g/cm^2$ of Pt/Ru was deposited on the bottom of the microchannels on each sample. At the membrane surface, sample B had 17 $\mu g/cm^2$ of Pt/Ru and sample C had 34 $\mu g/cm^2$. With twice as much sputtered Pt/Ru at the membrane, sample C shows an improvement in performance of less than 50% over sample B. Sputtering twice as much Pt/Ru does not double the catalyst surface area because the deposited islands are getting bigger, forming a more continuous (less porous) film.

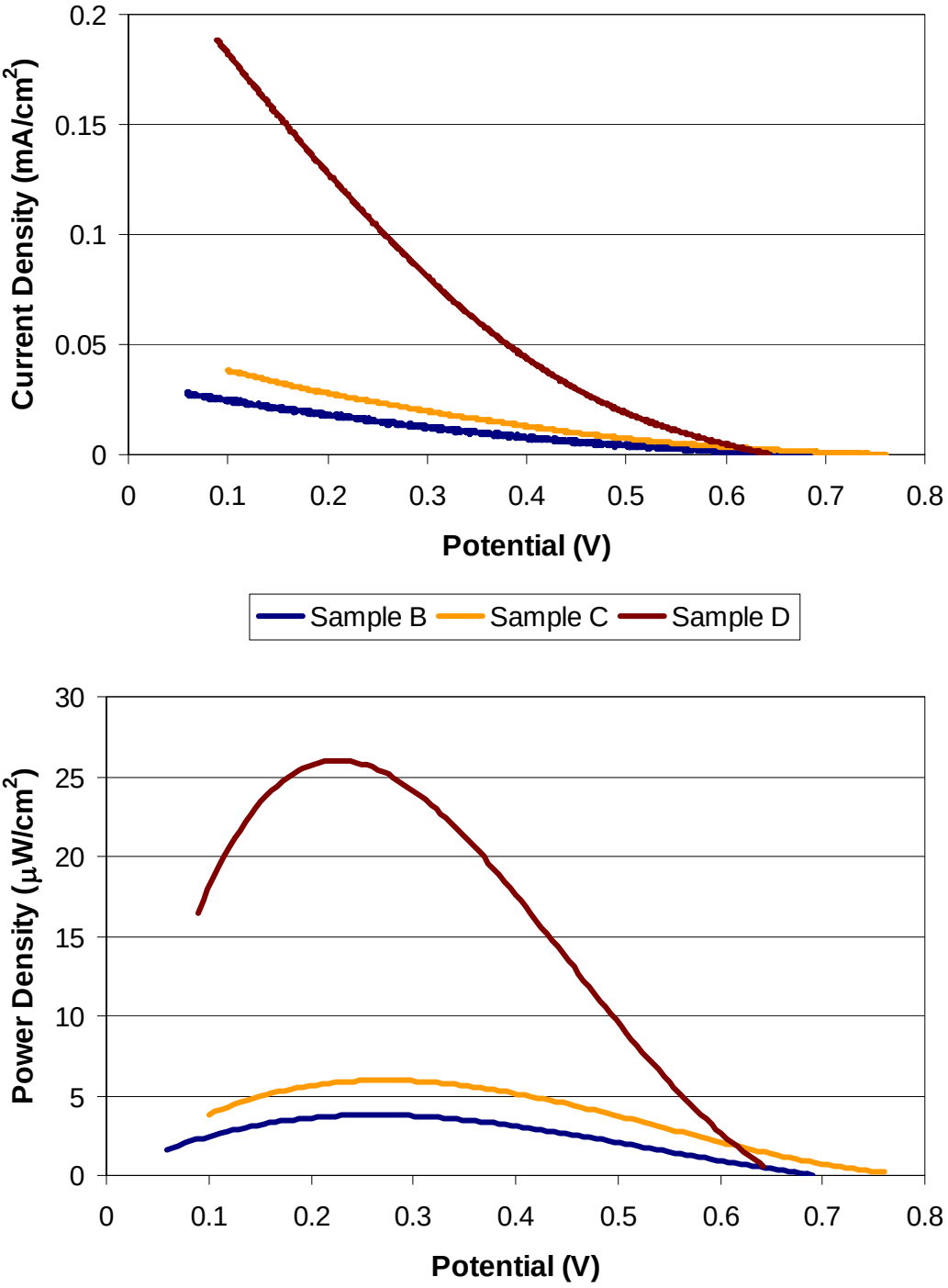

Figure 6.8: Ambient temperature micro fuel cell performance for samples B, C, and D with different amounts of sputtered anode catalyst

To improve the electrode performance, the catalyst surface area, particularly the catalyst that is in direct contact with the electrolyte, must be increased. A thin layer of SiO_2 electrolyte could be deposited between two catalyst depositions because it was deposited through PECVD. Sample D had the same 34 $\mu g/cm^2$ layer as C deposited on the patterned sacrificial polymer, followed by a deposition of 400 Å of SiO_2, and then an additional 8.5 $\mu g/cm^2$ of catalyst, before the thicker SiO_2 PEM layer was deposited. The second layer of sputtered Pt/Ru was imbedded in SiO_2, increasing the catalyst/electrolyte contact area. With only 25% more Pt/Ru at the membrane, the peak power density of sample D was over four times greater than sample C at room temperature. This dramatic improvement in current and power density was due to the SiO_2-encapsulated layer of Pt/Ru that allowed for more membrane/catalyst contact in addition to the increase in total catalyst weight. The two thin layers of Pt/Ru and the small amount of SiO_2 between them most likely form a mixed matrix of catalyst and electrolyte that is conductive to both protons and electrons while increasing the overall catalyst surface area, particularly the area in contact with the electrolyte.

The performance of the hydrogen fuel cells was studied as a function of time to determine if the data collected through linear voltammetry matches steady-state values at constant potential. Figure 6.9 shows the current density of sample D when a constant potential is held for ten minutes. The data show a relatively constant performance that is very close to the values collected for a linear sweep of 1 mV/s, as shown in Figure 6.10. Tests over longer periods of time, such as a few hours, with different devices have shown similar results. The SiO_2 did not swell with water like Nafion films, making them less susceptible to changes with time, such as a drop in performance from drying out.

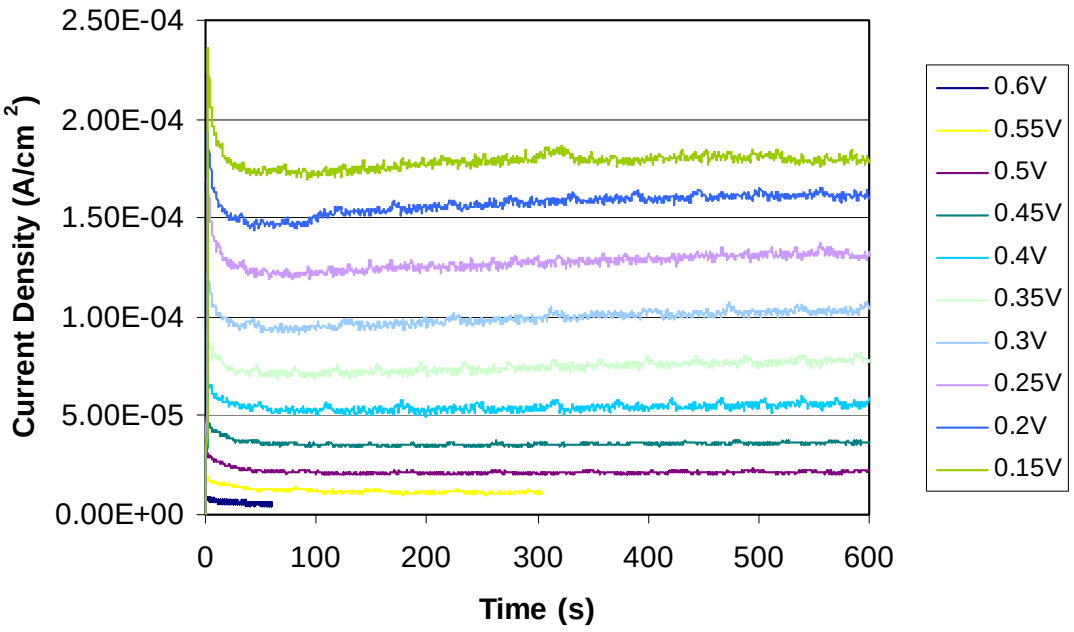

Figure 6.9: Current density of the imbedded catalyst sample held at constant potential for 10 minutes

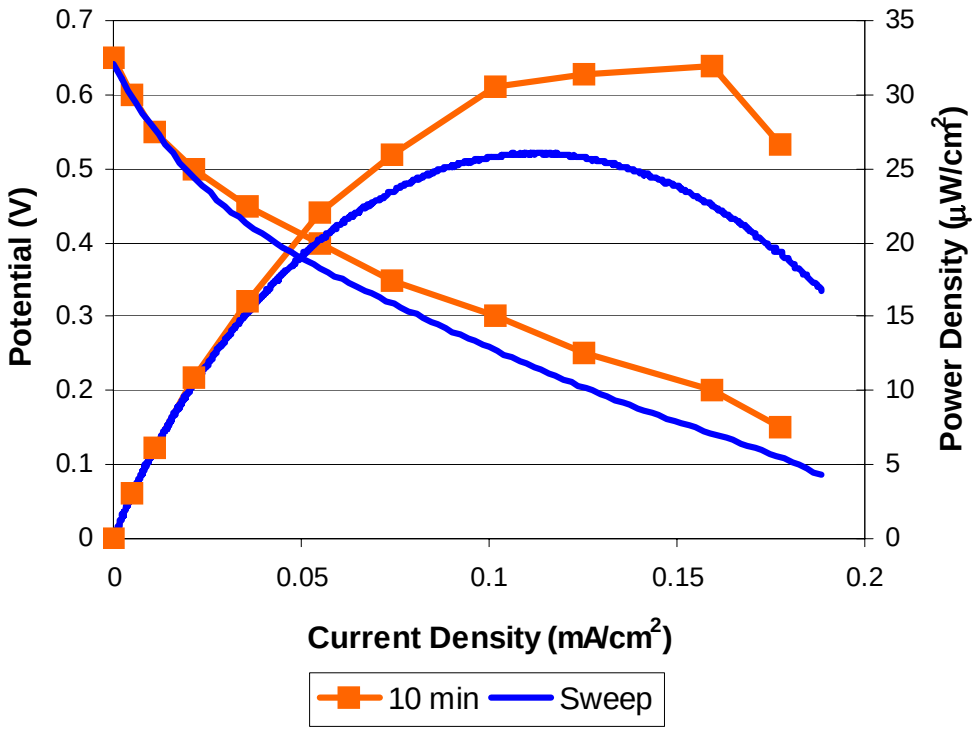

Figure 6.10: Comparison between steady-state (at 10 minutes) and linear voltametry polarization data for sample D with humidified hydrogen at room temperature

Experiments were performed to determine if any residue from the decomposition of PPC remained at the catalyst surface and hindered performance. Samples were prepared by sputtering a solid layer of Pt/Ru onto the substrate and then coating with PPC. It was not patterned or over coated with another material prior to decomposition. It was decomposed in a tube furnace following the standard recipe for temperatures and times. Afterwards, a noticeable, black residue remained on the surface. The catalytic activity of the Pt/Ru underneath was tested and compared to a fresh layer of Pt/Ru. Figure 6.11 shows the oxidation of methanol at these surfaces. Also shown are the results for Pt/Ru covered with PPC residue after being treated with a mixture of sulfuric acid and hydrogen peroxide. The activity improved, but was still significantly less than the clean catalyst. Other solvents were used in an attempt to remove the residue, but none of them were better than the sulfuric acid and hydrogen peroxide.

In addition to the first layer of catalyst having a residue remain from the decomposed PPC, another cause for the dramatic increase in performance from the second layer is the increase in catalyst/electrolyte contact area. Figure 6.12 shows a schematic representation of the catalyst particles at the membrane surface. The light gray Pt/Ru particles on the surface do not have as much contact with the electrolyte, shown in blue, as the second layer of embedded particles. Shown in darker gray, the titanium deposited for adhesion further reduces the contact between catalyst and electrolyte.

Finally, one may suspect that catalyst falling off the membrane surface would be possible cause of the lower performance of the first layer of catalyst, but the results indicate otherwise. First, the performance remains relatively constant over time, indicating that fuel passing down the channel is not removing it. If, on the other hand,

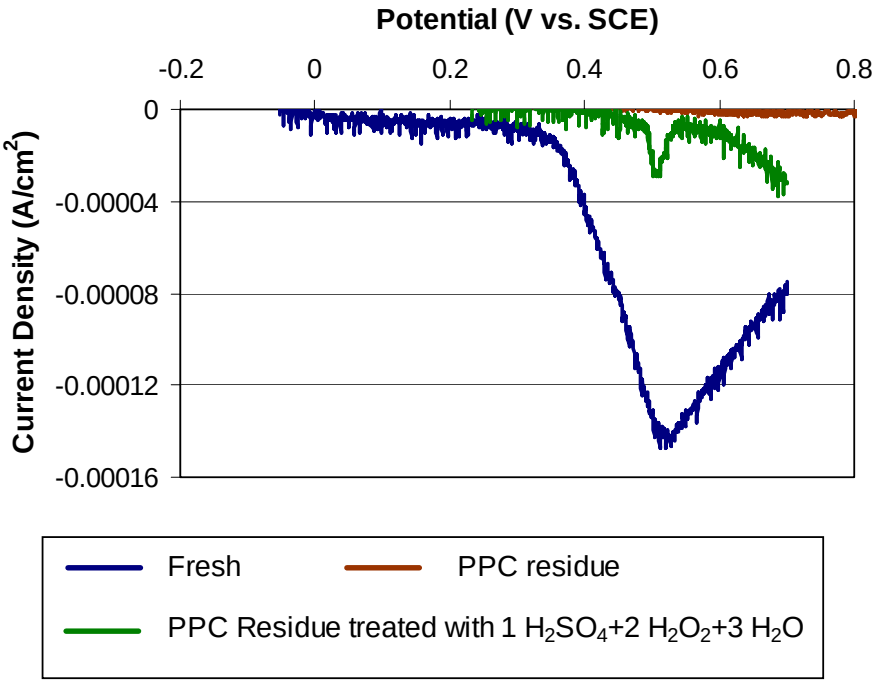

Figure 6.11: Catalytic activity of Pt/Ru films with PPC residue

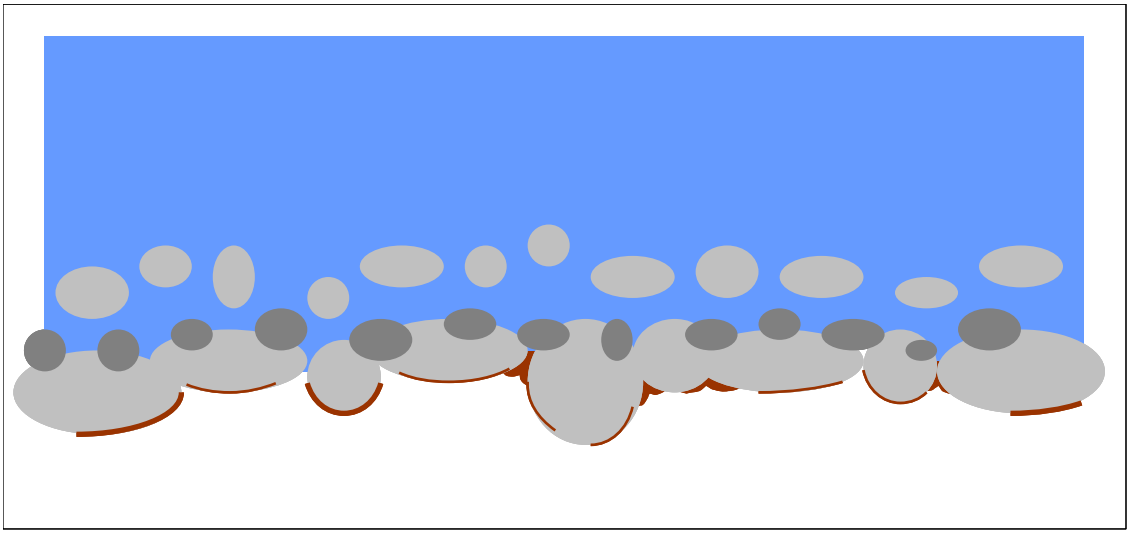

Figure 6.12: Schematic representation of the catalyst/membrane surface

the Pt/Ru falls off the membrane during PPC decomposition or shortly thereafter, then the performance would be dependant upon the amount of Pt/Ru that remains because of the titanium adhesion layer. This scenario would lead to the performance scaling with the amount of sputtered Ti, because it would determine how much of the catalyst remained on the membrane surface. The results, however, show that the performance increases with additional Pt/Ru, though the same amount of Ti was sputtered.

6.4 Conclusions

The performance was chiefly limited by the amount of catalyst used. While the current density was acceptable for the catalyst loading being used, increasing the catalyst in the electrode layers, but still maintaining the porosity of the sputtered layers for proton transport, was the key to increased performance. The two main factors for reduced performance from the sputtered catalyst layers are residue from the decomposed sacrificial polymer and limited contact area between the catalyst and electrolyte. Repeated alternate catalyst sputtering and SiO_2 deposition steps to build up a catalyst matrix provides an electrode with increased catalyst and membrane-catalyst contact area.

CHAPTER 7

ACIDIC METHANOL FUEL

Acidic methanol solutions have been investigated for use in direct methanol microchannel fuel cells. The increased proton conductivity of a methanol solution containing sulfuric acid enables the anode to be constructed with the catalyst separated from the proton exchange membrane. This approach could be especially useful in the fabrication of thin-film microchannel fuel cells where a more complex carbon fabric electrode is not possible. The performance of sequential build-up fuel cells was shown to be improved by depositing an additional layer of Pt/Ru on the side-walls of the anode microchannels opposite the membrane. Results from anode half-cell and full cell experiments are reported.

7.1 Introduction

Low temperature direct methanol fuel cells (DMFCs) convert liquid methanol and water into electrical energy and are a promising technology for portable devices. Compared with other fuel cell systems, the liquid-feed DMFC is relatively simple and could be easily miniaturized since it does not need a fuel reformer, complicated humidification, or thermal management system (50-52). Furthermore, methanol has a high energy density in comparison with lithium polymer and lithium ion polymer batteries (53). The main challenges associated with the development of DMFCs include poor electro-oxidation kinetics of methanol, high methanol crossover through the proton exchange membrane (PEM), carbon dioxide removal from the anode, and high overpotentials at the air cathode (54-58). To date, Pt-Ru alloy catalysts are still the most

efficient anode catalysts for methanol electro-oxidation (38-39, 59). The addition of Ru to the Pt catalyst enhances the rate of methanol electro-oxidation because the Ru provides a site for water oxidation and OH adsorption needed in oxidation of methanol to CO_2. The availability of adsorbed OH on the Ru lowers the number of CO intermediates on the Pt (40-43). In a typical DMFC, the anode catalysts are generally present in the form of nanoparticles supported on high surface area carbon in contact with the membrane (40, 44-46).

Due to the thin-film, sequential build-up process of the microfabricated fuel cells, the anode Pt-Ru alloy catalysts must be directly deposited (e.g. sputtering or evaporation) on a relatively flat surface. Hence, the anode catalyst is composed of a relatively porous, smooth layer directly on the membrane as compared to Pt-Ru nanoparticles on high surface area carbon supports in the typical DMFC and has a much lower surface area than the carbon supported fuel cell anode (60). In the microfabricated cell, the catalyst layer itself serves as part of the current collector as shown in Figure 7.1(a) and provides in-plane conductivity for electron transfer as well as proton transfer to the membrane. The porosity of the catalyst layer on the membrane is a key issue for proton generation and transport to the membrane. A denser anode catalyst layer (lower porosity) has improved electrical conductivity at the expense of proton conductivity. Thus, an optimum anode catalyst loading is necessary to maintain low current collector electrical resistance and provide high catalytic activity.

In this work, a conductive analyte was used so that the surface area of the anode catalyst layer could be increased without having to decrease the porosity of the catalyst layer on the membrane or change the membrane-electrode configuration, as shown in

Figure 7.1(b). Although the anode catalyst extends to regions not in contact with the membrane, an acidic methanol solution could provide sufficient conductivity for proton transfer to the membrane. The electro-oxidation of acidic methanol on the sputtered Pt-Ru alloy was investigated. A fuel cell using an acidic methanol solution as the fuel and proton transport medium was fabricated to examine the contribution of Pt-Ru catalyst lining the anode chamber to the overall anode reaction. The power density of the fuel cell and the ability of the acidic methanol solution to transfer the protons are reported.

7.2 Experimental Method

The electrochemical experiments were performed using a PerkinElmer PARSTAT 2263. The scan rate for linear sweep voltammetry was 1 mV/s. The electro-oxidation of methanol in the acidic solution was studied in a three electrode system. The working electrode was a solid Pt-Ru alloy layer deposited on titanium by sputter-deposition at room temperature. The deposition rate was 3.0 Å/sec. and the deposition time was 6 min. The atomic ratio of the Pt-Ru alloy layer was 1:1, as confirmed by XPS analysis. The counter electrode was a platinum wire, and the reference electrode was a saturated calomel electrode (SCE). Deionized water and H_2SO_4 were used to prepare the acidic methanol solutions. The conductivity of the solutions was measured using impedance spectroscopy. The frequency range for the impedance measurement was from 100 mHz to 1 MHz, with an ac signal amplitude of 10 mV. During each test, the acidic methanol solution was purged with nitrogen gas.

The structure of the cell with the acidic methanol solution as the fuel and proton transport medium is shown in Figure 7.2. The anode was a Pt-Ru alloy layer with 1080

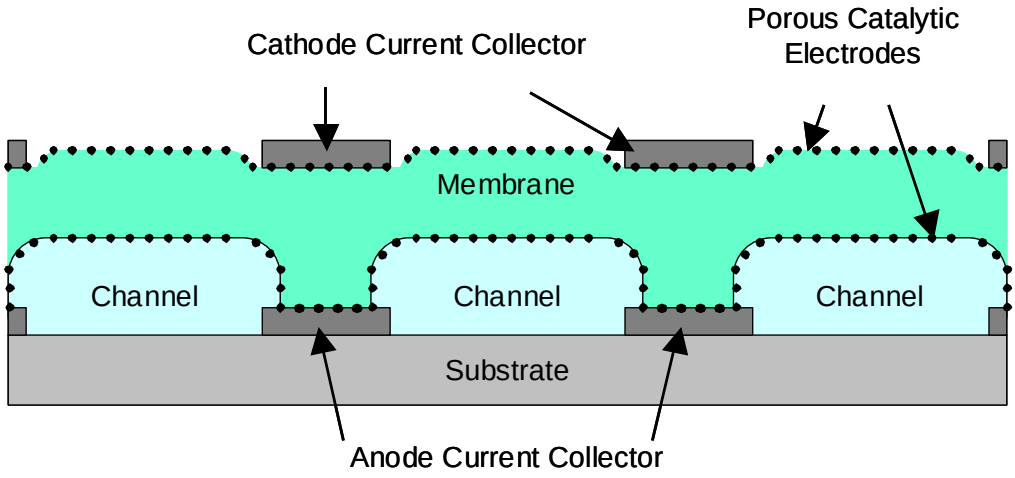

(a)

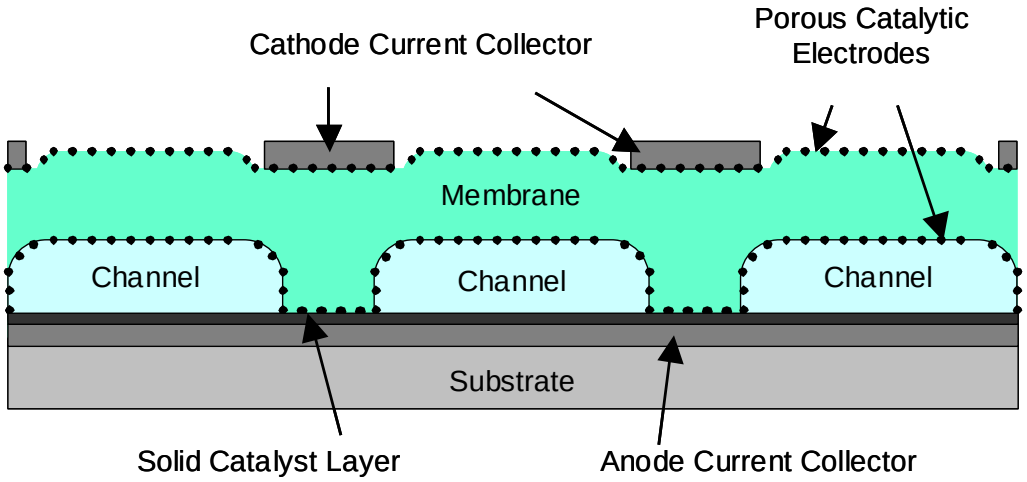

(b)

Figure 7.1: Cross-sectional view of the microchannels in the microfabricated direct methanol fuel cell (a) and the microfabricated direct acidic methanol fuel cell (b)

A thickness on the Ti board. The cathode was a Pt/C gas diffusion electrode with a Pt loading of 0.5 mg/cm^2 from E-TEK Inc., and the membrane was Nafion 117 from DuPont. The membrane (after pretreatment) and the cathode were hot-pressed to form a membrane cathode assembly at 130°C and 2 MPa for 3 min. The distance between the anode Pt-Ru alloy catalyst layer and the membrane was 20 mm. The anode half-cell behavior at the same condition in the cell was evaluated using 1M H_2SO_4 solution with SCE and a platinum wire counter electrode in the cathode compartment.

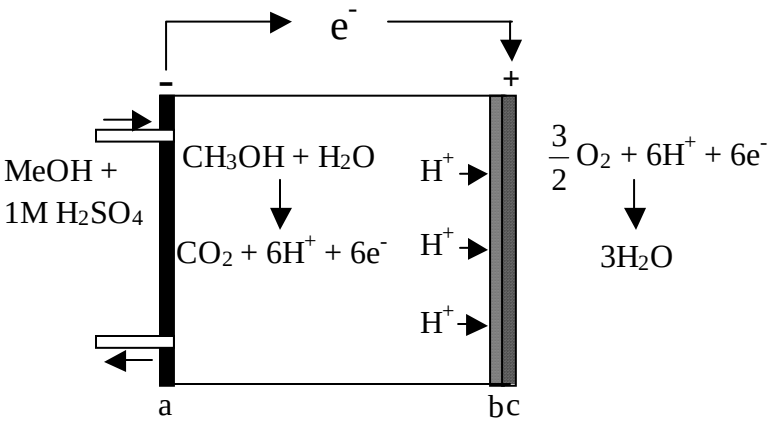

Figure 7.2: Schematic of the fuel cell using acidic methanol solution as the fuel and proton transport medium

The effectiveness of the Pt-Ru alloy catalysts deposited on the current collector on the bottom (or opposite side) of the microchannel was tested in a microfabricated anode half-cell. The 3.0 μm-thick SiO_2 was deposited by PECVD at 100°C. The size of the microchannels was 0.30 mm × 0.018 mm × 15.0 mm. The Pt-Ru loading on the inner wall of the membrane of the microchannel was 38 $\mu g/cm^2$ and the thickness of the Pt-Ru alloy layer on the bottom side of the microchannels was 1080 Å. The current collector was Au, and a 45 Å thick Ti layer was deposited between Pt-Ru alloy and Au to improve adhesion. A reservoir was built on the top of the channel for the 1M H_2SO_4 solution. The SCE reference electrode and a platinum wire counter electrode were used for the anode current-voltage curve measurements.

7.3 Results and discussion

The oxidation behavior of the methanol on the Pt or Pt-Ru alloy catalyst has been studied in acidic electrolytes because the addition of acid can improve the solution conductivity (61-63). The linear sweep voltammetry curves for the oxidation of a 1 M methanol solution with different H_2SO_4 concentrations on a sputter-deposited Pt-Ru alloy at 60 °C are shown in Figure 7.3. It can be seen that the current density for methanol oxidation on the Pt-Ru alloy without H_2SO_4 in the solution was very low. When 0.5 M H_2SO_4 was mixed with the methanol solution, the oxidation current increased significantly because H_2SO_4 increased the conductivity of the methanol solution. Table 7.1 lists the conductivity of the 1 M methanol solution with different H_2SO_4 concentrations at room temperature. The dependence of the methanol oxidation current on the acid concentration in the solution is consistent with the conductivity of the

solution. There was little difference in the oxidation current with H_2SO_4 concentrations above 1M because of the modest change in the solution conductivity.

Table 7.1: Conductivity of 1M methanol solution with different sulfuric acid concentration at room temperature

Concentration of H_2SO_4 (M)	0.00	0.25	0.50	1.00	1.50	2.00
Conductivity (s/cm)	0.00003027	0.0126	0.2509	0.4420	0.5619	0.6589

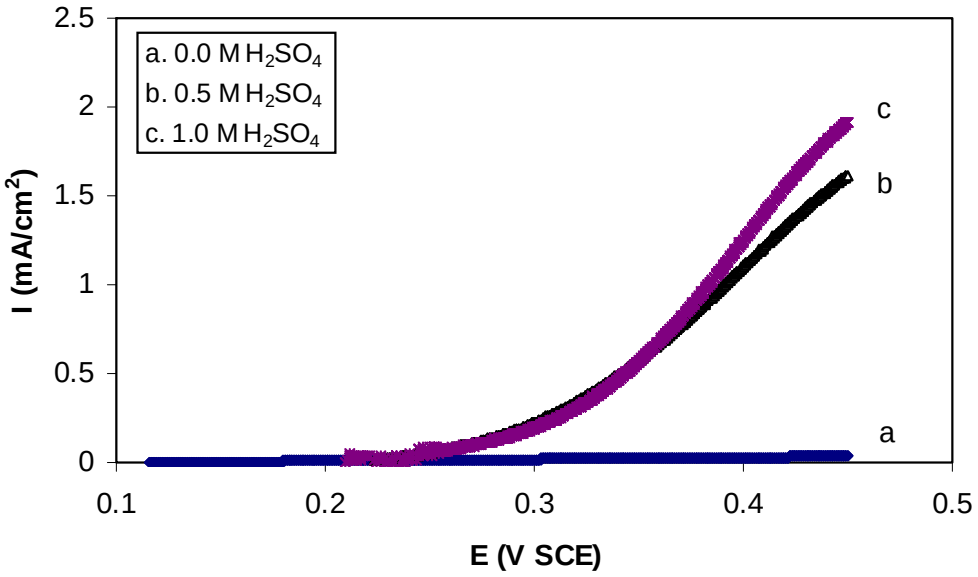

Figure 7.3: Oxidation of 1 M methanol solution with different H_2SO_4 concentration on the sputter deposited Pt-Ru alloy

It has been reported that the decomposition/electrooxidation process of methanol on the Pt-Ru alloy can be explained by a bifunctional reaction mechanism; the methanol oxidation activity mainly depends on the surface structure of the Pt-Ru alloy and the Pt:Ru composition (40, 64-65). Figure 7.4 shows current-time curve for 1 M methanol oxidation in a 1 M H_2SO_4 solution at the electrode potential of 0.25 V SCE and 60ºC on the sputter deposited Pt-Ru alloy. The oxidation current had a steep decrease during the first 10 min of the experiment, reaching a steady-state value. In the acidic solution, the catalytic activity of the sputter-deposited Pt-Ru alloy is lower than that of the carbon supported and unsupported Pt-Ru alloy catalyst reported in the literature (59, 65).

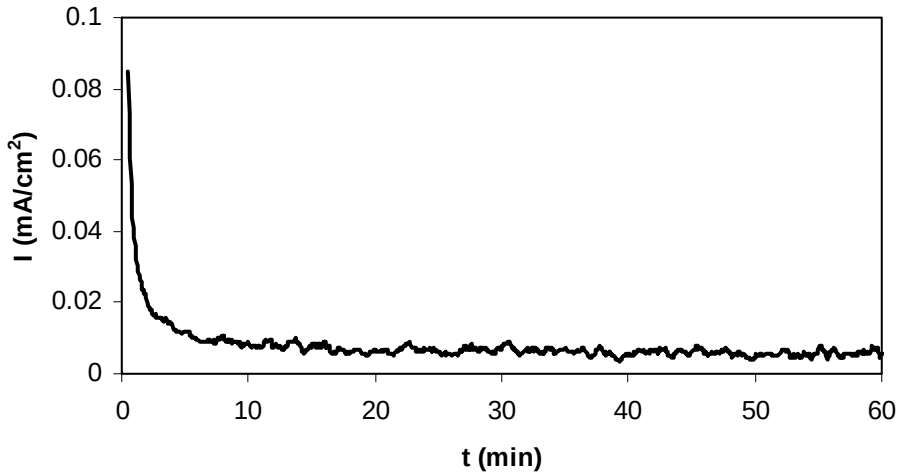

Figure 7.4: Current-time curve for 1 M methanol oxidation in 1 M H_2SO_4 solution at 0.25 V SCE and 60ºC on the sputter deposited Pt-Ru alloy

Figure 7.5 shows the performance of the acidic methanol fuel cell utilizing 1 M methanol as the fuel and 1 M H_2SO_4 as the proton transport medium. The cell was operated at 40°C to 80°C with ambient air for the air cathode. It can be seen that the performance of the cell increased with temperature. The acidic methanol analyte solution does transport protons generated on the Pt-Ru anode catalyst layer to the membrane when the Pt-Ru alloy is remote from the Nafion membrane. The protons are transported through the acidic methanol solution to the membrane, for migration to the cathode. However, the performance of the acid methanol fuel cell was not as good as typical DMFCs where membrane electrode assemblies with high anode surface area are used. For example, typical DMFCs have an open-circuit potential of 0.5-0.7 V and a current density of 0.3-0.6 A/cm^2 at 0.2 V and 90 °C (59), although results do vary considerably from study to study. The acidic methanol fuel cell had an open-circuit potential of 0.35 V and the current density was about 0.1 mA/cm^2 at 0.2 V and 80 °C.

In order to determine the performance limiting components in the acidic methanol fuel cell, a series of half-cell studies were performed. Figure 7.6 shows the current-voltage curves of the anode half-cell under the same condition as the acidic methanol fuel cell in Figure 7.5. The performance of the anode is comparable to that of the full acidic methanol fuel cell. Therefore, the performance of the acidic methanol fuel cell appears to be mainly limited by the anode reaction. One reason for the modest anode current is that the sputter-deposited Pt-Ru alloy has a lower catalytic active surface area compared to the carbon supported Pt-Ru alloy particles. Another reason is that the protons generated on the anode have to pass through the interface between the anode and acidic methanol

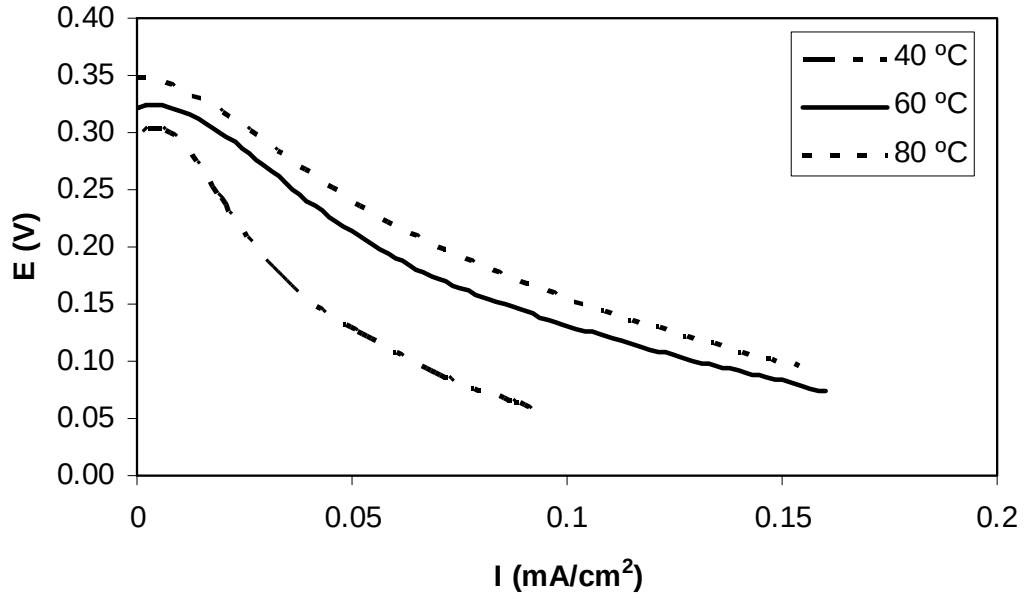

Figure 7.5: Performance of the acidic methanol fuel cell utilizing 1 M methanol and 1 M H_2SO_4 solution as the fuel and proton transport medium at different temperature

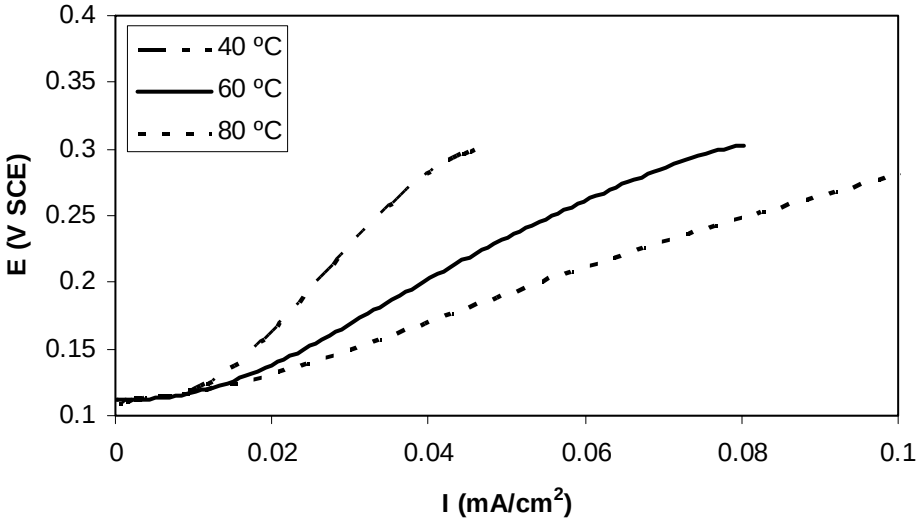

Figure 7.6: Anode performance of acidic methanol fuel cell utilizing 1 M methanol and 1 M H_2SO_4 solution as the fuel and proton transport medium at different temperature

solution, acidic methanol solution, and the interface between acidic methanol solution and the membrane.

In the microfabricated cell with SiO_2 as the PEM, the anode half-cell experimental results indicated that the optimum Pt-Ru alloy catalyst loading on the membrane of the anode was 26-38 $\mu g/cm^2$. The higher catalyst loading on the membrane led to decreased anode current because the porosity of the catalyst layer became lower and blocked proton transport into the membrane. Although the acidic methanol fuel cell described in Figure 7.5 has modest performance, it shows that the anode catalyst loading could be increased by depositing the Pt-Ru alloy on the supporting walls in the microchannel chamber and using the acidic methanol solution as fuel. Figure 7.7 shows the performance of the anode half-cells with and without Pt-Ru alloy on the walls of the anode chambers in the microchannels using 1 M MeOH and 1 M H_2SO_4 or 1 M MeOH as fuel at room temperature. The flow rate of the fuel was 1 ml/hr. After depositing more Pt-Ru alloy on the anode wall in the microchannel, it can be seen that the performance of the anode improved significantly. The acidic methanol solution effectively increased the anode active surface area from just that on the membrane to that coating the anode-chamber wall. The use of the remote Pt/Ru catalyst and acidic methanol fuel is a particularly attractive option for use in microchannel-based fuel cells. The ability to fabricate an extended anode catalytic area enables higher currents to be achieved compared to anodes restricted to the membrane surface only. Since steady-state operation would not change the acid content of the analyte, the optimum feed would be a methanol and water mixture.

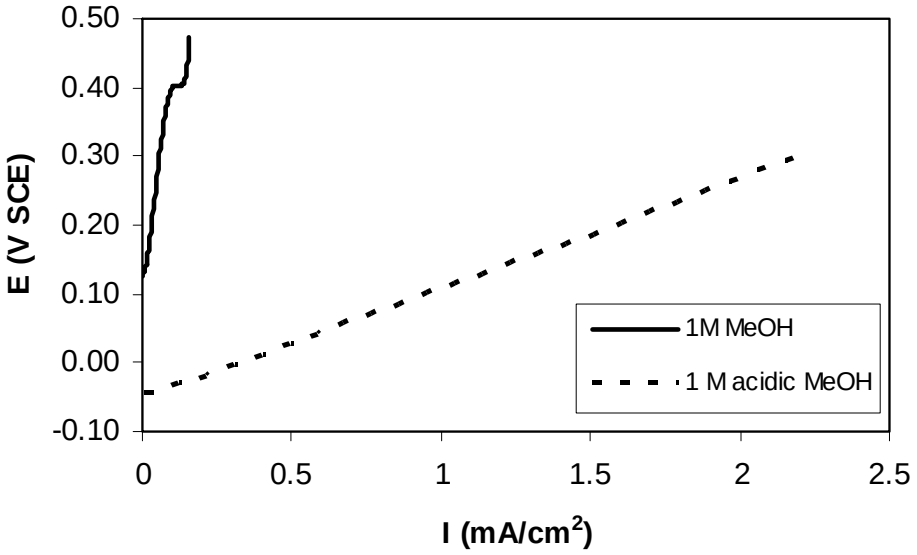

Figure 7.7: Performance of the anodes with Pt-Ru alloy on the anode chamber wall in the microchannel using 1 M MeOH and 1 M H_2SO_4 as the fuel and without Pt-Ru alloy on the anode chamber wall using 1 M MeOH as the fuel at the room temperature.

7.4 Conclusions

In the microfabricated fuel cells, SiO_2 was used as the proton exchange membrane, and a solid Pt-Ru alloy layer was directly sputter deposited on the membrane as the anode catalyst and current collector. The Pt-Ru alloy thus produced has a lower catalytic activity than the carbon supported Pt-Ru alloy in a typical direct methanol fuel cell. For the microchannel fuel cell, the optimum Pt-Ru alloy loading on the membrane is 26-38 $\mu g/cm^2$ for compromising the oxidation rate of methanol, electrical conductance, and porosity. Depositing Pt-Ru alloy on the bottom of the channel and using an acidic methanol solution as the fuel increased the anode catalyst loading in the microchannels. The protons generated on the catalyst on the anode chamber wall can be transported to the membrane through the acidic methanol. The performance of the anode thus made in the microchannel fuel cell is improved significantly.

CHAPTER 8

SILICON DIOXIDE MEMBRANES

Plasma-enhanced chemical vapor deposition (PECVD) silicon dioxide was studied as a proton exchange membrane (PEM) for use in thin-film microfabricated fuel cells. The ionic conductivity was studied for different deposition conditions and temperature was shown to have the largest effect. Even for low temperature deposition (100°C), the resistivity of the oxide films was higher than traditional polymer electrolyte membranes, e.g. Nafion, but they were also much thinner. Results from fuel cells with silicon dioxide membranes operating on hydrogen were shown in the earlier chapter that focused on sputtered catalyst electrodes. The ionic conductivity and other fundamental experiments on SiO_2 membranes are presented in this chapter along with results from fuel cells operating on methanol. The results of cells operating with humidified hydrogen were presented in chapter 6 demonstrating the effects of anode fabrication. Analysis of the SiO_2 membranes and their contribution to the limitations of devices operating on hydrogen and methanol are presented.

8.1 Introduction

Proton exchange membranes can be used in low-temperature fuel cells that operate with either hydrogen or methanol (21). The solid membrane in conventional fuel cells are usually a perfluorinated polymer with sidechains terminating in sulfonic acid moieties, such as Nafion. Membranes in PEM fuel cells generally contain water to keep the conductivity high. Methanol crossover causes a mixed potential and poisoning of the oxygen reduction reaction (22), leading to decreased performance.

Compared to conventional fuel cells, a PEM in a microfabricated fuel cells should be thin to match the thickness of the other materials, such as insulators on electronic devices. The use of an alternate membrane material with a higher resistance to methanol crossover and less dependence on water concentration is desired for thin-film membranes. The ionic conductivity, however, can be lower because the film is thinner. The deposition temperature of PECVD silicon dioxide has been shown to have a large effect on silanol and water concentrations in the film, leading to increased polarity and therefore higher ionic conductivity (32). The resistance to methanol permeation through inorganic glasses is very high. In addition, the mechanical properties make it suitable for use in the thin-film design being used, making it an attractive alternative to be studied.

8.2 Experimental Method

The deposition of SiO_2 took place in a Plasma-Therm PECVD system (Plasma-Therm, St. Petersburg, FL) at temperatures of 60-200°C. The reactant gases were silane and nitrous oxide with a N_2O:SiH_4 ratio of 2.25 and operating pressure of 600 mTorr. Deposition times of 60-75 minutes produced film thicknesses, measured with an Alpha-Step surface profilometer (KLA-Tencor, San Jose, CA), between 2.4 and 3.4 μm.

All electrochemical measurements, including impedance spectroscopy (IS) and linear voltamagrams, were performed with a PerkinElmer PARSTAT 2263 (EG&G, Princeton, NJ) electrochemical system. The scan rate for linear sweep voltametry was 1 mV/s. Ionic conductivity was measured with impedance spectroscopy through SiO_2 films deposited onto aluminum-coated substrates and contacted with a mercury probe, as well as with actual cells. The frequency range for the impedance measurement was from 100 mHz to 1 MHz, with an AC signal amplitude of 10 mV. Half-cell devices were

fabricated with the fuel delivery channels and sputtered catalyst under the SiO_2 PEM. Instead of a cathode, epoxy was used to form a well on top of the devices and filled with a 1 M sulfuric acid solution. Measurements were made with a saturated calomel electrode (SCE) and a Pt wire as the reference and counter electrodes, respectively, placed in the sulfuric acid solution. A PHD 2000 Programmable Syringe Pump (Harvard Apparatus, Holliston, MA) delivered liquid fuels and controlled the flow rates. Hydrogen was supplied with a pressurized tank of ultra high purity grade gas that passed through a bubbler to humidify the feed.

The other details of fabricating the thin-film fuel cells have been described earlier, including the use of sacrificial polymers to form microchannels for fuel flow, sputtered catalyst layers at the anode and thick-film catalyst ink at the cathode.

8.3 Measurement of ionic conductivity

The requirements for the proton exchange membrane are different from the traditional PEM, e.g. Nafion, due to the mechanical properties and thickness required in microfabricated fuel cells. Here, SiO_2 deposited by PECVD are shown to work as stand-alone membranes. Two techniques used to measure ionic conductivity were impedance spectroscopy and direct ionic conductivity. Impedance spectroscopy is performed on samples of the membrane materials that have been deposited onto a layer of metal. Meanwhile, the ionic conductivity measurements require that both sides of the membrane be exposed. Impedance spectroscopy is a method to measure the conduction of ions in a film by comparing the real impedance to imaginary impedance over a range of frequencies. The films were deposited onto a metal layer, and then placed on a mercury

probe. The potentiostat was connected to the mercury probe and swept through frequencies from 2 GHz to 100 Hz.

Figure 8.1 shows the ionic conductivity of silicon dioxide vs. deposition temperature. As the deposition temperature decreased, the conductivity increased due to higher silanol concentration and lower density. The conductivity of the films was much lower than for other commonly used PEMs, such as Nafion, but they are also much thinner than other fuel cell membranes, offsetting some of the difference in resistance. Extruded Nafion membranes (equivalent weight of 1100) have area resistances of 0.1-0.35 Ω-cm^2 (66). The area resistance of a 3 μm thick SiO_2 film deposited at 100°C is 1200 Ω-cm^2 at room temperature. The relatively high resistance leads to a decrease in cell voltage at higher current. The SiO_2 films used in these devices were adequate to investigate the other parameters, such as the anode and cathode catalyst loading.

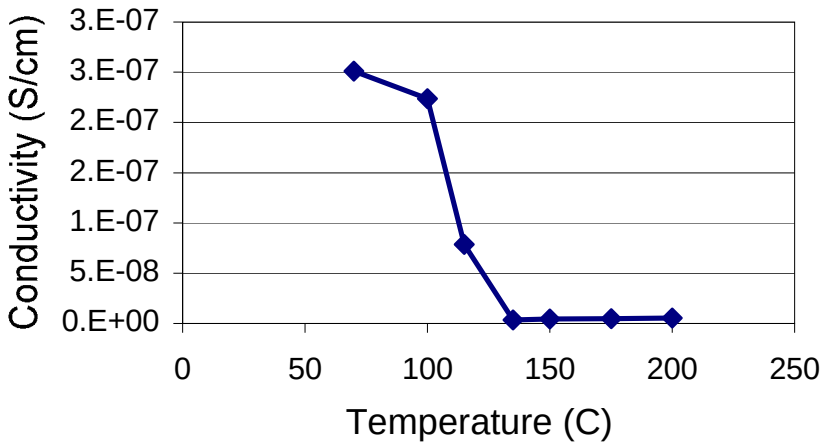

Figure 8.1: Effect of deposition temperature on ionic conductivity of SiO_2

SiO_2 membranes supported on glass frits as described in the experimental method chapter were placed between two vials containing 2.0 M KCl solution. A potential was applied across the platinum wires resulting in a flux of protons through the membrane. The resistance of the membrane was calculated by subtracting the solution's resistance from the total resistance. Figure 8.2 shows data from a sample of SiO_2 deposited at 100°C and measured at temperatures up to 80°C. An increase in conductivity was observed with increasing temperature. The data at ambient conditions for the membranes deposited on porous frits and measured in the electrochemical cell were close to the impedance spectroscopy measurements for similarly deposited films on the metallized substrates.

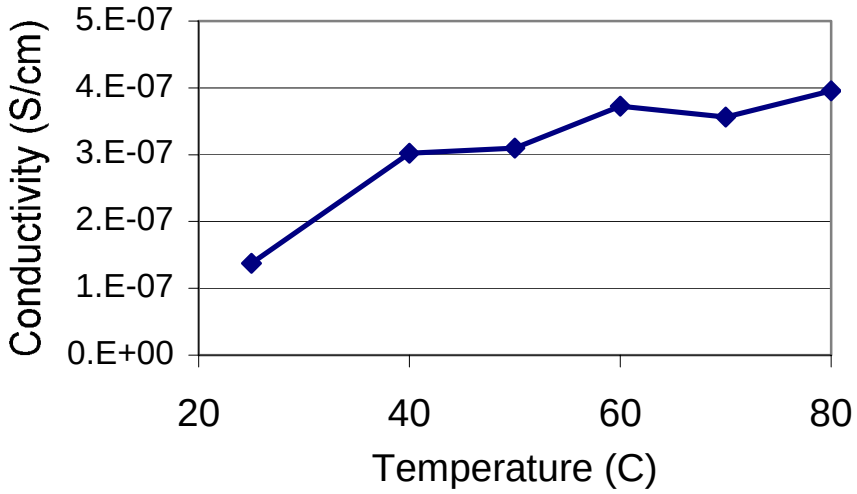

Figure 8.2: Conductivity of low-temperature deposited SiO_2 at different temperatures

8.4 Silicon dioxide membranes in direct methanol fuel cells

Half-cell devices were fabricated and tested to evaluate the anode performance with different fuels and provide a comparison for the full cell tests. A solid layer of Pt/Ru was deposited before the sacrificial polymer was patterned, as well as a porous layer on top of the patterned features to be in contact with the membrane. The catalyst weight at the membrane surface was 17 $\mu g/cm^2$.

The methanol in water concentration was 1 M. The acidic methanol mixture contained 1 M sulfuric acid with 1 M methanol. Figure 8.3 shows the half-cell polarization curves for methanol and acidic methanol. Adding sulfuric acid to the fuel made the solution conductive to protons. The higher active surface area, due to the conductivity of the acidic methanol solution, improved the current density. The Pt/Ru catalyst that was deposited on the walls of the channel not in contact with the membrane was utilized to increase the amount of methanol oxidation. Increasing the flow rate of the acidic methanol fuel improves the current density and open-circuit potential. The main detriment to performance at lower flow rates appears to be the formation of carbon dioxide bubbles at the anode that must be pushed out of the microchannels. With the current densities observed at 0.25 V vs. SCE (2 and 7 mA/cm^2 for 1 and 5 mL/hr, respectively), the production of gaseous CO_2 bubbles cover catalyst sites and may also restrict the proton conductance through the fuel from the bottom of the microchannels to the PEM.

Microfabricated full-cells were fabricated and tested with linear sweep voltammetry at a scan rate of 1 mV/sec from the open-circuit potential. Figure 8.4 shows

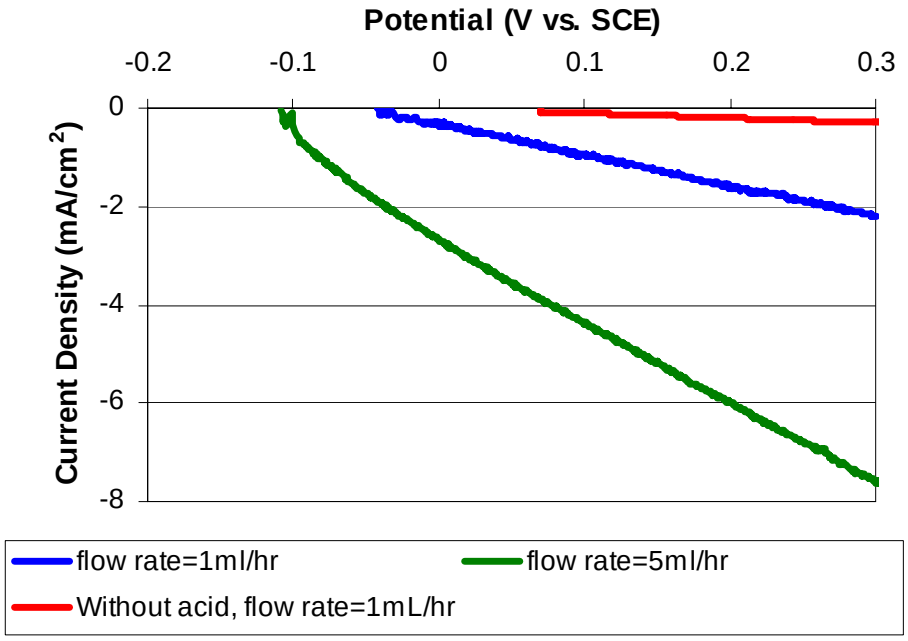

Figure 8.3: Half-cell performance of microchannels with methanol-water and acid-methanol-water solutions

the polarization and power curves for 1.0 methanol solution run at room temperature with a flow rate of 1 mL/hr in a microchannel full cell with the thick-film cathode. This sample's fabrication was described in more detail in chapter 6 as sample E. As the concentration of methanol increased from 1.0 to 4.0 M, the open-circuit potential remained at about 600 mV, but the current density fell about 30% through most of the potential range.

The current and power densities for the cell operated with acidic methanol are shown in Figure 8.5. The methanol concentration was 1.0 M and the flowrate was also 1 mL/hr. When using acidic methanol, the solid layer of catalyst at the bottom of the microchannel was utilized in addition to the porous Pt/Ru at the membrane in the oxidation of methanol because the fuel solution can conduct protons. While the open-circuit potential was lower, the peak current and power densities were much higher than the same device operating with either non-acidic methanol or hydrogen as the fuel.

8.5 Membrane analysis and discussion

PECVD SiO_2 was shown to work as a thin-film PEM in these microfabricated fuel cells. While very dependent on deposition temperature, the resistivity of the oxide films was much higher than traditional polymer electrolyte membranes, e.g. Nafion, and even though they were also much thinner, the resulting area resistance was higher. This causes the current density to be very low and requires a significant drop in operating voltage for increased current. Other factors in these cells also contribute to low power densities, such as low catalyst loading. For the different fuels used, the performance of the cells was significantly different.

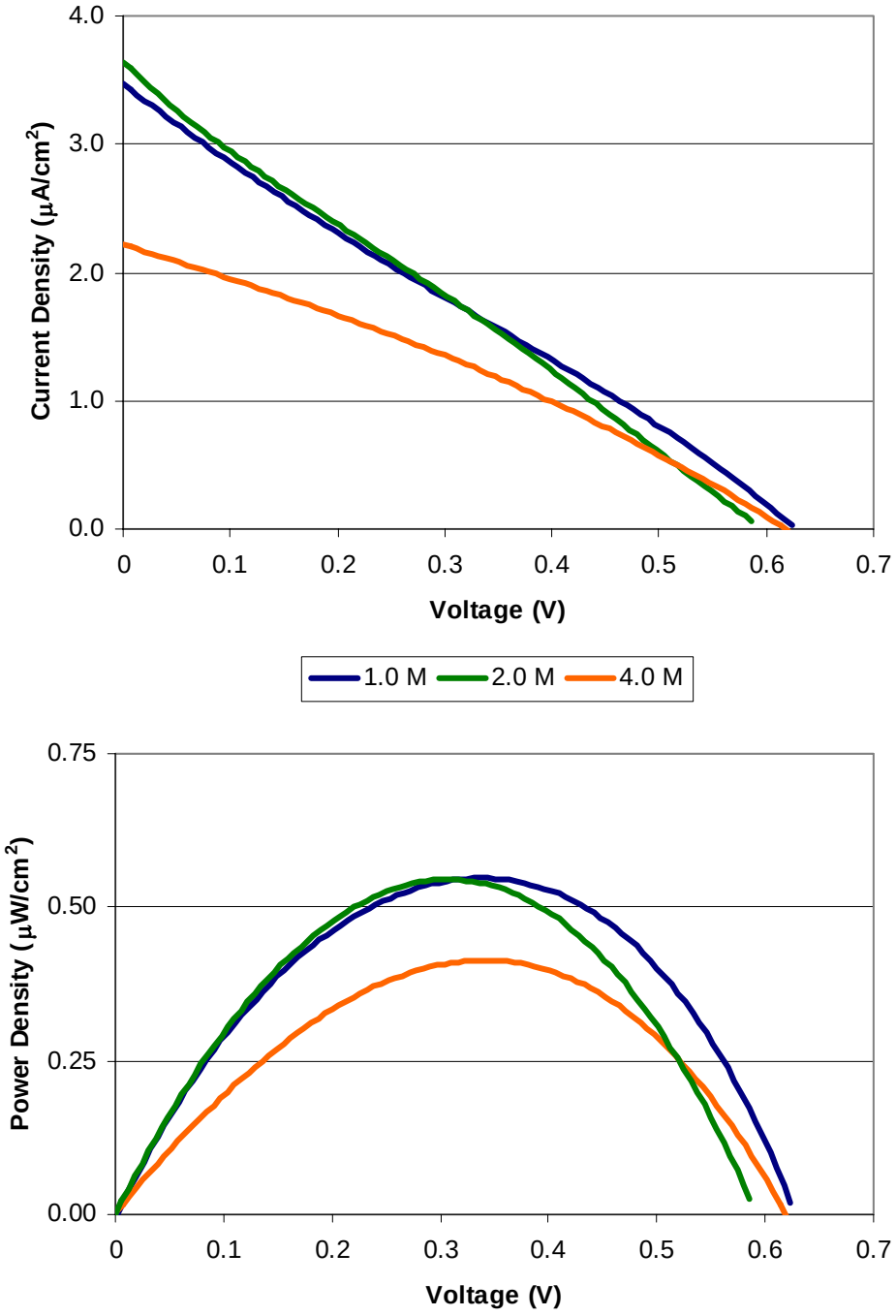

Figure 8.4: Microchannel full cell performance with different methanol concentrations at room temperature

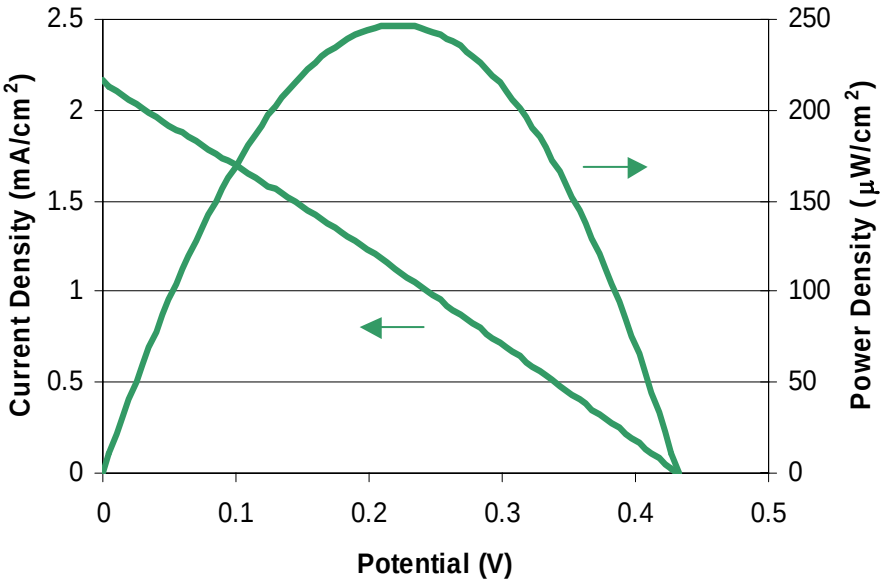

Figure 8.5: Microchannel full cell performance with 1.0 M acidic methanol at 1 mL/hr

Table 8.1 gives the overall area resistance, calculated from slope of the current density vs. voltage polarization curve, for samples operating on different fuels and conditions. The fabrication details for the samples have been previously described. Also presented are the values for membrane resistance calculated from the data shown in Figure 8.2, the thickness of the SiO_2 used in the sample, and the operating temperature. For samples A and B, the overall cell resistance was very high. As previously stated, the sputtered cathode in sample A was the device-limiting feature. For sample B, the anode catalyst weight was shown to be the most significant contributor to the performance, but as the temperature increased to 60°C the PEM resistance accounted for about half of the overall resistance. Sample C had more Pt/Ru at the anode than sample B, resulting in higher current densities throughout the potential range at ambient and elevated temperature. The increased catalytic activity of the anode at 60°C resulted in the resistance of the cell being very close to that of the SiO_2. With the embedded catalyst technique employed in sample D, the anode improved to such an extent that the resistance of the SiO_2 determined the performance of the device at ambient conditions.

When operating on 1.0, 2.0, or 4.0 M methanol, the current densities were extremely low, indicating that the oxidation of the methanol at the anode was the most significant limitation. A positive feature of the methanol operation was the open-circuit potentials around 600 mV. These values were less than with hydrogen, but were considered very good for methanol with such a thin PEM.

The performance of the cell operating on acidic methanol was dramatically different. The significant increase in useful catalyst area with acidic methanol has already been discussed in detail the previous chapter. While this accounts for the

Table 8.1: Area resistance of micro fuel cells with different operating conditions

Sample	Fuel	Temperature (°C)	Area resistance (Ohm cm^2)	Calculated SiO_2 resistance (Ohm cm^2)
A	Hydrogen	Ambient	1.10E+05	2667
A	Hydrogen	60	2.51E+04	842
B	Hydrogen	Ambient	1.80E+04	2667
B	Hydrogen	40	4310	1067
B	Hydrogen	60	1581	842
C	Hydrogen	Ambient	1.32E+04	2667
C	Hydrogen	60	909	842
D	Hydrogen	Ambient	2381	2667
E	1.0 M Methanol	Ambient	1.95E+06	2000
E	2.0 M Methanol	Ambient	1.70E+06	2000
E	4.0 M Methanol	Ambient	3.10E+06	2000
E	Acidic methanol	Ambient	310	2000

increased current density, another important result was the dramatic decrease in open-circuit potential. Also, the overall cell resistance calculated from the slope of the current density vs. voltage was actually less than the SiO_2 resistance from other tests. These two factors indicate that the addition of acid to the fuel solution changed the properties of the SiO_2. This change, which resulted in decreased resistance to proton and methanol transport across the PEM, was of a destructive nature. With time, the acidic solution caused the SiO_2 to develop cracks or holes and fuel leakage was observed.

8.6 Conclusions

Micro fuel cells utilizing sacrificial polymer-based microchannels and thin-film SiO_2 membranes have been successfully fabricated and tested. Low-temperature PECVD silicon dioxide shows promise for use in integrated thin-film devices. Lowering the deposition temperature dramatically increased the conductivity of the films to an acceptable level for the current densities achieved with the fabricated electrodes used in this study.

The conductivity of the membranes and the open-circuit potentials are too low. Thicker layers of SiO_2 can improve the open-circuit potential, but result in even higher resistance and lower current densities. Making thinner SiO_2 layers improves the ionic conductivity, but results in lower yield due to the fragile nature of the glass. The use of acidic methanol also causes damage to the SiO_2, limiting the viable lifetime of the devices.

While the performance was shown to increase dramatically with increased temperature, the ability of these devices to maintain an elevated temperature on their own is questionable because of their small size. The amount of waste heat produced by the

fuel cells that can be retained will affect their level of performance because of the temperature dependence of the cells. The goal will be a design with maximum insulation for the fuel cells to keep the operating temperature as high as possible. They will most likely find usage in applications where high current or power output is not as important as the high energy density they can offer at any temperature.

CHAPTER 9

POLYMER ON SILICON DIOXIDE MEMBRANES

To further improve the mechanical strength of the micro fuel cells, thin layers of polymers have been deposited over the SiO_2 PEM. These double layer membranes offer better strength than SiO_2 alone, and better resistance to fuel permeation than a polymer only thin-film membrane. Two polymers that were successfully used with SiO_2 in double-layer PEMS were polyimide and Nafion. In addition, experiments performed on polyphenylene sulfonic acid (PPSA) are presented.

9.1 Polyimide

9.1.1 Polyimide background

Polyimides are a class of polymers commonly used as dielectrics or protective overcoats in semiconductor devices. They typically have a good combination of properties, including thermal stability, mechanical toughness, and chemical resistance. In semiconductor fabrication, polyimides are applied to the substrate as a liquid through spin-coating. The films are then thermally cured into the stable polymer layer that can be patterned through typical lithographic processes, i.e. the use of photoresists and plasma etching.

The use of polyimides as encapsulating materials for sacrificial polymer-based microchannels was extensive for PNB. Solvent incompatibility made them unusable on top of polypropylene carbonates. In other words, the PPC was soluble in the polyimides' solvent, n-methyl pyrolidone (NMP). This resulted in the destruction of patterned polycarbonate features when polyimide was spin-coated directly onto PPC. The use of

SiO_2 as a solvent barrier prevented the dissolution of the underlying features, opening enabling the study of polyimide as a thin-film PEM.

Curing of a polyimide film takes place through an imidization reaction of polyamic acid. Figure 9.1 shows chemical structure of the polyimide solution PI-2611 from HD Microsystems (city, state) before (a) and after (b) the ring-closing imidization reaction. Uncured polyimide solutions consist of the polyamic acid form of the material and therefore have a higher dielectric constant. These acid groups offer the possibility of ionic conductivity (proton transport) through the film making them a viable choice for thin-film PEM studies. The focus of this work was to keep as much polyamic acid as possible from curing during the processing of micro fuel cell devices so that the ionic conductivity would remain high.

9.1.2 Polyimide modification and curing

Additives were added to PI-2611 solution to attempt to modify the polymer and prevent it from curing as readily. Table 9.1 gives the compositions of the diluted PI-2611 solutions with acid and base additives. Samples of the solutions were spin-coated onto aluminum-coated glass slides and cured at different temperatures. All samples were soft-baked on a 100°C hotplate for 15 minutes. One sample of each solution was cured in a nitrogen-purged tube furnace for 1 hour at 200°C and one of each solution was cured in the furnace for 1 hour at 300°C.

Fourier Transform Infrared (FTIR) spectroscopy was used to analyze the extent of curing of the films. Figures 9.2 shows the spectra for one sample, PI-4, between 1285 and 1595 cm^{-1}. The 100°C soft baked sample is shown in green, the 200°C cured film is

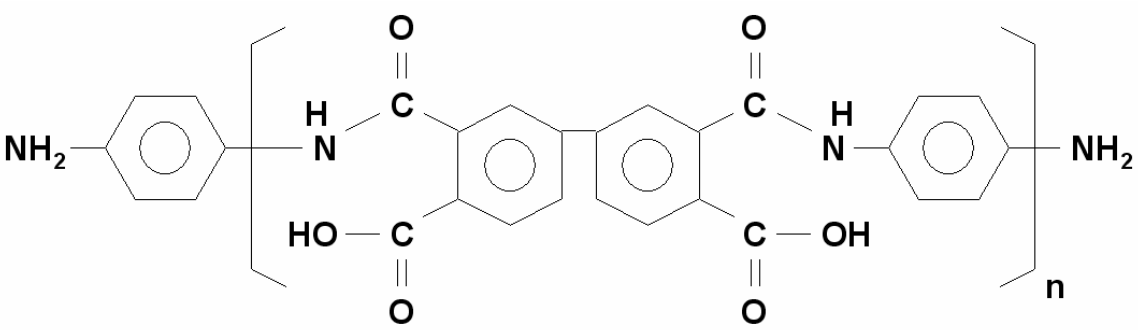

a

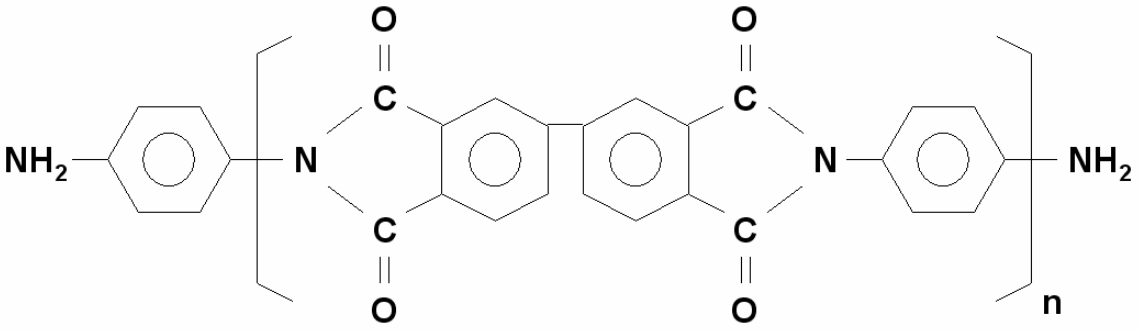

b

Figure 9.1: Chemical structure of PI-2611 before (a) and after (b) the ring-closing imidization reaction

Table 9.1: Modified polyimide solutions

Sample	Polymer wt.% solids	Additive name	Additive wt. %
PI-4	7.02%		0%
PI-5	7.20%	acetic acid	10.39%
PI-6	6.46%	diflouroacetic acid	18.67%
PI-7	6.10%	potasium hydroxide	10.36%
PI-8	3.73%	potasium hydroxide	6.32%

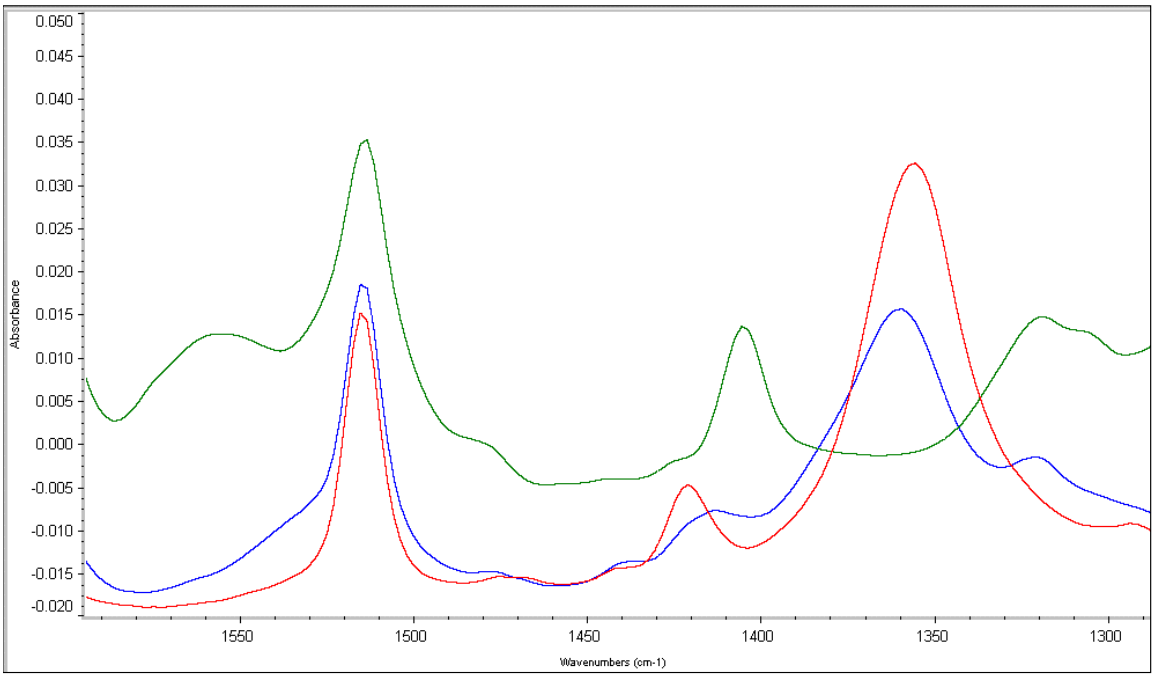

Figure 9.2: FTIR spectra of PI-4 samples

shown in blue, and the 300°C cured film is shown in red. Curing can be seen in the peak at 1359 cm^{-1} that increases with increasing temperature. The spectra from samples PI-5 and PI-7 were very similar to the PI-4 spectra shown. Meanwhile, the diflouroacetic acid added to sample PI-6 appeared to have reduced the extent of curing for the sample taken to 200°C. Its peak at 1359 cm^{-1} was smaller than the other samples cured at 200°C.

Using the FTIR spectra, the following equation can be used to determine the extent of imidization:

$$\text{Cure}\,\% = \frac{(A_{1359} / A_{1516})}{(A_{1359} / A_{1516})_{ref}} \qquad [9.1]$$

where A_{1359} and A_{1516} are the measure of absorbance peak height at 1359 cm^{-1} and 1516 cm^{-1}, respectively. Wave number 1359 cm^{-1} represents the ring closing peak and increases in absorbance with the extent of cure, while 1516 cm^{-1} represents the ring breathing vibrations. The absorbance peaks from the PI-4 sample cured at 300°C were used as the reference values in the calculations of the extent of imidization. Table 9.2 shows absorbance values at the appropriate wave numbers and the percent imidization based on the above equation. As can be seen if Figure 9.3, all of the samples cured to a about the same extent with one hour of exposure to 300°C. When taken to only 200 °C, each of the samples partially cured. Sample PI-6, which contained diflouroacetic acid as an additive, had a lower percent imidization at 200°C than the other samples.

Table 9.2: FTIR cure analysis of modified polyimide films

Sample	Cure Temp	1359 cm^{-1}	1516 cm^{-1}	Percent Imidization
PI-4	100	-0.0013	0.0347	0.00%
PI-4	200	0.0155	0.0184	41.03%
PI-4	300	0.031	0.0151	100.00%
PI-5	100	-0.0021	0.0399	0.00%
PI-5	200	0.0222	0.0268	40.35%
PI-5	300	0.0338	0.0168	98.00%
PI-6	100	0.0002	0.034	0.29%
PI-6	200	0.0028	0.012	11.37%
PI-6	300	0.0274	0.0125	106.77%
PI-7	100	-0.0017	0.0401	0.00%
PI-7	200	0.0201	0.0175	55.95%
PI-7	300	0.0315	0.0154	99.63%

9.1.3 Measurement of ionic conductivity

The samples with polyimide on aluminum were placed on a mercury probe and connected to an LCR meter to measure the permittivity through the films. Data was recorded at two frequencies, 10 kHz and 100 kHz. Table 9.3 shows the values of permittivity obtained for each sample.

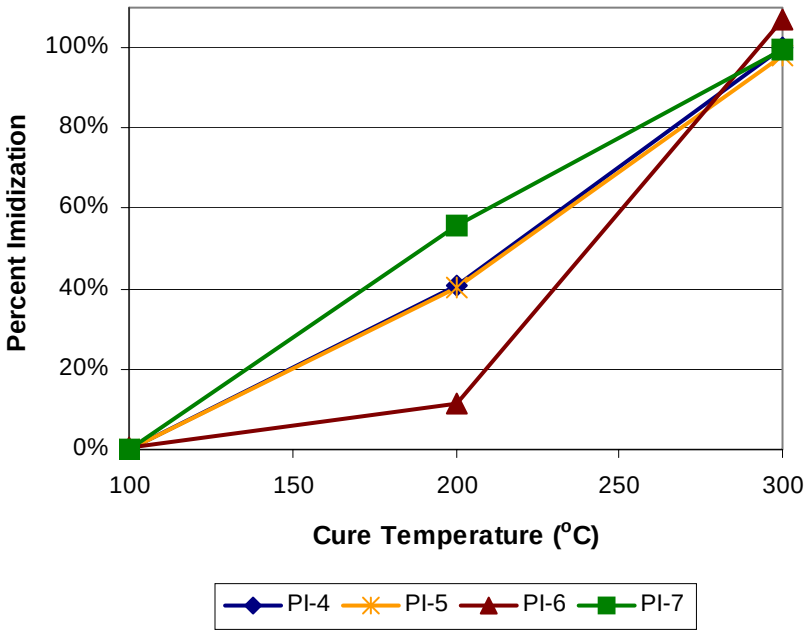

Figure 9.3: Extent of curing with temperature for modified polyimide films

Table 9.3: LCR meter data for modified polyimide films

Sample	Cure Temperature (^{o}C)	Frequency (kHz)	Capacitance (pF)	Loss (μS)
PI-4	100	10	53.9	0.238
		100	48.6	2.22
	200	10	56.1	0.086
		100	53.5	1.0
	300	10	47.5	0.082
		100	46.4	0.42
PI-5	100	10	2.4	0.0067
		100	2.28	0.057
	200	10	47.4	0.1
		100	44	1.6
	300	10	40.7	0.028
		100	39.9	0.29
PI-6	100	10	13.2	0.031
		100	12.5	0.29
	200	10	72.5	0.15
		100	73.4	1.95
	300	10	12.3	0.026
		100	11.9	0.16
PI-7	100	10	60.8	0.275
		100	54.7	2.47
	200	10	59.1	0.08
		100	57.1	1.04
	300	10	54.6	0.037
		100	53.9	0.45

9.1.4 Polyimide use in micro fuel cells

Due to the fact that attempts to modify the polyimide solutions did not result in a reduction in the extent of curing with temperature or an increase in ionic conductivity, a diluted solution of PI 2611 was used in the microfabricated fuel cells, but separate devices were not made with every modified solution. The cells were fabricated similarly to those previously described with a solid layer of Pt/Ru at the bottom of the microchannels, PPC sacrificial polymer to form the microchannels, 17 $\mu g/cm^2$ of Pt/Ru with a Ti adhesion layer at the membrane surface, then 2.4 μm of SiO_2. The diluted polyimide was spin-coated to 2 μm and then the PPC was decomposed at 200°C. The cathode was constructed using the Pt ink and porous gold current collector previously described. Figure 9.4 shows the polarization curve of the polyimide-on-SiO_2 sample. Linear sweep voltammagrams were taken from open-circuit potential at 1 mV/sec.

Two major results can readily be seen from the addition of the thin layer of polyimide in the PEM structure when compared to the results from the similarly constructed SiO_2-only fuel cell shown in Figure 6.7. First, the open-circuit potential increased by approximately 200 mV. The current density, however, is negatively affected. At ambient, the current densities are similar, but with increased temperature, the performance of the polyimide sample does not improve as drastically as the SiO_2-only sample and produces only about 20% of the current at 60°C. This relatively constant performance with temperature provides evidence that the membrane resistance was the primary limitation to device performance. The slope of the current density versus voltage polarization curve was approximately 1.8×10^4 Ω-cm^2 for each of the three temperatures

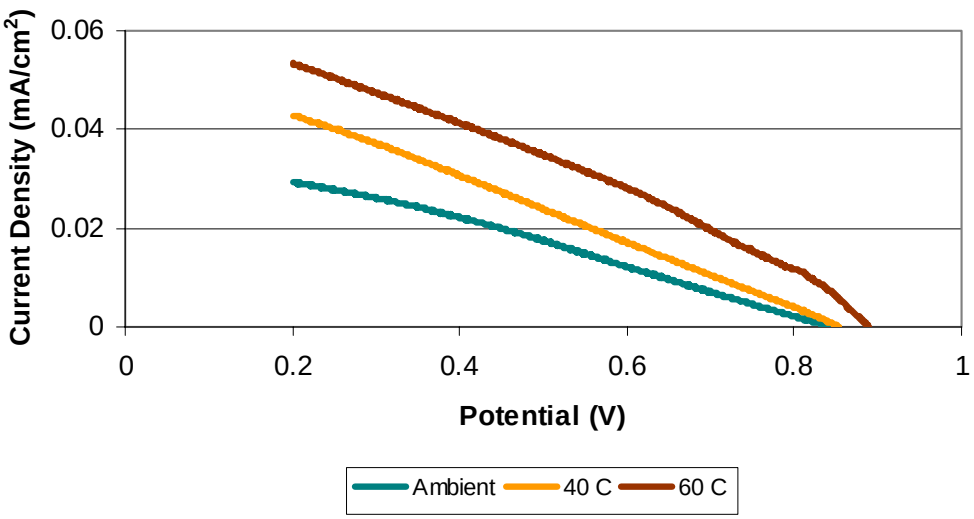

Figure 9.4: Polarization curve of SiO_2-polyimide PEM micro fuel cell

shown. The area resistance of the PI-on-SiO_2 membrane was, therefore, close to this value.

A beneficial result from the addition of polyimide was an increase in yield and stability. Not only did a greater percentage of completed devices successfully had fluid flow down the complete channel without cracks or leaks, they withstood a greater amount of physical and chemical stress without breakage. Figure 9.5 shows the polarization curve for one of these cells at room temperature with formic acid as a fuel. The current and power densities are again very low and the open-circuit potential of slightly more than 300 mV is far lower than with hydrogen fuel. Nevertheless, these were the only cells that successfully ran formic acid without breaking. The cells with SiO_2-only PEMs developed cracks and leaks due to the corrosive acid.

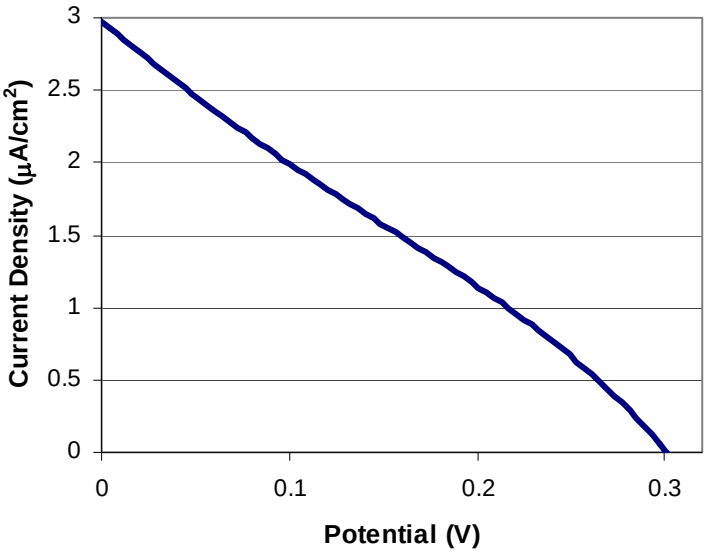

Figure 9.5: Polarization curve of SiO_2-polyimide PEM micro fuel cell with formic acid

The use of polyimide as part of a composite membrane structure provided evidence that SiO_2 PEMs could be improved with a layer of polymer. Increased open-circuit potentials and improved reliability were obtained. The polyimide layers, however, had too high of resistance to proton transport and limited the performance of the devices to such an extent that polyimide would not be a viable choice for the dual-layer membranes.

9.2 Nafion

Figure 9.6 shows the polarization and power curves at ambient temperature for a sample with Nafion cast on the SiO_2. The air-breathing cathode construction was the same as the others, but the anode contained additional catalyst, 65 $\mu g/cm^2$, and was Pt instead of Pt/Ru. The open-circuit potential was 900 mV and the current densities were remarkably higher than the above samples. While the improved open-circuit potential was due to the improved membrane, the increase in current density was mainly due to the additional catalyst. The power density of 0.6 mW/cm^2 at 0.4 V was a great improvement over previously reported results. The active area required for a continuous 1 mW power source would be less than 2 cm^2, a size that would fit the integrated sensor/IC/micro fuel cell design.

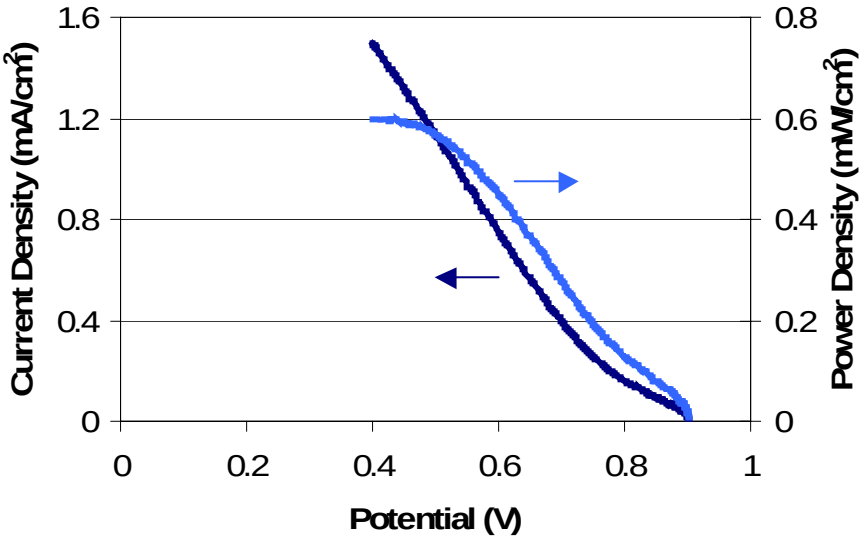

Figure 9.6: Polarization curve of SiO_2-Nafion PEM micro fuel cell

9.3 Poly para-phenylene sulphonic acid

9.3.1 PPSA background

Another polymer that was studied for use as a thin-film PEM, either by itself or on SiO2, was poly para-phenylene sulphonic acid (PPSA). The task of evaluating and optimizing PPSA for use as a PEM included E-beam cross-linking, ionic conductivity tests and use in half-cell structures. This new polymer electrolyte material was synthesized at Case Western Reserve University (Cleveland, OH) and received in solid powder form. The structure of PPSA is shown in Figure 9.7.

.

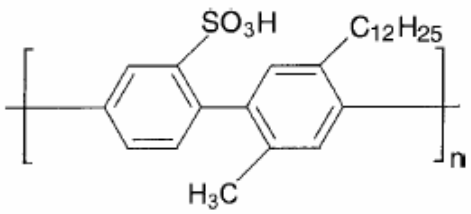

Figure 9.7: Poly para-phenylene sulphonic acid

9.3.2 PPSA crosslinking

In order to evaluate the polymer, the PPPSA was dissolved in water to form a homogeneous solution, and then spin-coated onto a silicon wafer to form a thin film. Several different spin speeds were tested. The sample was then dried under vacuum at 50^{o}C. Before crosslinking, the sample was kept away from moisture. Electron beam curing of the polymer in this study was carried out using AlliedSignal's Electron cure 30-200 AT system. The two primary variables in the crosslinking process were the E-beam dose and the back heating temperature. The structure property and interaction with water before and after E-beam crosslinking were compared.

20 wt.% poly para-phenylene sulphonic acid was spin-coated on silicon wafers. Because the solution was very dilute, the polymer could only be spun at very low spin speeds, therefore 500 rpm was used in this work. The E-beam crosslinking was investigated under a wide range of cure conditions. The accelerating voltage was set at 3 KeV and the beam current at 6 mA. The back heating temperature for this study was set at 100^{o}C. The total time involved in the cure process ranged from 160 to 800 seconds. Electron beam dose levels ranging from 1000 to 7000 $\mu C/cm^2$ were used to cure the polymer.

The film thickness was measured before and after E-beam crosslinking. Experiments were carried out to compare the solubility of the polymer film in water before and after crosslinking. The results are shown in Table 9.4, and SEM images of the polymer before and after curing are shown in Figures 9.8 and 9.9. The sample cross-linked at a dose of 5000 $\mu C/cm^2$ or above formed a thin film that did not dissolve in water, though the film was very brittle.

Table 9.4: Film thickness and solubility before and after crosslinking

Dose ($\mu C/cm^2$)		1000	3000	5000	7000
thickness (μm)	before cure	0.11	0.37	0.30	0.47
	after cure	0.15	0.40	0.32	0.50
solubility in water	before cure	dissolves in 1 min	dissolves in 1min	dissolves in 1min	dissolves in 1min
	after cure	dissolves in 1min	dissolves in 3min	does not dissolve	does not dissolve

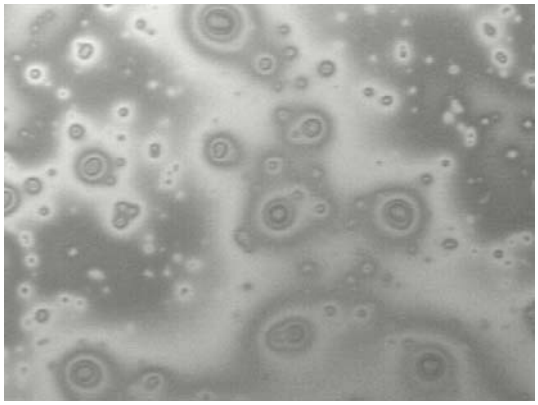

Figure 9.8: PPPSA before crosslinking

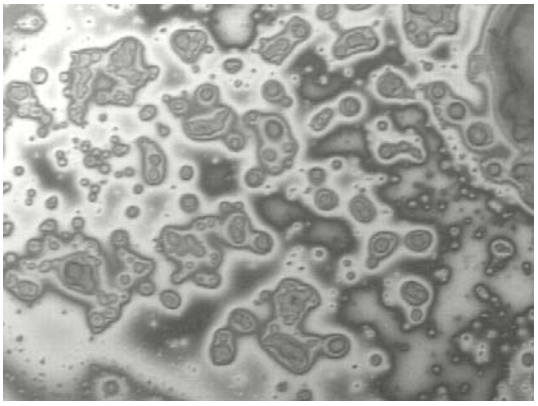

Figure 9.9: PPPSA film after crosslinking

Experiments performed on the PPSA to crosslink it with e-beam exposure showed a vast improvement in material stability. After crosslinking, the films no longer dissolved in water or methanol. The conductivity was measured before after various amounts of electron-beam exposure. Figure 9.10 shows data for two versions of PPSA. The newer material, from May 2003, had a conductivity that was much higher than the previous PPSA and retained its conductivity after crosslinking better. This version of the polymer was used for continued experiments.

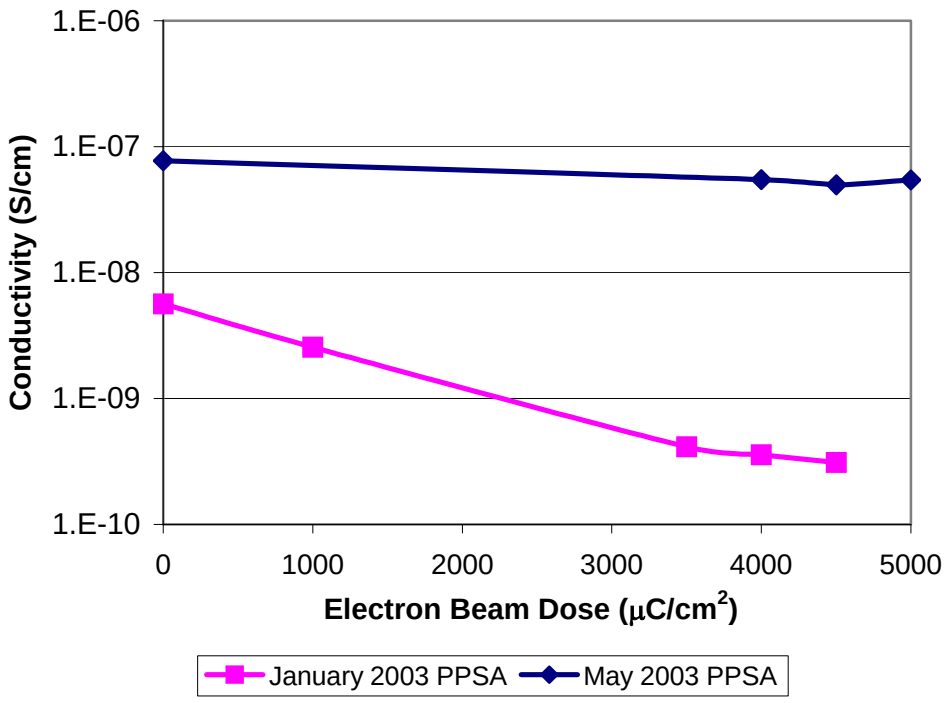

Figure 9.10: Conductivity of PPSA after e-beam crosslinking

After being measured for ionic conductivity, the PPSA films were soaked in 10% hydrochloric acid. The acid dissolved an un-crosslinked film, but for the crosslinked films, it improved the conductivity slightly. The results are shown in Figure 9.11.

Additional samples of PPSA were modified by adding 3 wt% of 2, 6-bis(4-azidobenzylidene)-4-ethyl cyclohexanone to promote crosslinking, thus reducing the amount of e-beam exposure necessary to make the films insoluble. As little as 1000 $\mu C/cm^2$ exposure made a 1 μm thick film insoluble in water or diluted acid. Again, the ionic conductivity of the samples were measured before and after being soaking in 10% HCl. Figure 9.12 shows the conductivity of the diazide-modified films with electron-beam exposure before and after being soaked in HCl. Not only does the conductivity increase with the acid soaking, but actually increases with e-beam exposure for the acid-soaked samples over much of the range studied.

9.3.3 PPSA use in half-cells

Samples of PPSA were spin-coated onto gas diffusion layers (GDL) with pre-loaded catalyst. These membrane-electrode assemblies (MEA) were supported with Al disks that had 1-mm^2 holes. A solution of 2 M H_2SO_4 with the counter and reference electrodes was kept on the side of the membrane opposite the GDL. Voltages were measured vs. a standard calomel electrode (SCE). Figures 9.13 and 9.14 show linear sweep voltammetry measurements for 1 μm thick PPSA films used as PEMs in half-cells for the oxidation of 1.0 M methanol and reduction of oxygen from air. A noticeable increase can be seen in the oxidation of methanol as the temperature increases. The increased temperature, however, appears to have very little effect on the reduction of oxygen from air.

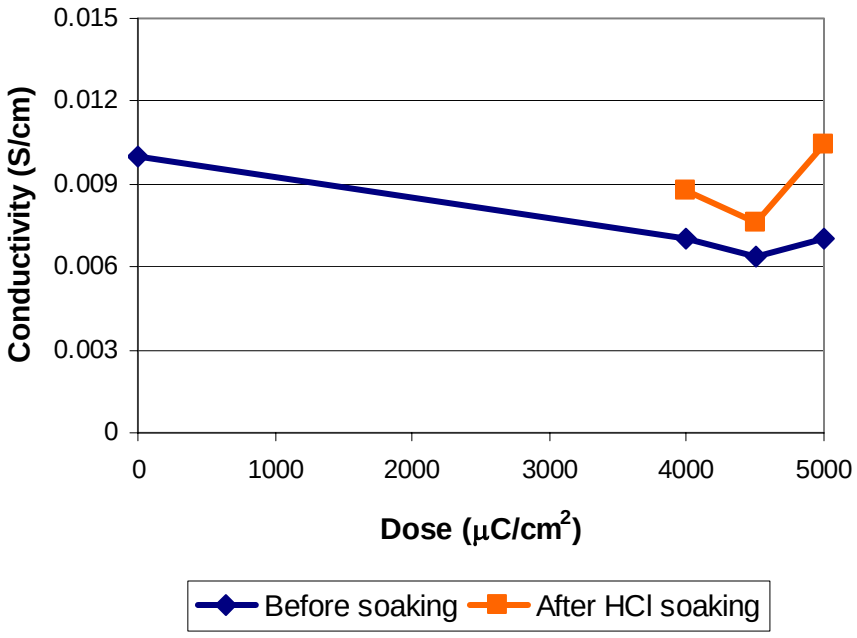

Figure 9.11: Conductivity of crosslinked PPSA before and after HCl soaking

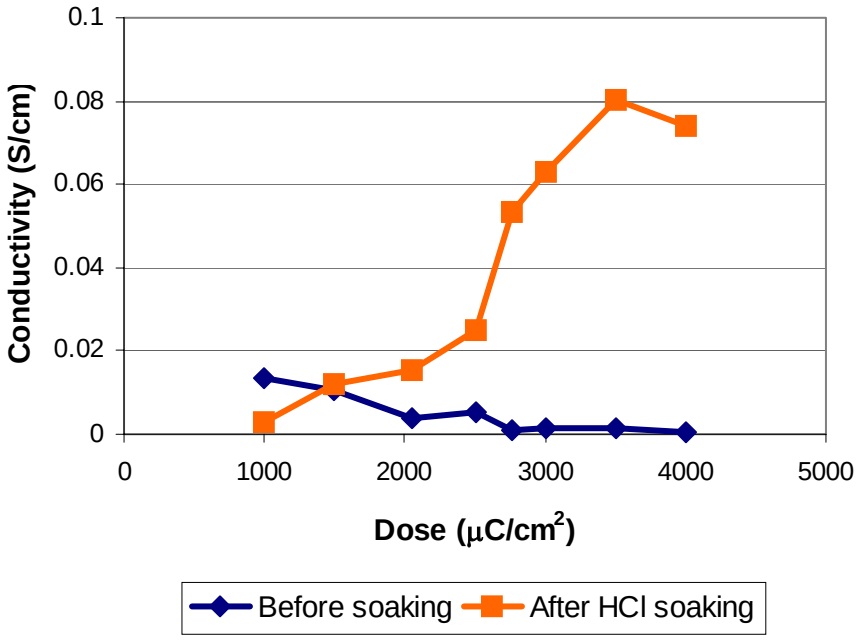

Figure 9.12: Conductivity of crosslinked PPSA with added diazide before and after HCl soaking

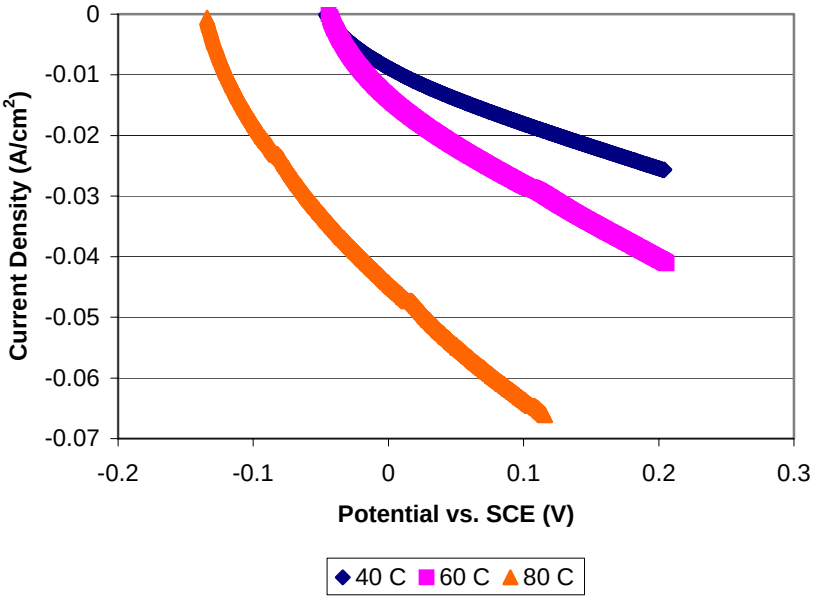

Figure 9.13: Methanol oxidation with PPSA membrane, thickness = 1 μm

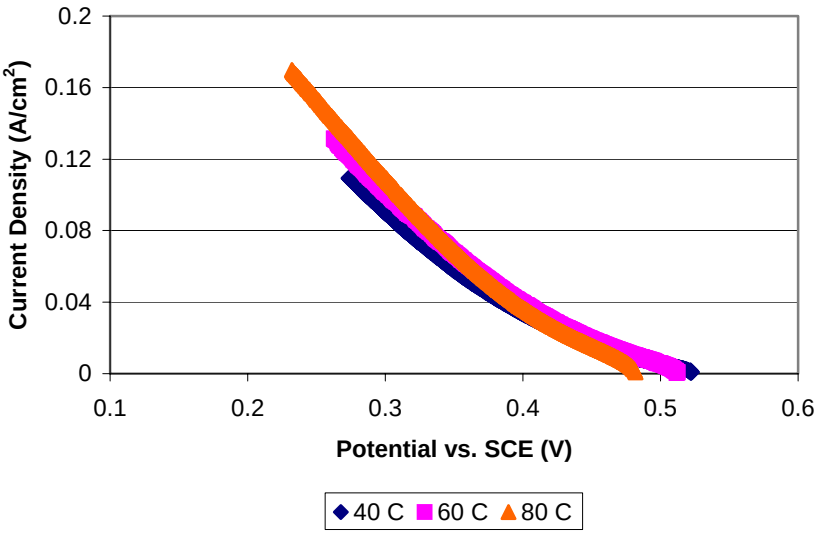

Figure 9.14: Oxygen in air reduction with PPSA membrane, thickness = 1 μm

9.4 Summary and Conclusions

Polyimide, specifically PI-2611, had been shown to work well as an encapsulating material for microchannels formed with polynorbornene. Its solvent, NMP, dissolved polycarbonate features during processing, necessitating a SiO_2 layer to act as a solvent layer, but the channels continued to have a high yield. The good mechanical properties of PI-2611 in these structures made it an attractive option for a thin-film PEM. Its dielectric properties, however, caused it to be too good of an insulator to protons as well as electrons. Even with only a partial curing, the films demonstrated too great of a resistance to proton transport than would be useful in these devices. Attempts to modify the polymer solution were not successful in significantly changing the extent of imidization with the processing temperatures used for the decomposition of the sacrificial polymer. When used in combination with SiO_2 to form a double-layer PEM in the micro fuel cells, a beneficial increase in open-circuit potential was obtained, but the high resistance caused the current and power densities to be lower than the SiO_2-only fuel cells. The improvements to the open-circuit potential and mechanical strength make this an attractive material to continue exploring. The use of different polyimides or other methods to modify the solutions may keep the extent of imidization to a minimum and the protonic conductivity high.

On the other hand, Nafion successfully increased the open-circuit potential without a loss in current density, resulting in higher power density. This should not come as a surprise since Nafion is the standard PEM material. Attempts to make a thin-film Nafion-only PEM on microchannel samples were not successful. In the composite membrane, SiO_2 serves its role to support the Nafion layer to prevent collapsing. Also,

the Nafion was deposited after the sacrificial polymer had been decomposed, thus the sensitive PEM material was not exposed to the elevated temperatures.

PPSA was expected to be the material that would be used as the thin-film membrane. While its conductivity was shown to be relatively high, after crosslinking it was very brittle and would crack when used as an overcoat for microchannels. While this polymer shows promise, it needs more work before it could successfully be used as a PEM in microfabricated fuel cells.

CHAPTER 10

PHOSPHOROUS-DOPED SILICON DIOXIDE MEMBRANES

Phosphorous-doped silicon dioxide (PSG) has been studied as a proton exchange membrane for use in thin-film fuel cells. It is deposited through plasma-enhanced chemical vapor deposition (PECVD) and has ionic conductivities two orders of magnitude greater than low-temperature deposited SiO_2 previously used in microfabricated cells. These films have been used in microfabricated fuel cells constructed on silicon integrated circuit wafers and tested. Their results show an improvement in performance over previous cells that used un-doped silicon dioxide. Additionally, cells with Nafion-on-PSG dual-layer membranes were fabricated and tested. These cells demonstrated improved current-voltage behavior under linear sweep voltammetry, but maintained their performance over several days.

10.1 Background

The main factor for proton conduction in glass appears to be the strength of O – H bonding. In silica glasses, the O – H bonding is typically strong, leading to a low mobility of H+, but in phospho-silicate glass, the O – H bonding is weak due to strong hydrogen bonding (33). In addition, the proton conductivity in phosphate glasses has been shown to be proportional to the square of the proton concentration (34). Studies of proton conduction has been made in a number of melt glasses of the form $MO \cdot P_2O_5$ (M = Be, Mg, Ca, Sr, Ba, etc.), in which small amounts of water in the form of – OH groups exist instead of alkali metal ions (35-36).

Phosphorous-doped SiO_2 films were deposited using a Unaxis PECVD system. The two gases for SiO_2 were nitrous oxide and silane. The doped films were made using a gas mixture of phosphine and silane with the nitrous oxide. A gas cylinder was obtained that had 5% silane with 0.3% phosphine with helium carrier gas to compliment the 5% silane in helium that was used for the regular glass films. The new gas line was connected to the PECVD system in addition to the other lines, enabling the use of silane and phosphine/silane together so that a range of phosphorous concentrations could be studied. Other process parameters that were adjusted included temperature, RF power, and ratio between the nitrous oxide and phosphine/silane flow rates.

10.2 Measurement of ionic conductivity

PSG films on the aluminum-coated substrates were measured for ionic conductivity through the use of impedance spectroscopy (IS). Figures 10.1 and 10.2 show the effect of two parameters, temperature and gas ratio, on the conductivity. The data for Figure 10.1 was from samples deposited at 100°C and 400 W power; with only gas flow rates changed. By decreasing the ratio of N_2O to PH_3/SiH_4 from the standard 2.25, the conductivity increased until the ratio is only 0.5. Below 0.5, the conductivity decreases. Though the conductivity was higher, films made with N_2O to PH_3/SiH_4 gas ratios less than one were not of very good quality and did not serve as a good encapsulating material for the microchannels without breaking.

Figure 10.2 shows that the conductivity of PSG was not as dependent upon deposition temperature as the original SiO_2 films. These films were deposited with the standard gas ratio of 2.25 and 400 W power. This provides good evidence that the conduction of ions through the PSG was improved due to the phosphorous and not just an

increase in silanol concentration with decreased temperature. Because of the low decomposition temperature of the PPC sacrificial polymer, 100°C continued to be used for the deposition of PSG in the fuel cell devices.

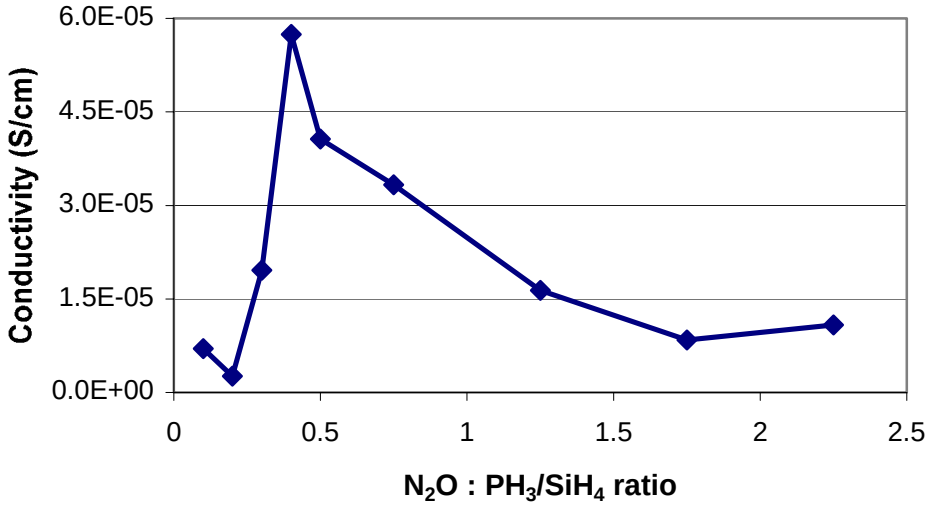

Figure 10.1: Conductivity of PSG films as a function of gas ratio

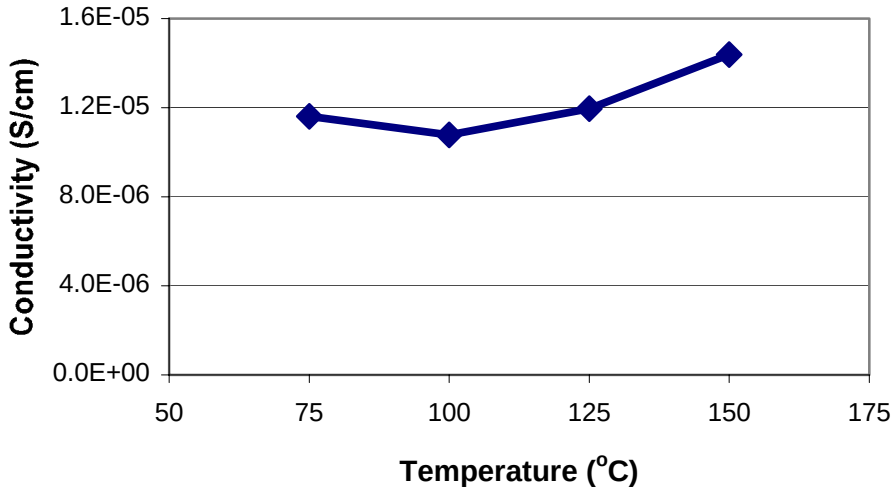

Figure 10.2: Conductivity of PSG films as a function of deposition temperature

10.3 XPS analysis of PSG films

The chemical composition (phosphorus concentration in the film) and local bonding environments of Si, O and P were studied with x-ray photo-electron spectroscopy (XPS). The thickness of the films deposited on bare Si substrates for XPS measurements was 2-3 μm. The XPS spectra were recorded using a Perkin Elmer XPS system (Model PHI 1600).

Figure 10.3 shows a typical XPS survey scan spectrum for a PSG film grown at 100°C. In addition to the expected Si, O and P peaks, small amounts of C and N were present as impurities, due presumably to cross-contamination of the deposition chamber. The overall chemical composition of the films was Si 29-30 at.%, O 69-70 at.%, and P 0.5-0.7 at.%. The Si/O ratio in the films was found to be nearly independent of the deposition temperature, while Figure 10.4 shows that the P concentration decreases with increased deposition temperature. The local bonding configurations of Si, P, and O were studied from their respective core level photo-electron peaks and are shown in Figure 10.5. The Si 2p peak in Figure 10.5 (a) can be seen to be fitted adequately with a single Gaussian peak centered at 103.6 eV, indicating that Si was present in the Si-O bonding only. The absence of a contribution at 99.3 eV confirms that no Si-Si bonding was present. The P 2p photo-electron peak in Figure 10.5 (b) can also be fitted adequately with a single Gaussian peak centered at 134.8 eV, again indicating that P was present in the P-O bonding only, and that P was indeed present in the substitutional state. The O 1s peak in Figure 10.5 (c) displays two components at 531.2 eV and 533.1 eV, corresponding to O-P and O-Si bonding, respectively. Consistent with this result, the relative fraction of the 531.2 eV component in the O peak that corresponds to the O-P

bonding was also found to be directly proportional to the P concentration in the film. Thus, the core level photo-electron spectra in Figure 10.5 show that the PSG films grown in this study are chemically homogeneous and maintain stoichiometry even at low deposition temperatures.

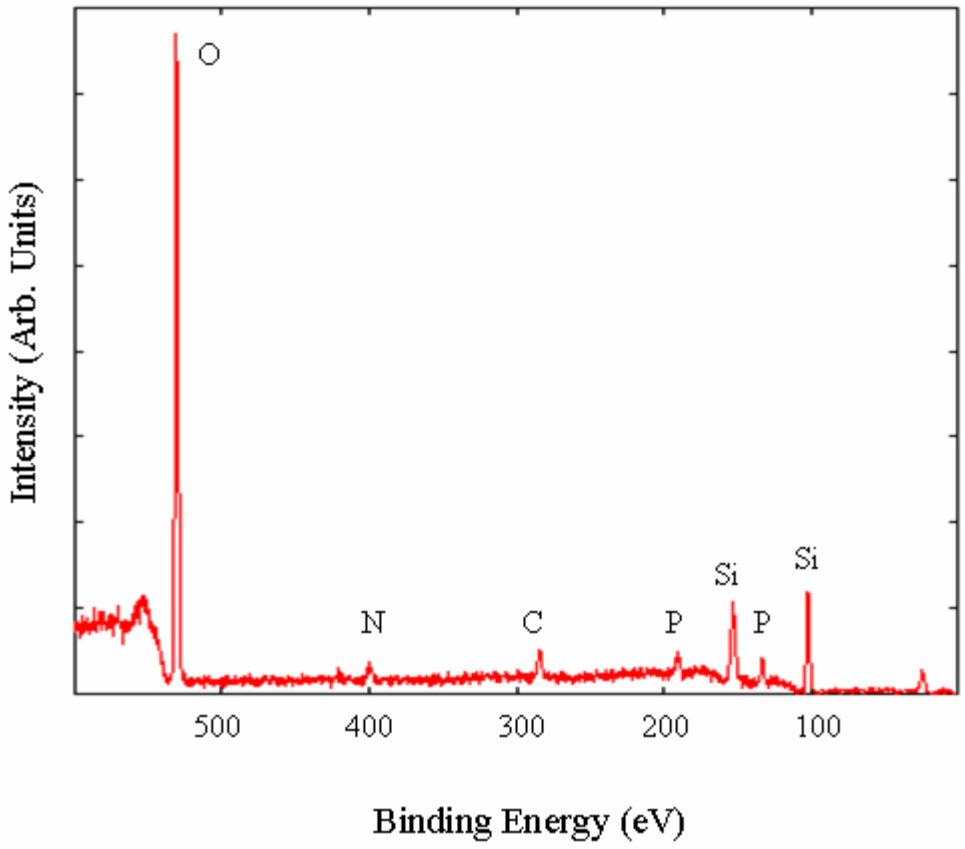

Figure 10.3: Typical XPS survey scan spectrum of PSG film

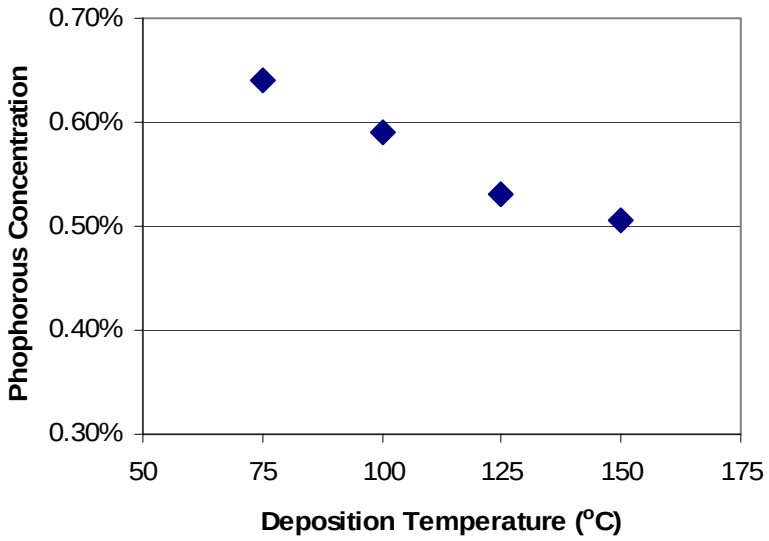

Figure 10.4: XPS measurement of phosphorous concentration in PSG films as a function of deposition temperature

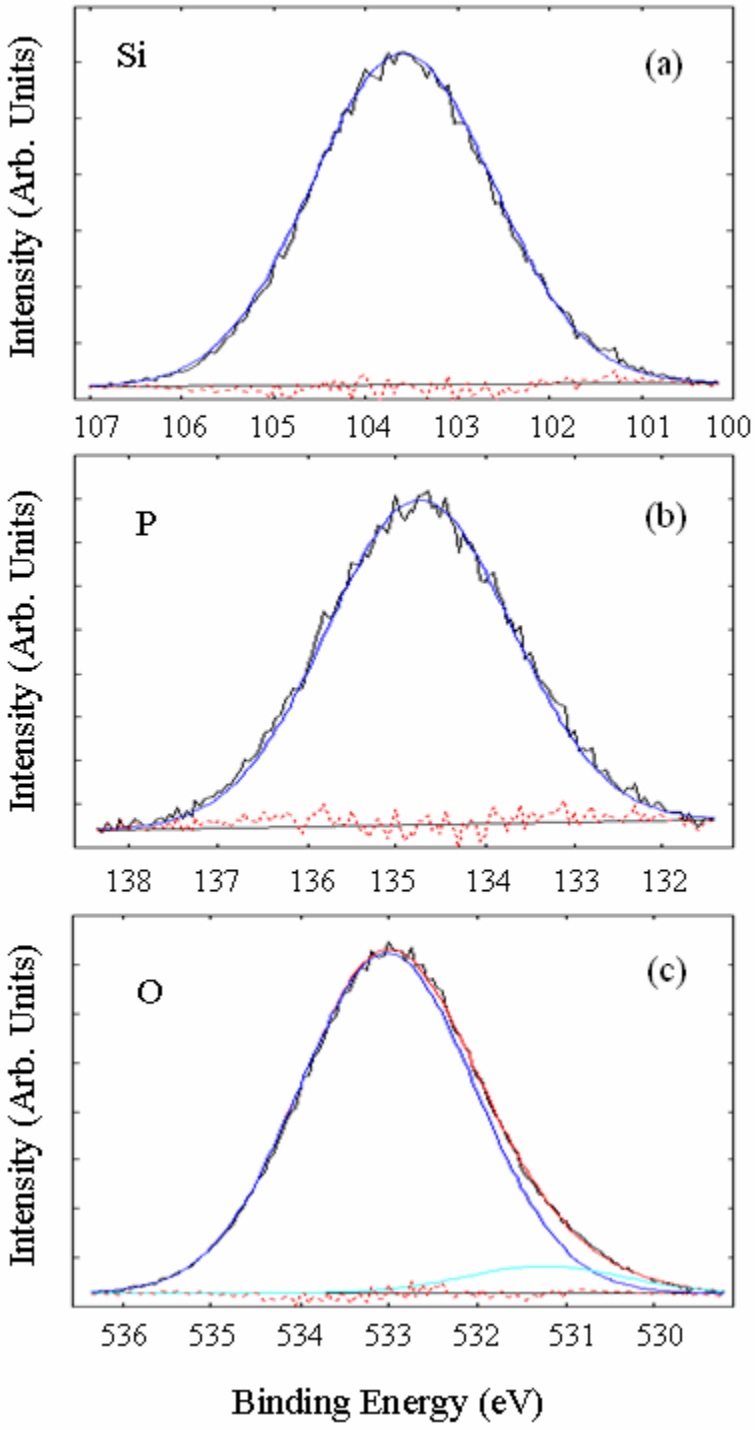

Figure 10.5: XPS scans of the local bonding configurations of Si (a), P (b), and O (c)

10.4 Use in micro fuel cells

Phosphorous-doped films were used as PEMs in microfabricated fuel cells to compare to the un-doped SiO_2. Again, the deposition temperature of the PECVD chamber was 100°C. Although, many different recipes were tested for ionic conductivity measurements, the mechanical strength of the films using some of the different gas ratios were not as good as the standard SiO_2 recipe. For this reason, the initial fuel cell devices with phosphorous doping used the standard recipe with only the phosphine-silane gas substituted for silane. These films, however, were still not as strong as the previous SiO_2 films and required a thicker deposition.

Microfabricated full cells were fabricated using the processes previously described and tested with linear sweep voltammetry at a scan rate of 1 mV/sec from the open-circuit potential. The thickness of the PSG membrane was shown to have a major effect on the performance of the cells. Figure 10.6 shows the room temperature polarization (top) and power (bottom) curves of two samples with different thicknesses of PSG. The gas ratio was 2.25, the deposition temperature was 100°C, and the power was 400 W. Humidified hydrogen with an inlet pressure of 1 psig was the fuel and the thick-film cathodes were air breathing. On each sample, a solid layer of approximately 100 $\mu g/cm^2$ of Pt/Ru was deposited on the bottom of the microchannels and 34 $\mu g/cm^2$ of Pt/Ru at the membrane surface. The first sample had 6.0 μm of PSG while the second had 9.0 μm. With the increase in resistance due to the thicker membrane, the current density decreases significantly.

Also shown in Figure 10.6 is the performance of a microfabricated fuel cell with Nafion-on-PSG dual-layer membrane. The fabrication of this device was similar to the 6

μm thick PSG device, except a 20 μm thick layer of Nafion was cast over the PSG layer prior to the cathode fabrication. The open-circuit potential and current density both improved, resulting in an approximate doubling of the peak power density. Additionally, the cells fabricated with the composite membranes have worked for a longer period of time.

In addition to improving the PEM characteristics, an important area of concentration continued to be the anode fabrication, specifically how to increase the catalyst loading while maintaining porosity for proton transport through the membrane. Figure 10.7 shows the polarization and power curves for a cell with the double layer catalyst. This sample was fabricated in parallel to the Nafion-on-PSG sample above, except that after the 34 $\mu g/cm^2$ Pt/Ru layer was deposited, approximately 750 Å of PSG was deposited, then followed by an additional 9 $\mu g/cm^2$ of Pt/Ru. The rest of the device fabrication continued with the 6.0 μm layer of PSG, 20 μm layer of Nafion, and Pt ink cathode. Even though, the increase in catalyst loading was very slight, the improvements in open-circuit potential and current density are very dramatic. The sweep rate used for this polarization curve was 1 mV/s. Figure 10.8 shows a series of 30-minute chronoamperommetry measurements for the cell operating on hydrogen at set potentials from 350 mV to 750 mV. The values obtained at each potential are very similar to the 1 mV/s linear sweep voltammetry scan. The activity of the embedded catalyst layers continue to be much better than those deposited directly onto the PPC sacrificial polymer prior to the PEM deposition because of the increase in catalyst/electrolyte contact area and PPC residue on the first layer, as previously discussed.

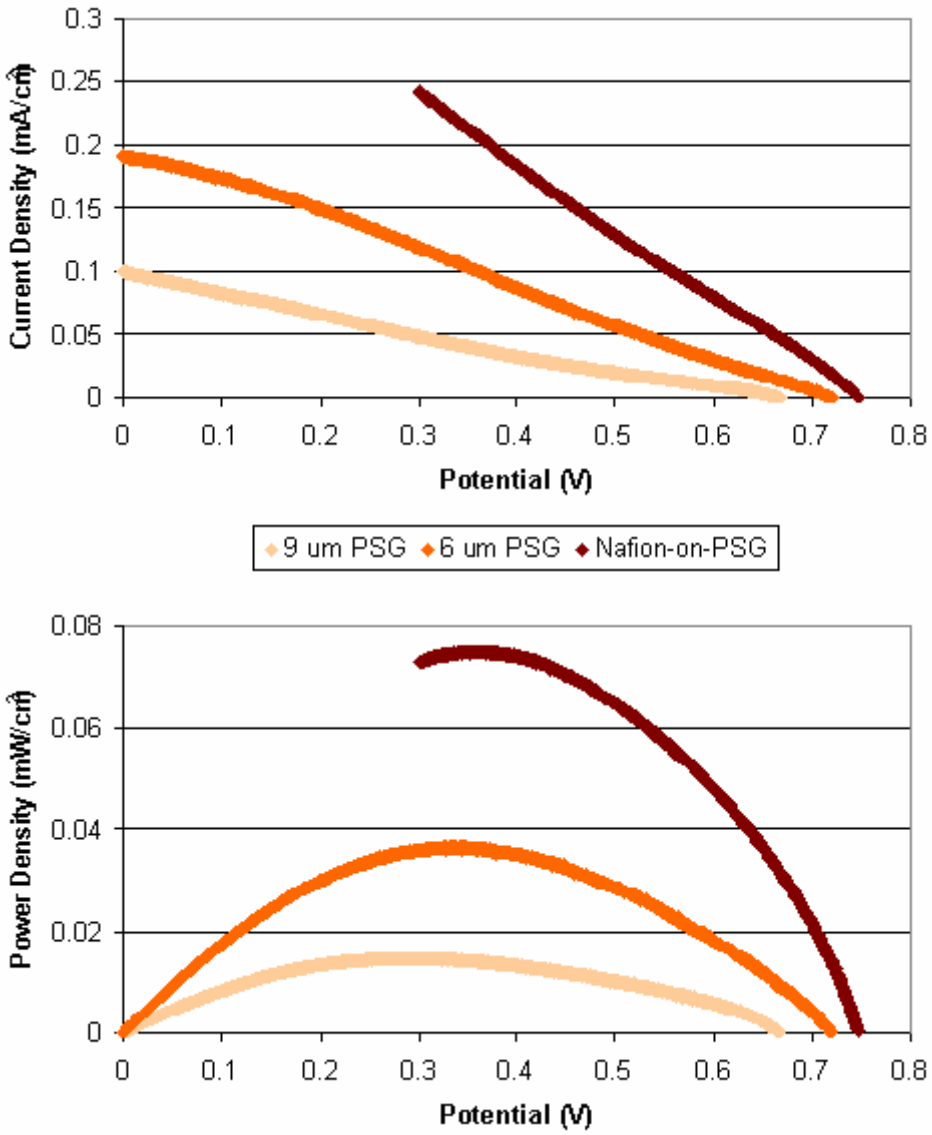

Figure 10.6: Polarization (top) and power (bottom) curves for microfabricated fuel cells featuring PSG membranes with thicknesses of 6.0 and 9.0 μm and a Nafion-on-PSG membrane

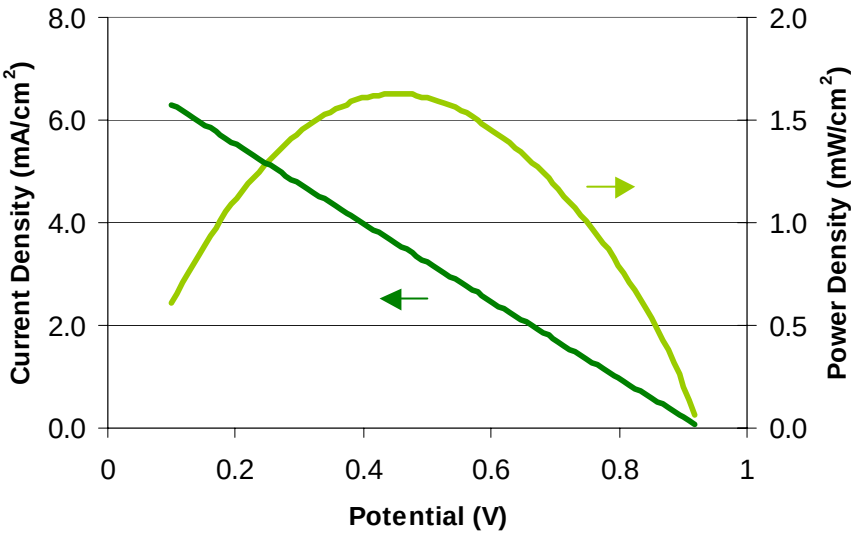

Figure 10.7: Polarization and power curves for microfabricated fuel cells with Nafion-on-PSG membranes featuring a double-layer of Pt/Ru anode catalyst

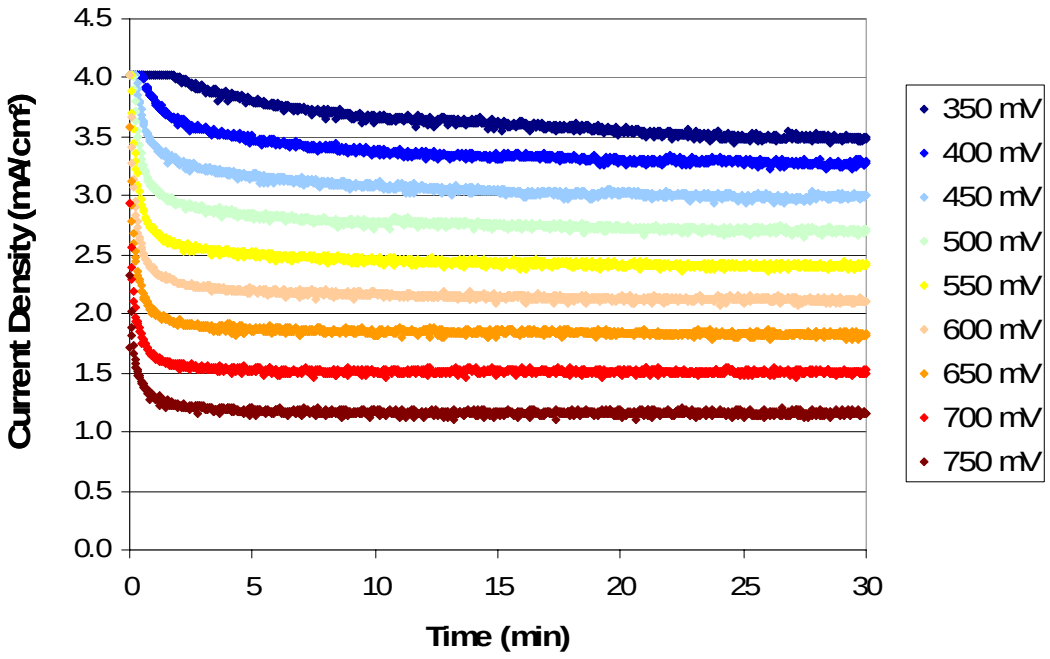

Figure 10.8: Current densities at constant potentials for Nafion-on-PSG fuel cell operating on humidified hydrogen

Figure 10.9 shows linear sweep voltammetry scans with different sweep rates. As the sweep rate increased, the currents obtained increased. This indicated that another factor was limiting performance besides the membrane characteristics or catalyst loading, i.e. mass transfer limitations. Because much of the hydrogen oxidation with this cell occurred at the catalyst embedded in the glass, the diffusion of hydrogen through the thin layer (750 A) of PSG limited the performance at slower sweep rates and steady-state conditions. For the very fast sweep rates, the mass transfer limitations were minimized and the slope of the current-voltage curve follows the resistance of the cell. The slope of current density versus voltage for the 200 mV/s scan indicated an area resistance of 62 Ω-cm^2. Based on the ionic conductivity measurements and the 6.0 μm thickness deposited in this cell, the area resistance for the PSG layer was calculated to be approximately 54 Ω-cm2. Therefore, the overall resistance of the cell closely matched the PSG resistance.

10.5 Long-term performance

In addition to improving the current voltage behavior, one of the main goals of using the Nafion-on-PSG composite PEMs was to improve the lifetime and reliability of these microfabricated fuel cells. Tests were performed on Nafion-on-PSG samples with both single and dual catalyst layers for a period of days to ensure that the device would continue to operate at the same level. Figure 10.10 shows the measured voltage as the single layer Pt/Ru cell was discharged across a 1 MΩ resistor and across a 236 kΩ resistor with an excess flow of humidified hydrogen with inlet pressure of 1 psig. For the two and half days across the higher resistance, a relatively constant voltage of 0.67 V was recorded, resulting in a current density of 0.037 mA/cm^2. It then was discharged across

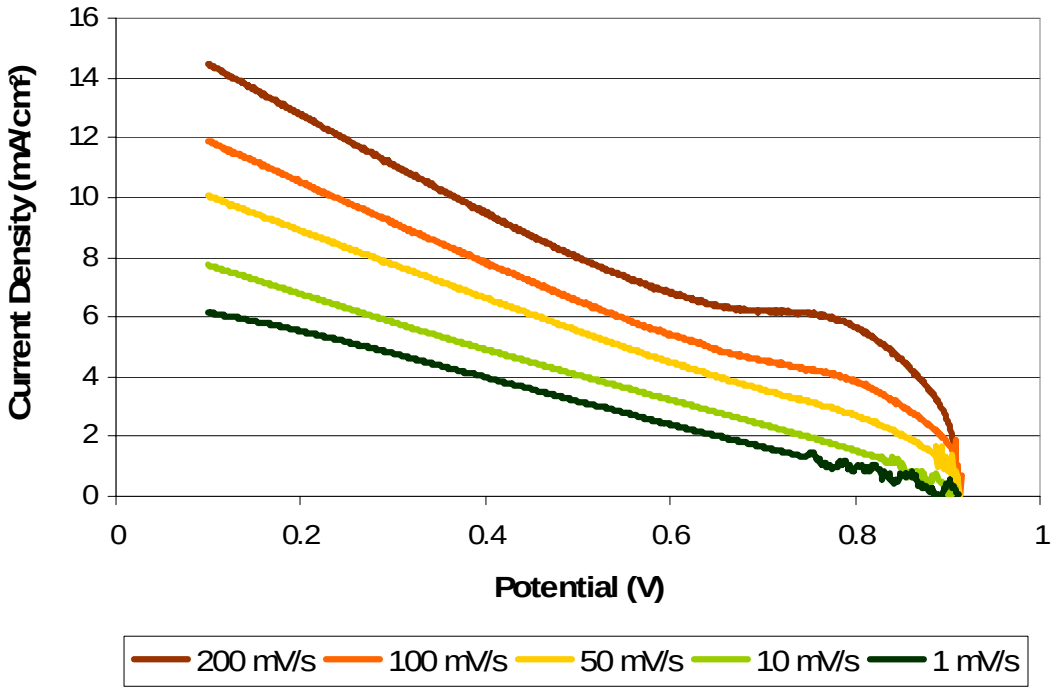

Figure 10.9: Linear sweep voltammetry results with different sweep rates for Nafion-on-PSG fuel cell operating on humidified hydrogen

the lower resistance for four days and showed a slight increase in voltage from a little over 0.4 V near the beginning of the run to about 0.5 V over days 3 and 4. The average current density was approximately 0.12 mA/cm^2, with an average power density of 53 $\mu W/cm^2$. These current and power densities maintained during the tests were about 30% lower than the values obtained from linear sweep voltammetry for the same device.

Similar tests were performed on the cell with the double Pt/Ru layer. Figure 10.11 shows the measured voltage of this cell discharged across a 236 kΩ resistor and across a 56 kΩ resistor operating on excess hydrogen with inlet pressure of 1 psig. Across the 236 kΩ resistance, the voltage increase to greater than 0.7 V, before dropping to about 0.67 V during the fourth day. The current density at this voltage was 0.095 mA/cm^2. It then was discharged across the lower resistance for six days and operated with an average voltage of approximately 0.4 V, resulting in current and densities of 0.24 mA/cm^2 and 95 $\mu W/cm^2$, respectively. While still greater than the single catalyst layer device, these values were dramatically lower than the data observed by linear sweep voltammetry. This provides further evidence that diffusion of hydrogen through the PSG was a limitation in the performance for the second layer of Pt/Ru. After removing the load at the end of each test, but continuing the flow of H_2, the open-circuit potential returned to about 1.0 V within a few minutes.

10.6 Fuel utilization

While the fuel cells have been shown to perform consistently with time for a steady flow of excess H_2 through the microchannels, the fuel utilization was extremely low for these tests. Most of the previous tests, including linear sweep voltammetry in the

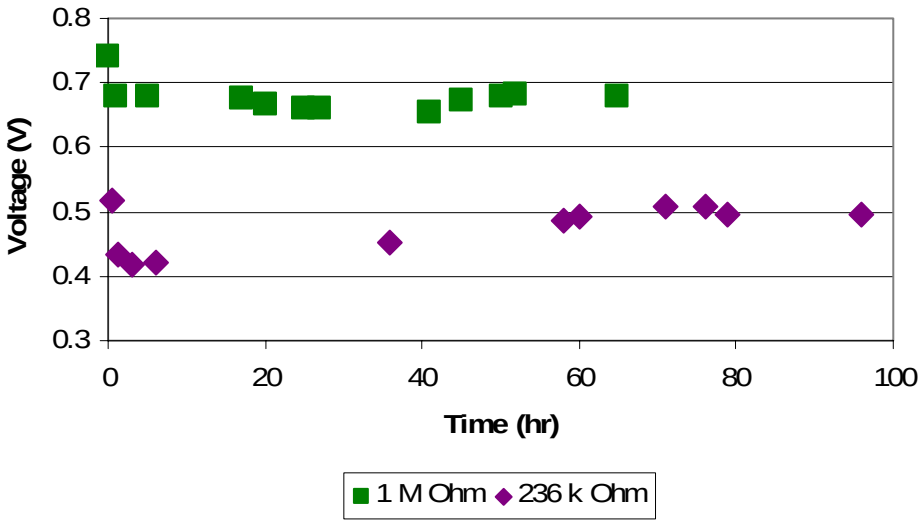

Figure 10.10: Measured voltages of single layer Pt/Ru, Nafion-on-PSG fuel cell discharged under constant load resistance

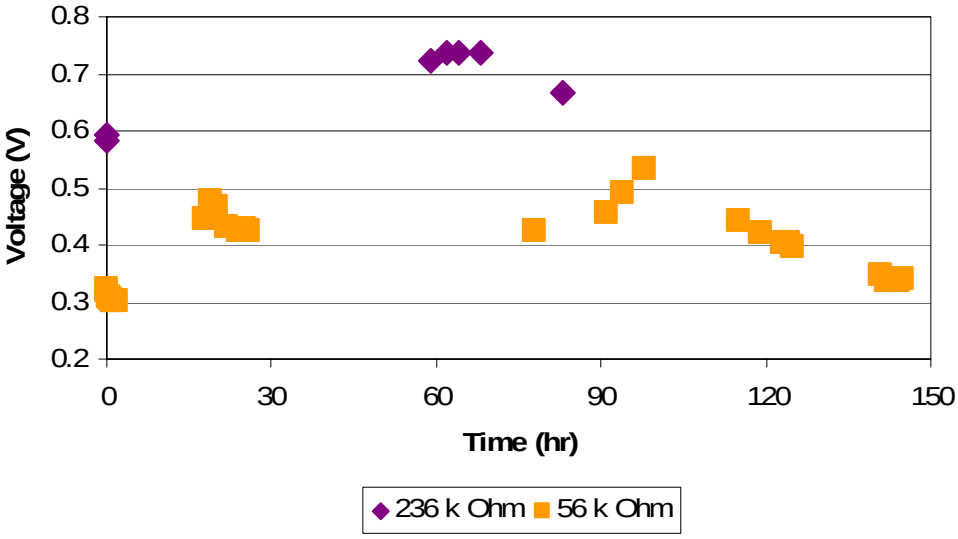

Figure 10.11: Measured voltages of dual layer Pt/Ru, Nafion-on-PSG fuel cell discharged under constant load resistance

previous chapters and the long-term tests shown in Figures 10.10 and 10.11, operated on hydrogen that entered the microchannels with an inlet pressure of 1.0 psig and exited to the atmosphere. The amount of fuel consumed at the anode for even the best cells was less that 1% of the total that passed through the channels. For the microchannel dimensions used and the amount of current produced, it would not be best to use a flow of hydrogen with an exit hole.

A more realistic design for H_2 fuel cells would be to not have an exit since there are no by-products produced at the anode. With a properly sealed system, the only means of hydrogen loss other than through its reaction at the anode would be diffusion across the PEM or through the walls of the fuel storage area.

In order to test how much hydrogen would react without an exit, the tubing connected to the outlet hole was plugged with epoxy. Hydrogen was allowed to fill the microchannel and all tubing at a charged pressure of 3 psig. A valve placed between the hydrogen source and the pressure transducer in the line was shut, limiting the hydrogen available to the fuel cell to what was already in the system. The total volume of this system, including the tubing and void volume of two valves and the pressure transducer was calculated to be 0.418 mL. At 3 psig, or 17.7 psia, the total amount of hydrogen was calculated at 2.23×10^{-5} moles, which if fully reacted could produce 4.31 C of charge. The theoretical energy available was 5.17 J, assuming the reaction occurred at 1.2 V.

Again the 56 kΩ resistor was used as the load and the potential was measured by the potentiostat throughout the length of the experiment. Figure 10.12 shows the current measurements with time. Also plotted is the total Coulombs passed as the fuel cell discharged. After almost a full week had passed, approximately 53% of the available

hydrogen had been used. The pressure gauge was monitored during the test and the recorded values are plotted in Figure 10.13. The pressure at the end point of the experiment was -8.5 psig, or 6.2 psia, and was maintained in the system after the run was stopped for over two hours before the system was vented. The fact that the pressure actually fell well below atmosphere conditions as hydrogen was consumed and did not change after the run indicated that the system was sealed very well. It also indicates that even though the voltage had fallen to 0.1 V and the experiment was stopped, hydrogen remained in the system. If the difference in starting and ending pressures are used to calculate the loss in hydrogen instead of the total initial pressure, then the fuel utilization was approximately 82%.

Figure 10.14 shows the power output with time. The total energy converted vs. time shows that the overall efficiency was only 12.4% for the entire amount of hydrogen, or 19.2% using the value calculated from the pressure loss. Again, the overall efficiency is highly dependent upon the operating voltage as well as fuel utilization. The low efficiency was due mainly to the fact that as the voltage dropped, the energy from the reactions that was successfully converted into electrical energy also dropped.

Another important result demonstrated by this test was the performance of the device as a function of the hydrogen pressure at the anode. A comparison of the current and pressure data with time show that the cell needs to be operated with a hydrogen pressure greater than one atmosphere to produce higher power densities. Also, for practical usage, the devices must be able to operate at consistent current and voltage levels. For an operating device, a minimum operating voltage and current must be maintained. Values greater than these set minimums would be wasted energy, while any

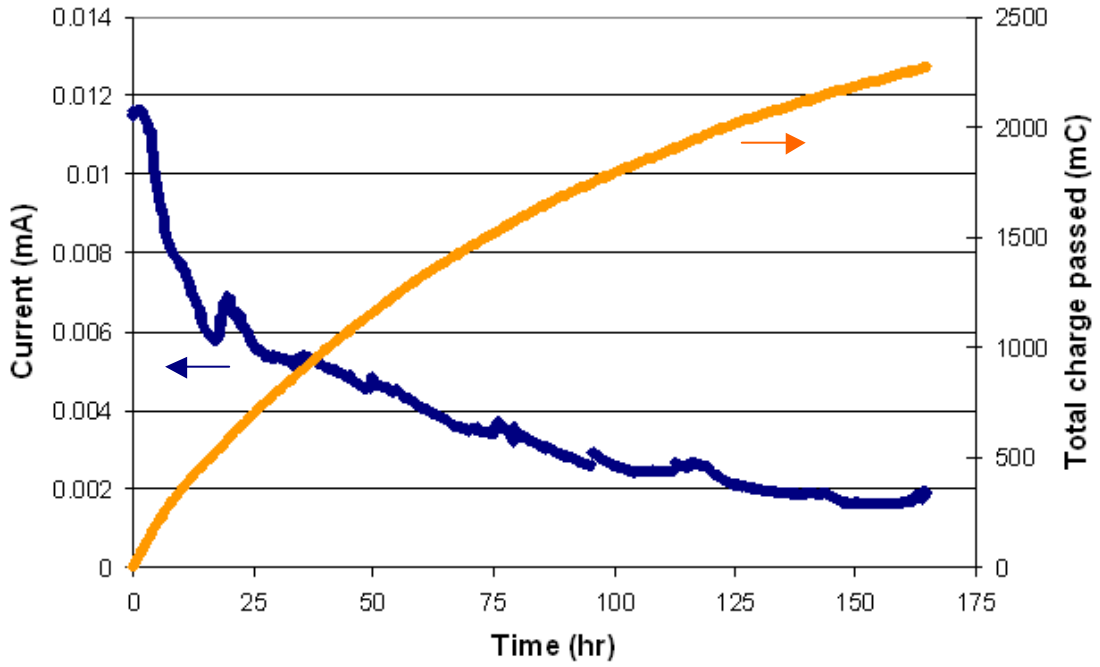

Figure 10.12: Current and total charge passed with time for a microfabricated fuel cell operating on a limited supply of hydrogen

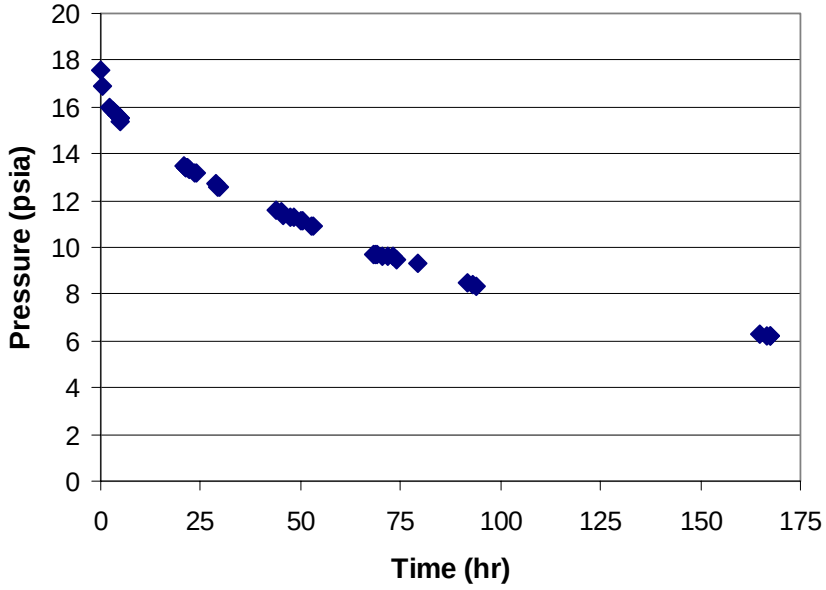

Figure 10.13: Pressure data for a microfabricated fuel cell operating on a limited supply of hydrogen

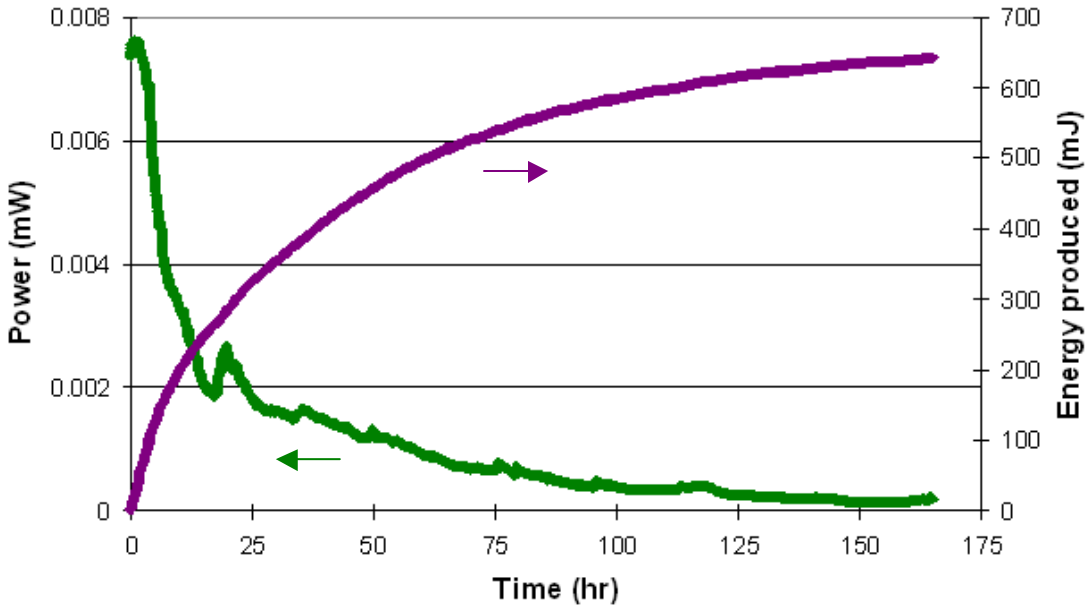

Figure 10.14: Power and total energy converted with time for a microfabricated fuel cell operating on a limited supply of hydrogen

power produced at lower voltage or current values would not properly operate the electrical device for which the fuel cell was designed. The important factor for any hydrogen fuel storage device would be the ability to not only deliver the fuel, but maintain the pressure at the anode throughout the fuel usage. With high fuel utilization, the overall efficiency would be determined chiefly by the operating voltage. For instance, if over 90% of the fuel was consumed at a consistent 0.6 V, the overall efficiency would be greater than 45%.

To test the fuel utilization of the micro fuel cells operating under a constant hydrogen pressure, the testing setup was changed so that water could be used to displace a given amount of hydrogen in the system. After the system was filled with humidified hydrogen to a desired pressure, a switching valve changed the inlet from the gas tank to a syringe pump. The syringe pump then pushed water at a known flow rate to maintain the pressure while hydrogen was consumed.

Figure 10.15 shows the fuel cell's current with time for a hydrogen pressure of 2.1 psig. With constant pressure, the current was much more consistent than with a falling pressure. The pressure was maintained over the course of the experiment by pushing water from the syringe pump at a rate of 8 μL/hr, resulting in a total displacement of 0.1333 mL. This volume and pressure of hydrogen should produce 1313 mC of charge. With 385 mC of charge passed during the run, the fuel utilization was approximately 30%.

With the added complexity of the experimental setup, there was a greater chance that a small leak may have been present during this experiment, resulting in the decreased

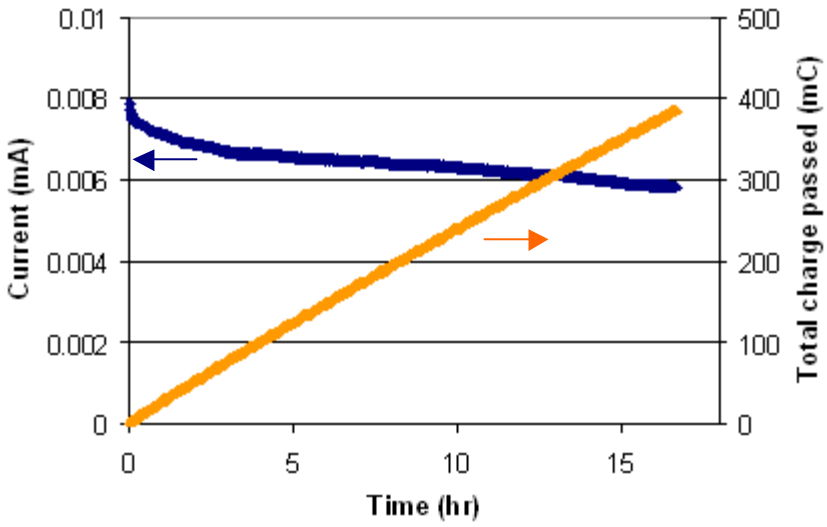

Figure 10.15: Current and total charge passed with time for a microfabricated fuel cell operating at a maintained pressure of 2.1 psig

fuel utilization. After the syringe pump and fuel cell operation had been stopped, the setup was not disturbed and the pressure gauge was monitored. In two hours, the pressure fell from 2.1 to 1.9 psig, indicating that hydrogen was escaping with a leakage rate of approximately 3 μL/hr, which would have resulted in losing approximately 0.051 mL of hydrogen during the experiment. Subtracting this value for lost hydrogen from the total volume displaced results in a fuel utilization of 47.5%.

10.7 Operation with methanol

Nafion-on-PSG fuel cells were also tested with methanol fuel at room temperature. Among the variables tested were the effects of methanol concentration and fuel flowrate. The fuel cell used in the following experiments was similarly constructed as the hydrogen cell above, including the double layer of Pt/Ru catalyst at the anode.

Figure 10.16 shows a series of linear sweep voltammetry measurements for methanol with different sweep rates. The fuel concentration was 1.0 M and flowrate was 0.1 mL/hr. The scans began at the open-circuit potential and moved to 0.1 V. With increasing sweep rate, the current density increased, indicating that mass transfer effects limited the performance, namely the diffusion of methanol into the PSG and to the embedded Pt/Ru layer. For the 100 mV/s sweep rate linear voltammetry, the diffusion effects are minimized to better evaluate the effect on the current-voltage behavior from the membrane resistance. Based on the slope of the current density vs. potential, the area resistance of the cell was 75 Ω-cm^2. This value was close to the calculated value of 54 Ω-cm^2 from the ionic conductivity measurements that, as with hydrogen, the overall cell resistance was dominated by the resistance of the PSG portion of the PEM. While the

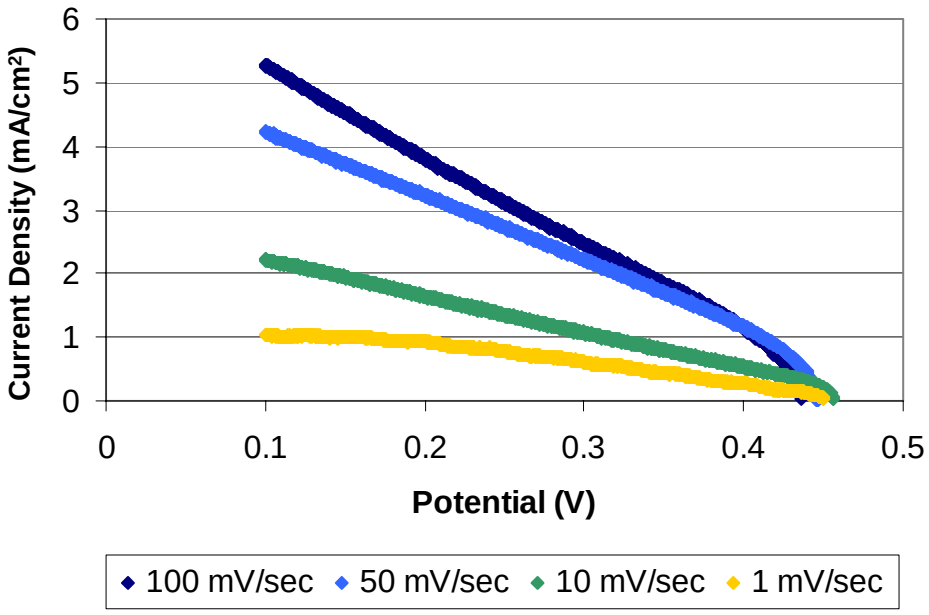

Figure 10.16: Linear sweep voltammetry scans for Nafion-on-PSG fuel cell operating on 1.0 M methanol

slope of the polarization curve was similar, the open-circuit potential was lower than when operating on hydrogen, resulting in lower power densities.

Figure 10.17 shows linear sweep voltammetry measurements for methanol concentrations from 1.0 to 8.0 M. The open-circuit potential decreased slightly with increasing concentration. This indicates that there was some methanol crossover through the dual-layer PEM. With the 100 mV/s sweep rate, the slope of the polarization curve did not change significantly with increasing concentration. With the 1 mV/s sweep rate, the current density increased with increasing concentration, indicating that methanol diffusion to the embedded Pt/Ru was the limiting factor in device performance at the slower sweep rates, as well as steady-state conditions.

Figure 10.18 shows chronoamperommetry measurements for 1.0 M methanol with a flowrate of 0.1 mL/hr at different potentials. The values at 10 minutes are relatively close to those obtained with 1 mV/s linear sweep voltammetry, but it can be seen that for higher current densities, the time to reach a constant current takes slightly longer. A similar series of chronoamperommetry measurements were performed on the cell at flowrates from 0.2 μL/hr to 1.0 mL/hr. The results, shown in Figure 10.19, did not demonstrate a dependence on the flowrate in this range, as even 0.2 μL/hr delivered an excess of methanol for the currents obtained. Figure 10.20 shows the current density of the cell over the course of 12 hours held at a constant potential of 250 mV and supplied with 1.0 M methanol at a flow rate of 0.2 μL/hr. The cell produced a consistent current density of 0.4 mA/cm^2. While the flow rate was the slowest that could be set with the equipment used, it still resulted in a fuel utilization of only 11.2%.

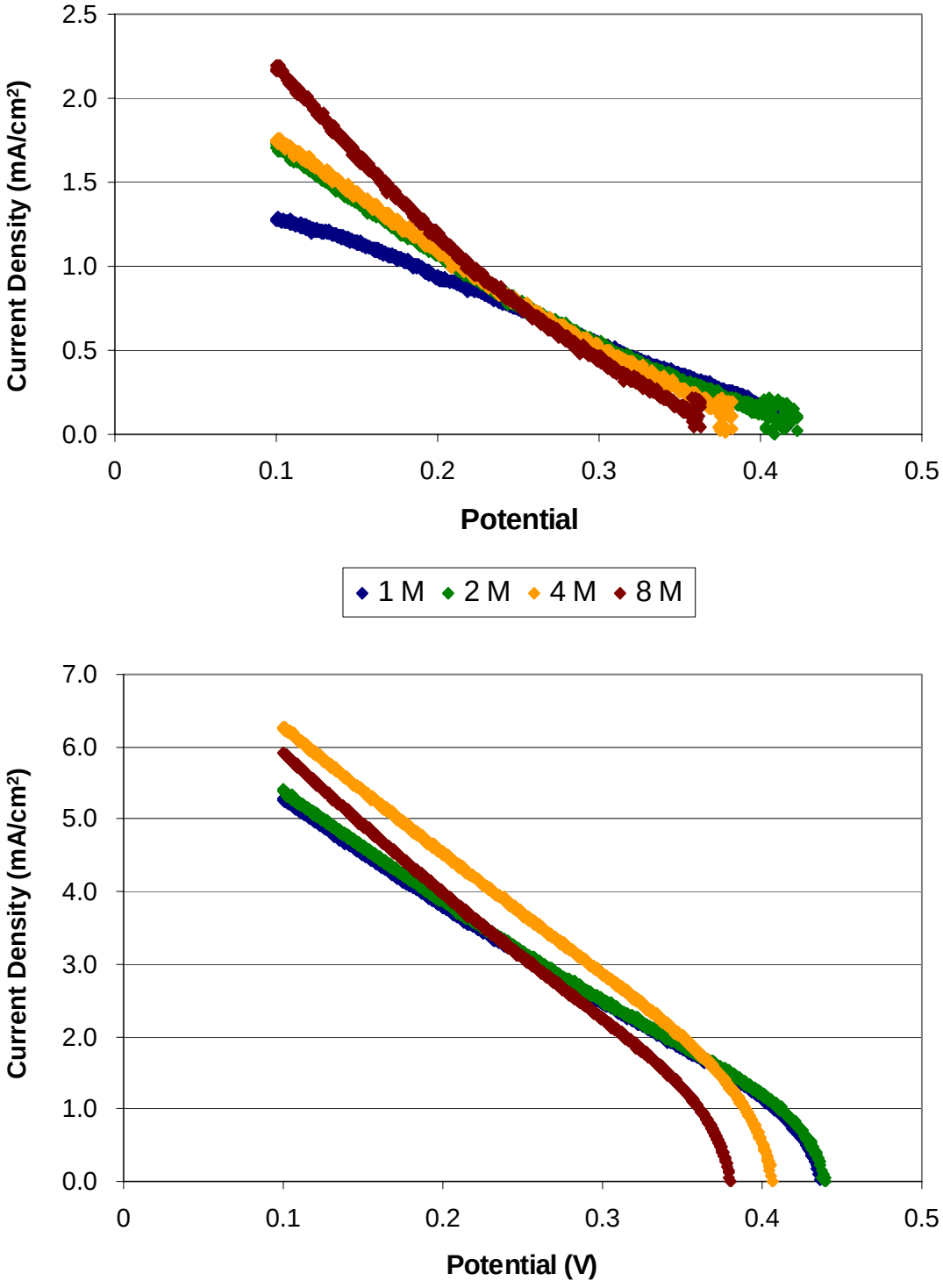

Figure 10.17: Linear Sweep Voltammetry scans for different concentrations of methanol with sweep rates of 1 mV/sec (top) and 100 mV/sec (bottom)

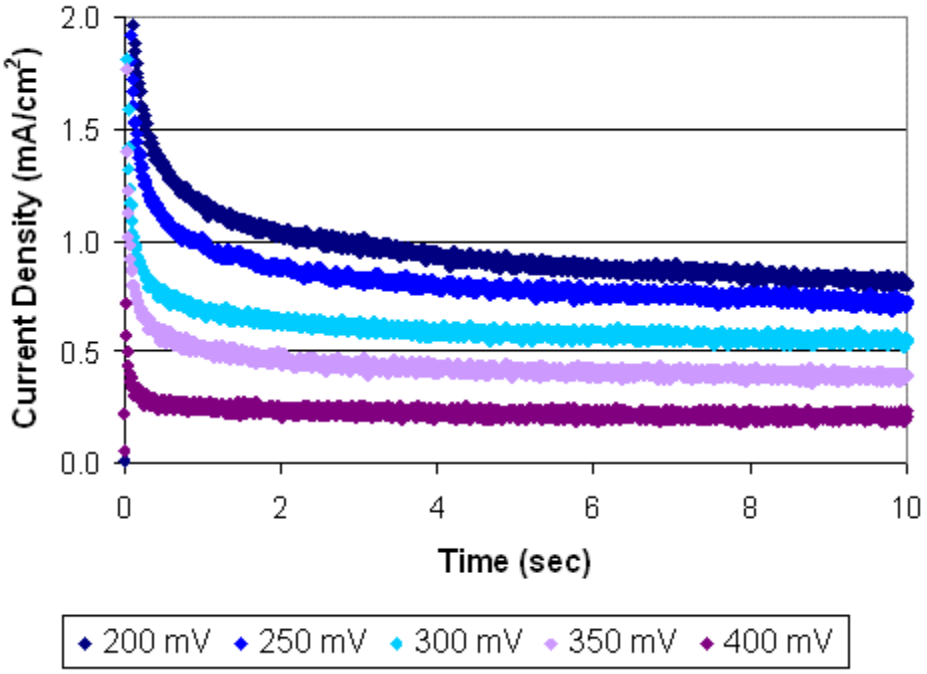

Figure 10.18: Current densities at constant potentials for Nafion-on-PSG fuel cell operating on 1.0 M methanol at 0.1 mL/hr flowrate

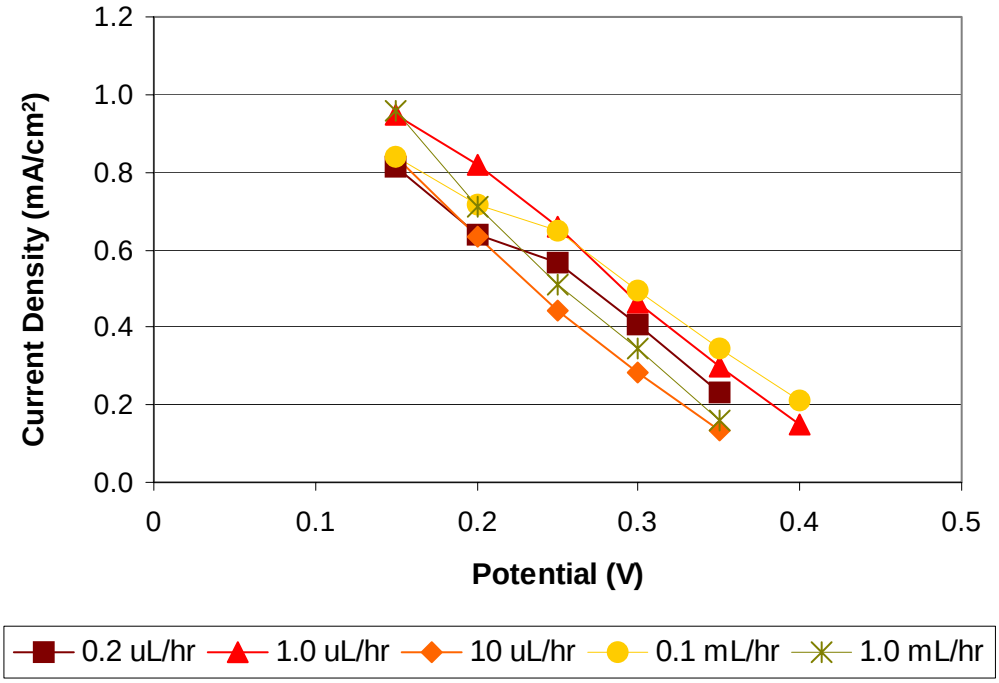

Figure 10.19: Current density at time=10 minutes vs. voltage for fuel cells operating on 1.0 M methanol with different flowrates

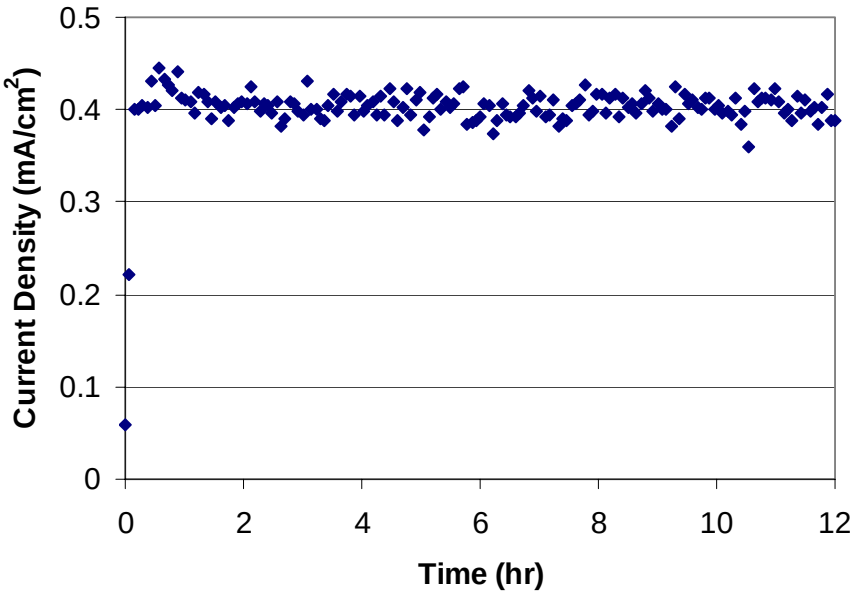

Figure 10. 20: Current density at 250 mV of Nafion-on-PSG fuel cell operating at room temperature on 1.0 M methanol with a flowrate of 0.2 μL/hr

10.8 Conclusions

The addition of phosphorous to SiO_2 has been shown to increase the ionic conductivity of the films and improve the overall performance of microfabricated fuel cells when used as the PEM. The conductivity of PSG films deposited under the same process conditions as the previously used SiO_2 membranes, except the addition of the phosphine gas, was approximately 50 times greater than the un-doped low-temperature SiO_2. Due to this increase in conductivity, thicker PEM layers could be deposited to improve the mechanical strength of the devices while still having a lower resistance to proton transport. The thicker films also improved the open-circuit potential, leading to better overall performance.

Casting a layer of Nafion on the PSG to form a dual-layer PEM further improves the overall device performance, particularly the long-term reliability. Using two layers of catalyst separated by an ultra-thin layer of the PSG electrolyte showed a dramatic increase in the device performance. Because of the increased catalyst/electrolyte contact area and cleaner surface, most of the hydrogen oxidation took place at the second, PSG-embedded layer of Pt/Ru, leading to hydrogen diffusion limiting the performance with increased current densities.

Continued efforts with the anode catalyst loading and Nafion-on-PSG composite membranes should further improve the performance. Of particular interest will be increasing the number of Pt/Ru catalyst layers and optimizing the amount of PSG deposited between these successive Pt/Ru layers. Optimizing the PSG deposition recipe for increased ionic conductivity as well as making thinner films can further reduce the overall resistance of the membranes.

Another very important area of improvement demonstrated with the Nafion-on-PSG fuel cells was the long-term reliability. One cell was used for a multitude of tests over the course of approximately two months. These tests not only showed consistent performance over time, but concentrated on the utilization of supplied hydrogen fuel. A well-sealed, closed system demonstrated over 80% fuel utilization based on the change in hydrogen pressure.

Methanol results with the Nafion-on-PSG cells were better than those obtained from the un-doped SiO_2. The improved anode was very important as the key parameter that limited the performance was the diffusion of methanol in PSG. Its crossover through the PSG membrane determined the open-circuit potential, while the rate of methanol diffusion though the very thin PSG layer that was used to embed the catalyst determined the currents at lower potentials.

CHAPTER 11

ADVANCED DESIGN AND FABRICATION

11.1 Introduction

Through Chapter 10, the discussion has been based on work performed with the design and fabrication of the micro fuel cells as described in the fabrication chapter. These devices featured straight channels built up from the silicon substrate with a patterned sacrificial polymer. Tubes were attached on the top of the channels using the plastic molded connectors. While test devices were successfully fabricated and tested, leading to a wealth of information on the materials and processes used and their effect on performance, this simplistic design has drawbacks. These shortcomings would be particularly problematic as the size, or active area, of the devices is scaled up to provide more power. Among the weaknesses that can be addressed with a new design are:

- Photo-patterning of polypropylene carbonate,
- Topside tube attachment,
- Non-planar, fragile membrane,
- Size limitation, and
- Matching of fuel usage with power

Polypropylene carbonate offered many advantages over previous sacrificial polymers, including a lower decomposition temperature and the ability to be directly patterned with ultraviolet exposure through a mask, similar to a photoresist, thus reducing necessary equipment and time. The thermal patterning process, however, did not produce as sharp features as polymer patterns made by reactive ion etching. While slope

sidewalls were considered positive for these structures, the loss of feature height, specifically the loss in height being dependent upon the feature width, necessitated that the channel structures have a very simple design. Changes in width of channels, corners and branching of channels all caused the features to have variable heights and differences in width between the mask and final patterns.

Attaching tubes to the top of the microchannels serves its purpose for fuel delivery to test devices, but was not considered the long-term, or final, method. Bringing the fuel from the back, or opposite side, of the wafer was considered the preferred option because the air-breathing cathode must be on the top, or fuel cell side, of the wafer. Also, because the test devices were so small, the amount of useable area covered up by the tubing and tube connector, up to 30% of the microchannels' length, was significant.

Because SiO_2 ended up being used as the thin-film PEM, or as part of a composite membrane, these devices were very fragile. They seemed to be most susceptible to breaking or cracking at the points of highest stress on the glass. This was at the side edges of the microchannels. The oxide must form a corner between the flat underlying substrate and the wall of the microchannel. In addition, this would also be a point of additional stress during heating because of differences in the polymer's and underlying substrate's coefficients of thermal expansion (CTE).

For these reasons, the sizes of the test devices have been limited to the dimensions of a single microchannel, up to 300 μm width and 1.5 cm in length. Reasonable sizes for devices that would actually power simple circuits are between 1 and 2 cm^2 with an active area of at least 50%.

Finally, the amount of hydrogen passing through the channels was significantly greater than the amount that reacted. Increasing the size and using serpentine channels with a much longer length would slow the pressure-driven flow significantly. Combining this with the increase in fuel usage from the larger area could greatly increase the fuel utilization and overall efficiency as long as the performance (current density and operating voltage) remained the same.

To overcome these shortcomings in a new, larger generation of prototype, a change in the design and processing was necessary. This new design features a thicker anode current collector made through electroplating gold and backside holes. The processes, advantages, and some early results are presented here.

11.2 Electroplate Gold Wall Design

The requirements of the new design were to be bigger (more active area), yet more structurally stable. The prototypes have been fabricated by sputtering the anode current collector and patterning the sacrificial polymer (through RIE or photo-patterning) into the shape of the fuel delivery microchannels. The new process sequence has the gold current collectors electroplated much taller (20 μm) than the sputtered layers, allowing them to also serve as microchannel walls. The sacrificial polymer is then filled into the spaces between the gold walls and polished to make a smooth surface. The catalyst layer is sputtered, followed by the deposition of the overcoat/membrane. Figures 11.1 and 11.2 show schematic illustrations of the two process designs. The deposited proton exchange membrane (PEM) in the new design has a more planar structure across the fuel cell without sharp corners to conformally cover. These corners have been the point of breaking or cracking in the SiO_2 films due to stress.

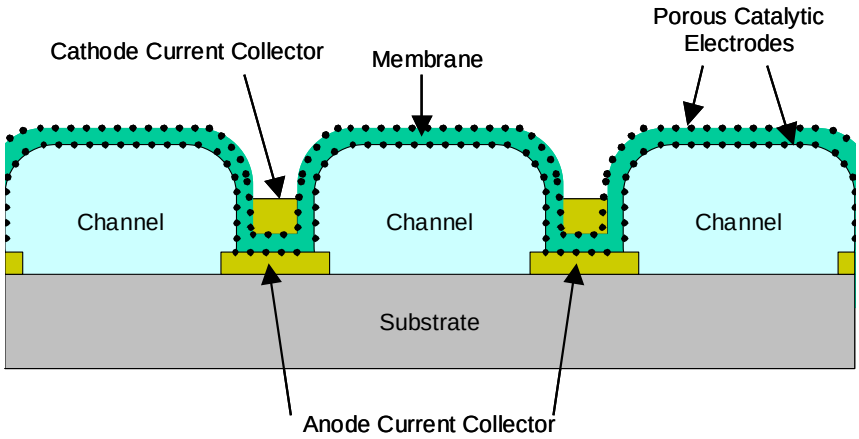

Figure 11.1: Schematic of micro fuel cell with patterned microchannels

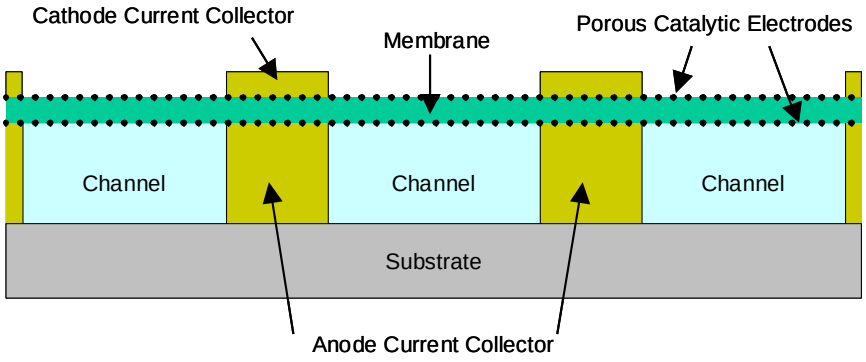

Figure 11.2: Schematic of micro fuel cell with electroplated gold wall microchannels

Figure 11.3 shows pictures of microchannels fabricated with electroplated gold walls and filled with polypropylene carbonate (PPC). The process of filling electroplated gold walls with PPC and polishing to a smooth surface for deposition of the overcoat has worked well.

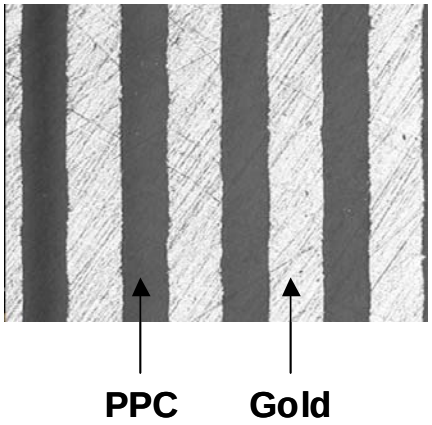

(a)

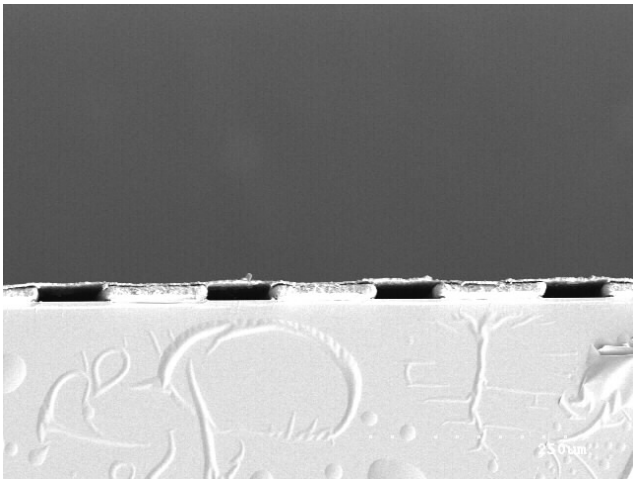

(b)

Figure 11.3: Filled PPC and gold walls after polishing (a) and SiO_2 coated microchannels formed by PPC decomposition (b)

11.3 Electrochemical Results

Figure 11.4 shows the polarization and power curves for a micro fuel cell with serpentine channels formed by electroplating gold and filling with the sacrificial polymer. The anode catalyst was a single layer of sputtered Pt with a loading of 64 μg/cm^2 and the membrane was a 6.0 μm thick layer of phosphorous-doped SiO_2 (PSG) deposited at 100°C. The increased catalyst loading improved the performance of this cell with respect to the ones with sputtered Pt/Ru.

The channels were 100 μm wide, 26 μm tall, and the fuel traveled the length of 3 channel segments of the serpentine design for a total length of 3.3 cm. There was an exit hole for excess fuel to escape. Due to the narrower channels, the active area was only about 50% greater than the single, 300 μm wide channels with 0.7 cm of active length. The different shape, however, caused the flow to be about six times less than before. The resulting fuel utilization and overall efficiency at 0.3 V were 0.26 % and 0.065 %, respectively. These numbers, while still very low, do represent a significant improvement over the previous results for cells with fuel exit holes. Continuing to increase the active area and length of the channels should continue to improve these numbers until the flow rate and power output are adequately matched.

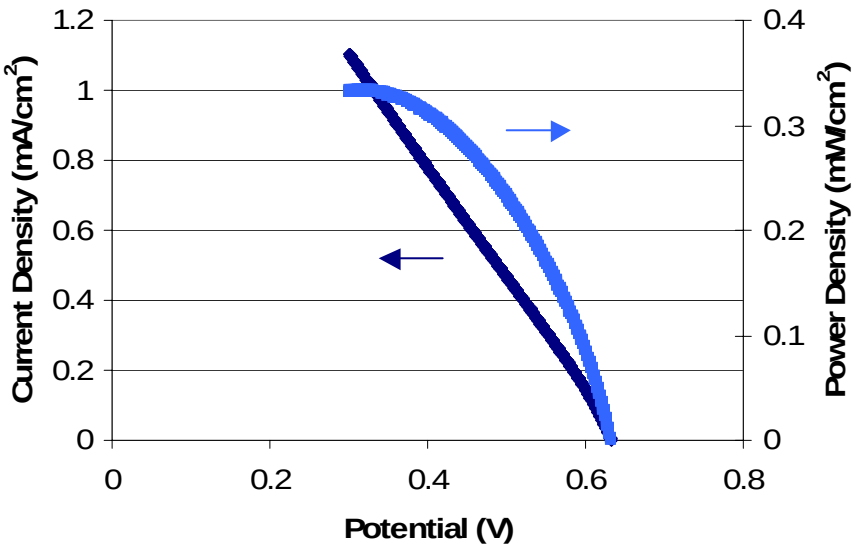

Figure 11.4: Polarization (navy) and power (blue) curves for a serpentine channel fuel cell

11.4 Backside hole fuel delivery

Another goal accomplished was the successful delivery of fuel to the microchannels from the backside of the wafer. This is an important feature of the final prototype because of the integration of the microfabricated fuel cell with the micro valve and fuel delivery pump. It is also important because it keeps the fuel inlet and outlet separated from the cathode, thus reducing the risk of methanol mixing with air and causing a mixed potential at the cathode.

Figure 11.5 shows a microscope image of an air channel formed over a hole through the silicon substrate. After trying different techniques, one process has been shown to reliably work. The steps are as follows: deposit a layer of silicon dioxide, approximately 2 μm thick, through plasma enhanced chemical vapor deposition (PECVD), spin and pattern a layer of photoresist on the back side of the wafer, use deep silicon etching to put a hole through the substrate to the deposited SiO_2, perform the fabrication steps on the front of the wafer using the SiO_2 as a "window" over the hole that provides support for materials to be deposited and a way to see the hole for proper alignment to pattern the microchannels.

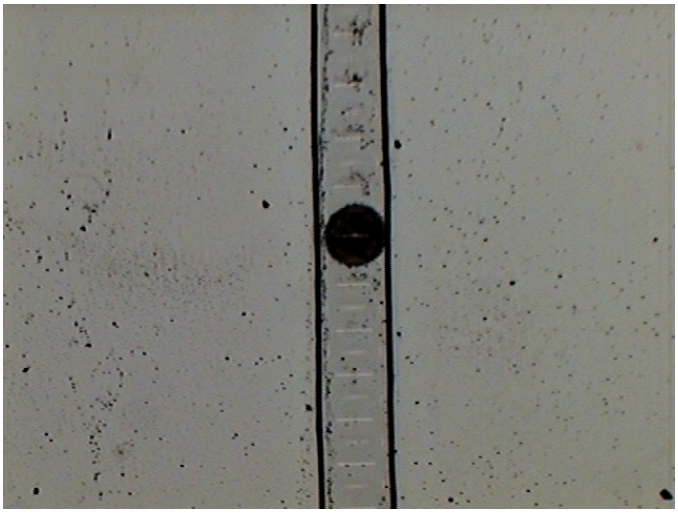

Figure 11.5: Microchannel fabricated over a fuel delivery through-hole

11.5 Summary

The ideas for advances in fabrication and design for larger fuel cells are presented here to illustrate the direction this work could follow in the future. Using the materials developed and described in previous chapters, larger fuel cell prototypes could provide a suitable power source for simple integrated circuits. An early prototype made with electroplated walls produced similar voltage and current densities to a smaller device fabricated with similar membrane and catalyst properties, resulting in greater power. The decreased flow rate due to the longer, serpentine channel further improved the fuel utilization and total efficiency. Continued increase in size, particularly the length of microchannels, will most likely be the key to matching power output to fuel flow.

CHAPTER 12

FINAL SUMMARY

12.1 Summary of work

This project began not only as a search for a micro power source, but also as a demonstration of air-gap technology using sacrificial polymers. Therefore, much of the early work centered on the fabrication of microchannels, including the sizing and ways to get fluid into the miniature structures. Functionalized polynorbonene (PNB) was initially used with polyimide encapsulating materials to fabricate microchannels to be tested for fluid flow. Different versions of polyimide were tested to find the one(s) that would have the mechanical properties to serve as the channel structure after PNB decomposition without collapsing or cracking. A method for tube attachment to the inlet hole was developed. A testing setup was put together that included the fluid source and a gauge to measure the pressure of the fluid close to entering the microchannels.

One of the areas of greatest concentration was the search for materials better suited for the micro fuel cell fabrication and getting them to work adequately. PNB's decomposition temperature of 425°C was considered too high because of some of the potential PEM materials that were to be studied. The use of polycarbonates with decomposition temperatures around 200°C was preferred, but led to other problems. Both polycyclohexane carbonate (PCC) and polypropylene carbonate (PPC) dissolve in a greater amount of solvents, including NMP, the solvent used for polyimide solutions. This problem led to the use of silicon dioxide, which had to be deposited at low temperatures to avoid the premature decomposition of the polycarbonates. While initially thought of as a possible solvent barrier between two polymer layers, the conductivity of

low-temperature PECVD SiO_2 proved high enough to be used as a thin-film PEM. Meanwhile, the ability to directly photo-pattern PPC into features up to 25 μm tall made it more desirable than PCC. While the photo patterning ultimately saved much time and equipment usage once understood, the process optimization, including UV exposure dose, hot plate temperature, and development time, took much effort and varied for different film thicknesses.

After much work with SiO_2 on PPC resulted in good quality microchannels, the fabrication of fuel cells, first half-cells then full cells, and their testing could be accomplished. Because the oxygen reduction was found to be the limiting factor to performance in early devices, a thick-film ink cathode and porous gold current collector were utilized as the cathode for subsequent fuel cells. With the higher catalyst loading at the cathode, anode and membrane characteristics could be studied. Various tests with different fuels, anode catalyst loading, and PEM materials provided the bulk of data presented in previous chapters and discussed in some detail below.

12.2 Conclusions

Micro fuel cells utilizing sacrificial polymer-based microchannels and thin-film SiO_2, phosphorous-doped SiO_2, and polymer-on-SiO_2 proton exchange membranes were successfully fabricated and tested. PECVD silicon dioxide was not considered as a potential material for thin-film PEMs at the outset of this project. However, its combination of mechanical and dielectric properties made it suitable for use in integrated thin-film devices. Lowering the deposition temperature dramatically increased the conductivity of the SiO_2 to an acceptable level for the current densities achieved with the sputtered electrodes used in this project. Additional increases in conductivity were

realized by doping the films with phosphorous during the deposition. This allowed the thickness of the membranes to be increased without a loss in current density. The thicker films reduced fuel crossover, improving the open-circuit potentials and overall power production.

The performance of the micro fuel cells was chiefly limited by the amount of catalyst used. The amount of catalyst deposited though sputtering was extremely small. While the current density was acceptable for the catalyst loading used, increasing the catalyst in the electrode layers, but still maintaining the porosity of the sputtered layers for proton transport, was a key to increased performance. Repeated alternate catalyst sputtering and SiO_2 deposition steps to build up a catalyst matrix provided an electrode with increased catalyst and membrane-catalyst contact area. Another advance during the project was the study of acidic methanol as a fuel. When using this conductive analyte, additional catalyst that was not in contact with the membrane could be utilized.

Improvements to the membrane were also a key to the viability of these microfabricated fuel cells. The conductivity of the membranes and the open-circuit potentials, particularly with methanol, were very low with SiO_2-only PEMs. The use of acidic methanol also causes damage to the channel, limiting the viable lifetime of the devices. Two techniques that proved useful to improving the membrane performance were phosphorous-doping and fabricating polymer-on-SiO_2 composite membranes.

By adding phosphine to the gases used to make SiO_2 through plasma-enhanced chemical vapor deposition, phosphorous was successfully incorporated into the oxide films. This doping increased the conductivity of films made with otherwise similar recipes approximately 50 times. PEMs with twice as much thickness still had a lower

resistance than their un-doped counterparts. The increase in thickness helped make them more mechanically stable and decreased fuel crossover, resulting in higher open-circuit potentials and power densities.

To further improve the mechanical strength of the micro fuel cells, thin layers of polymers were deposited over the SiO_2 to form composite PEMs. These double-layer membranes offered better strength than SiO_2 alone, and better resistance to fuel permeation than a polymer only thin-film membrane. The two polymers that received the most attention were polyimide and Nafion. While polyimide improved the open-circuit potential, its resistance to proton transport reduced the current densities achieved. Nafion, the common polymer for PEM fuel cells, did not dramatically increase the resistance of the membrane, leading to increases in both the open-circuit potential and power densities.

While the performance was shown to increase dramatically with increased temperature, the ability of these devices to maintain an elevated temperature on their own is questionable because of their small size. The amount of waste heat produced by the fuel cells that can be retained will affect their level of performance because of the temperature dependence of the cells. The goal will be a design with maximum insulation for the fuel cells to keep the operating temperature as high as possible. They will most likely find usage in applications where high current or power output is not as important as the high energy density they can offer at any temperature.

The use of hydrogen proved to be better suited for microchannel-based fuel cells than methanol. The amount of power that could be produced by the liquid fuel was limited because of carbon dioxide bubbles that restrict flow and cover active catalyst sites

due mainly to the volumetric expansion between a liquid and gas. The concentration of fuel that could be used before dramatic performance decreases were seen due to crossover was limited at about 4 Molar. With the lower concentration of fuel and current densities achieved, vaporization of the fuel from waste heat would not be realized.

Additionally, the design for a methanol storage pump that would deliver a constant pressure at the microchannel inlet resulted in a prototype with a lower volumetric efficiency. Meanwhile, advances in hydrogen storage have been discovered. This includes a design that uses of $LiAlH_4$ and controls the release of gaseous H_2 at a constant pressure. The compact container could be used with the microfabricated fuel cells.

12.3 Suggestions for future work

12.3.2 Improving micro fuel cells

The amount of work that can continue to be done on thin-film fuel cells remains greater than what has been done to date. Some of the research areas include material properties, optimization of catalyst and PEM layer thicknesses, co-fabrication with electronic circuits or other devices, and the construction of a completed prototype with miniaturized fuel storage and delivery.

Phosphorous-doped SiO_2 appears to be the leading material for thin-film PEMs. Its deposition by PECVD has been studied to some degree, but further work may continue to increase its ionic conductivity through recipe changes. Its optimal thickness has yet to be determined and could likely be dependent upon catalyst loading and type of fuel used.

Likewise, neither the optimum catalyst loading for a deposited layer or the best number of sputtered layers has been determined. The multi-layer, embedded catalyst technique offers a tremendous advantage over the single-layer method, but also requires much more study. Experiments that could be performed would not only include the amount of catalyst in each layer, but the amount of electrolyte to be deposited between layers and after how many successive layers does the improvement in performance become negligible.

Modeling of the multi-layer catalyst/electrolyte structure could be very beneficial. However, basic knowledge of the materials, including fuel diffusivity in the electrolyte, activity of the catalyst, and topography of the individual layers, would be necessary. Other modeling studies that could also prove valuable would include fuel flow in the microchannels and air flow and water removal above the oxygen reduction cathode.

Additionally, to be capable of producing a reasonable amount of power, the active area of the fuel cells must be increased. The previous chapter describes one method currently under investigation. This new fabrication technique tackles many necessary issues in the scale up to 1 cm^2 or greater sizes, but may prove to have its own shortcomings. Alternative methods to make fuel delivery channels, such as silicon trench etching, may prove to be a better method. Likewise, a design and fabrication sequence that does not utilize thermally decomposed sacrificial polymers would reduce some material compatibility issues and the problems with post-decomposition residue on the catalyst.

12.3.2 Applications with conventional fuel cells

Another area of study that could be undertaken would be the application of some of the fabrication techniques or materials developed in this project for microchannel-based fuel cells to larger, more traditional PEM fuel cells. The use of sputtered catalyst and thin-film proton exchange membranes are two of the most significant contributions from the microfabricated fuel cell project that could be applied to conventional fuel cells. The use of membrane materials than can be deposited by chemical vapor deposition (CVD) or PECVD enables the sputtered catalyst to be embedded in the electrolyte, increasing the amount of catalyst that can be deposited through multiple sputtering layers.

Platinum and platinum-based alloys are the most common catalysts used in proton exchange membrane (PEM) fuel cells. Because of the high cost of Pt, an important topic of investigation is decreased catalyst loading. Sputtering a small amount of catalyst can produce a layer that has a much higher surface area to weight ratio than even catalyst particles with an average size on the order of one micrometer. Other advantages to sputtering the catalyst include reproducibility and a possible reduction in wasted catalyst.

A fuel cell membrane electrode assembly (MEA) is typically constructed by hot-pressing gas diffusion layers (GDLs) to the PEM. These gas diffusion layers are usually carbon-based fibrous materials. Pt particles are suspended in ink and brushed onto the side of the GDL that will be in contact with the membrane before they are hot-pressed together. Sputtering the catalyst directly onto the PEM and/or the GDL could enable improved performance with decreased cost. Increased performance and improvements to the power vs. cost of materials could possibly be realized.

Proton exchange membranes made through common microfabrication techniques, including spin-coating and plasma enhanced chemical vapor deposition (PECVD), can have thicknesses from 1 to 20 micrometers. The thin-film membrane materials in this project have included polymers, silicon dioxide, and doped silicon dioxide. The main advantage of a thin-film membrane is increased conductance of protons versus a thicker film of the same material. While the materials studied thus far have all been too fragile to use as free-standing membranes, there are other ways to physically support them. One method that we found to work well was the direct deposition of the electrolyte membrane onto a GDL. Supported membranes were used for basic testing, but not in the construction of full cells as part of the project. Additional work with the supported thin-film membranes could make them useful in larger cells.

For a typical PEM, a number of material properties must be achieved for good performance. The use of multi-layer, or composite, membranes may offer a way to improve fuel cell performance, as was the case when Nafion was used in a polymer-on-SiO_2 membrane in the micro fuel cells. Two or more thin-film membranes could have a total thickness less than a standard Nafion film and offer a better combination of material properties due to contributions from the different materials. This concept has a great amount of area for expanded research and development, including the investigation of materials not used in this project.

In this work, the technique of embedding multiple layers of sputtered catalyst into the electrolyte increased the total amount of catalyst that could be used and therefore the performance. This technique requires that the membrane material be deposited by PECVD, CVD, or in a manner such that amount deposited can be very little and tightly

controlled. If sputtered catalysts are to be applied to larger fuel cells, this could be one technique to achieve suitable levels of catalyst loading. A catalyst-electrolyte matrix made through alternate sputtering of catalyst and deposition of thin electrolyte layers must still meet the same requirements as the single catalyst layers, namely enough catalyst to be electrically conductive while maintaining porosity for reactant and proton transport.

REFERENCES

1. S. C. Kelley, G. A. Deluga, and W. H. Smyrl, "A Miniature Methanol/Air Polymer Electrolyte Fuel Cell" *Electrochemical and Solid-State Letters*, **3**, 407-9 (2000).

2. J. D. Morse, A. F. Jankowski, R. T. Graff, and J. P. Hayes, "Novel proton exchange membrane thin-film fuel cell for microscale energy conversion" *Journal of Vacuum Science & Technology A,* **18**, 2003-5 (2000).

3. S. J. Lee, A. Chang-Chien, S. W. Cha, R. O'Hayre, Y. I. Park, Y. Saito, and F. B. Prinz, "Design and fabrication of a micro fuel cell array with 'flip-flop' interconnection" *Journal of Power Sources*, **112**, 410-18 (2002).

4. J. S. Wainright, F. R. Savinell, C. C. Liu, and M. Litt, "Microfabricated Fuel Cells" Electrochimica Acta, **48**, 2869-77 (2003).

5. M. Hayase, T. Kawase, and T. Hatsuzawa, "Miniature 250 μm Thick Fuel Cell with Monolithically Fabricated Silicon Electrodes" *Electrochemical and Solid-State Letters*, **7**, A231-4, (2004).

6. J. Yu, P. Chenga, Z. Maa, and B. Yi, "Fabrication of miniature silicon wafer fuel cells with improved performance" *Journal of Power Sources*, **124**, 40-46 (2003).

7. L. Carrette, K.A. Friedrich, and U. Stimming, "Fuel Cells – Fundamentals and Applications" *Fuel Cells,* **1**, no. 1, 5-39 (2001).

8. S. Wasmus, and A. Kuver, "Methanol Oxidation and Direct Methanol Fuel Cells: A Selective Review" *Journal of Electroanalytical Chemistry*, **461**, 14-31 (1999).

9. L. J. Burcham and I. E. Wachs, "The Origin of the Support Effect in Supported Metal Oxide Catalysts: In Situ Infrared and Kinetic Studies During Methanol Oxidation" *Catalysis Today*, **49**, 467-484 (1999).

10. S. F. Baxter, V. S. Battaglia, and R. E. White, "Methanol Fuel Cell Model: Anode" *Journal of the Electrochemical Society*, **146**, 437-47 (1999).

11. G. T. Burstein, C. J. Barnett, A. R. Kucernak and K. R. Williams, "Aspects of the Anodic Oxidation of Methanol" *Catalysis Today*, **38**, 425-37 (1997).

12. A. Hamnett, "Mechanism and Electrocatalysis in the Direct Methanol Fuel Cell" *Catalysis Today*, **38**, 445-57 (1997).

13. C. He, H. R. Kunz, and J. M. Fenton, "Evaluation of Platinum-Based Catalysts for Methanol Electro-oxidation in Phosphoric Acid Electrolyte" *Journal of the Electrochemical Society*, **144**, 970-979 (1997).

14. A. S. Lin, A. D. Kowalak and W. E. O'Grady, “Studies of the Role of Water in the Electrocatalysis of Methanol Oxidation” *Journal of Power Sources*, **58**, no. 1, 67-72 (1996).

15. M. P. Hogarth, and G. A. Hards, “Direct Methanol Fuel Cells” *Platinum Metals Review*, **40**, no.4, 150 (1996).

16. Y. Morimoto and E. B. Yeager, “Comparison of Methanol Oxidations on Pt, Pt|Ru and Pt|Sn Electrodes” *Journal of Electroanalytical Chemistry*, **444**, no. 1, 95-100 (1998).

17. A. B. Anderson, E. Grantscharova, and S. Seong, “Systematic Theoretical Study of Alloys of Platinum for Enhanced Methanol Fuel Cell Performance” *Journal of the Electrochemical Society*, **143**, 2075-82 (1996).

18. H. S. Wroblowa, Y.-C. Pan and G. Razumney, “Electroreduction of Oxygen. A New Mechanistic Criterion” *Journal of Electroanalytical Chemistry and Interfacial Electrochemistry*, **69**, no. 2, 195-201 (1976).

19. A. J. Appleby and M. Savy, “Kinetics of Oxygen Reduction Reactions Involving Catalytic Decomposition of Hydrogen Peroxide. Application to Porous and Rotating Ring-disk Electrodes” *Journal of Electroanalytical Chemistry and Interfacial Electrochemistry*, **92**, no. 1, 15-30 (1978).

20. S. Fukada, “Analysis of Oxygen Rduction Rate in a Proton Exchange Membrane Fuel Cell” *Energy Conversion & Management*, **42**, 1121-1131 (2001).

21. S. Gottesfield and T. Zawodzinski, “Polymer Electrolyte Fuel Cells” in *Advances in Electrochemical Science and Engineering*, Vol. 5, Wiley-VCH, 195-301 (1997)

22. J.-T. Wang, S. Wasmus, and R. F. Savinell, “Real-Time Mass Spectrometric Study of the Methanol Crossover in a Direct Methanol Fuel Cell” *Journal of the Electrochemical Society*, **143**, 1233-39 (1996).

23. A. Heinzel and V. M. Barragan, “A Review of the State-of-the-Art of the Methanol Crossover in Direct Methanol Fuel Cells” *Journal of Power Sources*, **84**, 70-74 (1999).

24. K. Scott, W. M. Taama, P. Argyropoulos and K. Sundmacher, “The Impact of Mass Transport and Methanol Crossover on the Direct Methanol Fuel Cell” *Journal of Power Sources*, **83**, 204-216 (1999).

25. D. H. Jung, C. H. Lee, C. S. Kim and D. R. Shin, “Performance of a Direct Methanol Polymer Electrolyte Fuel Cell” *Journal of Power Sources*, **71**, 169-173 (1998).

26. W. C. Choi, J. D. Kim and S. I. Woo, “Modification of Proton Conducting Membrane for Reducing Methanol Crossover in a Direct-Methanol Fuel Cell” *Journal of Power Sources*, **96**, 411-14 (2001).

27. X. Ren, M. S. Wilson, and S. Gottesfeld, “High Performance Direct Methanol Polymer Electrolyte Fuel Cells” *Journal of the Electrochemical Society*, **143**, L12-L15 (1996).

28. P. A. Kohl, Q. Zhao, K. Patel, D. Schmidt, S. A. Bidstrup-Allen, R. Shick, and S. Jayaraman, “Air-Gaps for Electrical Interconnections” *Electrochemical and Solid-State Letters*, **1**, 49-51 (1998).

29. D. Bhusari, H. A. Reed, M. Wedlake, A. M. Padovani, S. A. Bidstrup-Allen, and P. A. Kohl, ”Fabrication of Air-Channel Structures for Microfluidic, Microelectromechanical, and Microelectronic Applications” *Journal of Microelectromechanical Systems*, **10**, 400-408 (2001).

30. J. Fontanella, M. Wintersgill, J. Wainright, R. Savinell and M. Litt, “High Pressure Electrical Conductivity Studies of Acid Doped Polybenzimidazole” *Electrochemica Acta*, **43**, 1289-94 (1998).

31. J. Holladay , J. Wainright , E. Jones and S. Gano, “Power Generation Using a Mesoscale Fuel Cell Integrated with a Microscale Fuel Processor” *Journal of Power Sources*, **130**, 111-18 (2004).

32. M. F. Ceiler, Jr., P. A. Kohl, S. A. Bidstrup, “Plasma-Enhanced Chemical Vapor Deposition of Silicon Dioxide Deposited at Low Temperatures” *Journal of the Electrochemical Society*, **142**, 2067-71 (1995).

33. Y. Abe, H. Hosono, and Y. Ohta, “Protonic Conduction in Oxide Glasses: Simple relations between electrical conductivity, activation energy, and the O – H Bonding State” *Physical Review B*, **38**, no. 14, 10166-69 (1988).

34. M. Kotama, K. Nakanishi, H. Hosono, Y. Abe, and L. Hench, “Evidence for Protonic Conduction in Alkali-Free Phosphate Glasses” *Journal of the Electrochemical Society*, **138**, no. 10, 2928-30 (1991).

35. Y. Abe, H. Shimakawa, and L. Hench, “Protonic Conduction in Alkaline Earth Metaphosphate Glasses Containing Water” *Journal of Non-Crystalline Solids*, **51**, 357-65 (1982).

36. C. Wang and M. Nogami, “Effect of Formamide Additive on Protonic Conduction of P_2O_5-SiO_2 Glasses Prepared by Sol-Gel Method” *Materials Letters*, **42**, 225-8 (2000).

37. L. Li, P. Cong, R. Viswanathan, F. Qinbai, L. Renxuan and E. S. Smotkin, “Carbon supported and unsupported Pt-Ru anodes for liquid feed direct methanol fuel cells” *Electrochimica Acta*, **43**, 3657-63 (1998).

38. S. Aricò, P. Cretì, E. Modica, G. Monforte, V. Baglio and V. Antonucci, "Investigation of direct methanol fuel cells based on unsupported Pt–Ru anode catalysts with different chemical properties" *Electrochiica. Acta,* **45**, 4319-28 (2000).

39. Y.-C. Liu, X.-P. Qiu, Y.-Q. Huang, W.-T. Zhu and G.-S. Wu, "Influence of preparation process of MEA with mesocarbon microbeads supported Pt-Ru catalysts on methanol electrooxidation" *Journal of Applied Electrochemistry*, **32,** 1279-1285 (2002).

40. F. Maillard, F. Gloaguen and J.-M. Leger, "Preparation of methanol oxidation electrocatalysts: Ruthenium deposition on carbon-supported platinum nanoparticles" *Journal of Applied Electrochemistry,* **33,** 1-8 (2003).

41. J.-M. Leger, "Mechanistic aspects of methanol oxidation on platinum-based electrocatalysts" *Journal of Applied Electrochemistry,* **31,** 767-771 (2001).

42. J. Munk, P. A. Christensen, A. Hamnett and E. Skou, "The electrochemical oxidation of methanol on platinum and platinum + ruthenium particulate electrodes studied by in-situ FTIR spectroscopy and electrochemical mass spectrometry" *Journal of Electroanalytical Chemistry*, **401**, 215-222 (1996).

43. H. Wang, C. Wingender, H. Baltruschat, M. Lopez and M. T. Reetz, "Methanol oxidation on Pt, PtRu, and colloidal Pt electrocatalysts: a DEMS study of product formation" *Journal of Electroanalytical Chemistry,* **509**, 163-169 (2001).

44. S. Wasmus and A. Küver, "Methanol oxidation and direct methanol fuel cells: a selective review" *Journal of Electroanalytical Chemistry*, **461**, 14-31 (1999).

45. K. Shukla, P. A. Christensen, A. J. Dickinson and A. Hamnett, "A liquid-feed solid polymer electrolyte direct methanol fuel cell operating at near-ambient conditions" *Journal of Power Sources* **76,** 54-59 (1998).

46. M. Hogarth, P. Christensen, A. Hamnett and A. Shukla, "The design and construction of high-performance direct methanol fuel cells. 1. Liquid-feed systems" *Journal of Power Sources,* **69,** 113-124 (1997).

47. E. Dobierzewska-Mozrzymas, E. Pieciul, P. Bieganski, and G. Szymczak, "Conduction Mechanisms in Discontinuous Pt Films" *Crystal Research and Technology*, **36**, 1137-44 (2001).

48. R. O'Hayre, S.-J. Lee, S.-W. Cha and F. B. Prinz, "A sharp peak in the performance of sputtered platinum fuel cells at ultra-low platinum loading" *Journal of Power Sources*, **109,** 483-93 (2002).

49. R. B. Byrd, W. E. Stewart, and E. N. Lightfoot, "Velocity Distributions in Laminar Flow" in *Transport Phenomena*, John Wiley & Sons, 34-69 (1960).

50. A. Oedegaard, C. Hebling, A. Schmitz, S. Møller-Holst, and R. Tunold, "Influence of diffusion layer properties on low temperature DMFC" *J. Power Sources,* **127,** 187-96 (2004).

51. Z. G. Shao and I. M. Hsing, "Nafion Membrane Coated with Sulfonated Poly(vinyl alcohol)-Nafion Film for Direct Methanol Fuel Cells" *Electrochemical and Solid-State Letters,* **5,** A185-A187 (2002).

52. A. S. Aricò, S. Srinivasan, and V. Antonucci, "DMFCs: From Fundamental Aspects to Technology Development" *Fuel Cells,* **1,** 133-61 (2001).

53. R. Dillon, S. Srinivasan , A. S. Aricò and V. Antonucci, "Aging mechanisms and lifetime of PEFC and DMFC" *Journal of Power Sources,* **127,** 112-26 (2004).

54. A. S. Aricò, V. Baglio, A. Di Blasi, E. Modica, P. L. Antonucci, and V. Antonucci, "Surface properties of inorganic fillers for application in composite membranes-direct methanol fuel cells" *Journal of Power Sources,* **128,** 113-18 (2004).

55. V. Gogel, T. Frey, Zhu Yongsheng, K. A. Friedrich, L. Jörissen, and J. Garche, "Performance and methanol permeation of direct methanol fuel cells: dependence on operating conditions and on electrode structure" *J. Power Sources,* **127,** 172-80 (2004).

56. N. Miyake, J. S. Wainright, and R. F. Savinell, "Evaluation of a Sol-Gel Derived Nafion/Silica Hybrid Membrane for Proton Electrolyte Membrane Fuel Cell Applications: I. Proton Conductivity and Water Content" *Journal of the Electrochemical Society,* **148,** A898-A904 (2001).

57. K. Sundmacher, T. Schultz, S. Zhou, K. Scott, M. Ginkel, and E. D. Gilles, "Dynamics of the direct methanol fuel cell (DMFC): experiments and model-based analysis" *Chemical Engineering Science,* **56,** 333–41 (2001).

58. K. Sundmacher and K. Scott, "Direct methanol polymer electrolyte fuel cell: Analysis of charge and mass transfer in the vapour–liquid–solid system" *Chemical Engineering Science,* **54,** 2927–36 (1999).

59. L. Li, P. Cong, R. Viswanathan, F. Qinbai, L. Renxuan, and E. S. Smotkin, "Carbon supported and unsupported Pt-Ru anodes for liquid feed direct methanol fuel cells" *Electrochimica Acta,* **43,** 3657-63 (1998).

60. P. A. Christensen, A. Hamnett, J. Munk and G. L. Troughton, "An in situ FTIR study of the electrochemical oxidation of methanol at small platinum particles" *Journal of Electroanaytical Chemistry,* **370**, 251-58 (1994).

61. J.-H. Choi, K.-W. Park, B.-K. Kwon, and Y.-E. Sung, "Methanol Oxidation on Pt/Ru, Pt/Ni, and Pt/Ru/Ni Anode Electrocatalysts at Different Temperatures for DMFCs" *Journal of the Electrochemical Society,* **150,** A973-A978 (2003).

62. M. Watanabe, Y. Genjima, and K. Turumi, “Direct Methanol Oxidation on Platinum Electrodes with Ruthenium Adatoms in Hot Phosphoric Acid” *Journal of the Electrochemical Society,* **144,** 423-28 (1997).

63. J. Prabhuram and R. Manoharan, “Investigation of methanol oxidation on unsupported platinum electrodes in strong alkali and strong acid” *Journal of Power Sources,* **74,** 54-61 (1998).

64. G. Tremiliosi-Filho, H. Kim, W. Chrzanowski, A. Wieckowski, B. Grzybowska and P. Kulesza, “Reactivity and activation parameters in methanol oxidation on platinum single crystal electrodes ‘decorated’ by ruthenium adlayers” *Journal of Electroanalytical Chemistry,* **467,** 143-56 (1999).

65. H. Hoster, T. Iwasita, H. Baumgärtner, and W. Vielstich, “Current-Time Behavior of Smooth and Porous PtRu Surfaces for Methanol Oxidation” *Journal of the Electrochemical Society,* **148,** A496-A501 (2001).

66. S. Slade, S. A. Campbell, T. R. Ralph, and F. C. Walsh, “Ionic Conductivity of an Extruded Nafion 1100 EW Series of Membranes” *Journal of the Electrochemical Society*, **149**, A1556-64 (2002).